Development of a Radiation Counting System Based on a Plastic Scintillator for Medical Applications

Rubena Yusoff

Doctor of Philosophy

University of York

Physics

September 2019

Abstract

Radiotracer input function study is a common method to study the physiological and biochemical processes in early drug development as well as for therapeutic purpose and it is usually clinically performed on small animals to reduce blood withdrawal that can cause blood depletion. The common measurement principle is also applied in quality control tests of radiotracer production to ensure accurate amount of dose being produced. It is desirable of such testing devices to handle low volumes of radioactive fluid. The first part of the thesis introduces a novel type of scintillator detector based on microfluidic technology. The proposed detector can measure radiotracer activity in fluid in a microfluidic channel that is used to determine the input function in real time. At initial stage, simulation work using GEANT4 was done to validate the most suitable fluidic channel designs by optimising the dimensions of the channels to get higher count rate. The microfluidic detector prototype was fabricated using Polydimethylsiloxane(PDMS) and coupled to Silicon photomultipliers(SiPM). Experiments were carried out to evaluate the performance of the prototype in terms of the material effects on residual activity, detection efficiency, minimum detectable activity, linearity and sensitivity of the microfluidic prototype. PDMS has almost 10 times higher residual activity compare to glass. Absolute efficiency for ^{18}F ranges between 2.5-7.6% and for ^{68}Ga between 6.6-33.9%. ^{18}F is linear up to 11000 cps while ^{68}Ga up to 8000 cps. Sensitivity of the detector for ^{18}F is 0.8% and 2.9% for ^{68}Ga. The second part of the thesis describes a detector based on scintillating fiber technology. Due to the size, flexibility and cost of manufacturing of such fiber, it is a best possible option for activity counting in narrow diameter environment such as blood vessels. However, due to the sub-mm diameter of fiber, the number of counts detected is small. Preliminary investigation of scintillating fiber shows less than 1$\pm$0.1% difference from the actual half-life of ^{18}F. Initial feasibility studies of the prototype show excellent agreement of the measured decay time with theoretical decay time. The probe the absolute sensitivity is 289 cps/MBq/ml.

Contents

List of Figures

6

List of Tables

Acknowledgements

keep me calm during this stressful time.

Declaration

This thesis has been submitted for the degree of Doctor of Philosophy in accordance with the regulations of the University of York. The work contained herein has not been previously submitted for any other degree or qualification. I declare that this thesis is a presentation of original work and I am the sole author. This work has not previously been presented for an award at this, or any other, University. All sources are acknowledged as References.

The simulation and experimental work outlined in this thesis was performed solely by the author under the supervision of Prof D.G. Jenkins.

Signed

Rubena Yusoff

Chapter 1

Introduction

This chapter gives a brief account of the uses of PET for small animal study. The blood input function measurement methods are then described in section 1.2. The need for a miniaturised beta detectors in quality control aspects of radiotracer production are explained in section 1.3. An overview of research motivation and thesis objectives are then given. Lastly, the structure of the thesis is outlined.

Nuclear Medicine is a branch of medical diagnostic imaging that has been widely used in oncology, cardiology and neurology. The science of nuclear medicine involves administration of labelled-radionuclides to obtain diagnostic images. These radionuclides are also used for therapeutic purposes with similar science. Positron Emission Tomography (PET) and Single Photon Emission Computed Tomography(SPECT) are two nuclear medicine imaging modalities that are used to radiodetect specific disease or condition by injecting a radiotracer into the patient. The positron emitting radiotracer will accumulate in diseased organs and decay, producing annihilation photons. These photons will reach detector rings and eventually produce an image of the patient. The difference of these modalities to other imaging devices is that they provide physiological information such as tissue perfusion[12], metabolism process[13] and receptor function[14].

PET and SPECT has also demonstrated their use in in-vivo imaging technique for small animal imaging. This field of study is called molecular imaging, that is the study of biochemical processes such as pathological investigation[15] and molecular level pharmacology[16]. Compared to a human PET scanner, small animal scanners are much smaller in size. Due to the small size of the subject, small animal scanners ideally require a high spatial resolution. The most important advantage of a small animal scanners is that they can provide information on the biological process, not just their effect at the end of the process. In turn, this permits evaluation of disease and provides information of biochemical, physiologic, and molecular effects of pharmaceutical drugs.

1.1 PET for Small Animal Study

There is a large database of PET animal studies that provide the bridge between preclinical discoveries and implementation in the clinical field. In new drug development, for example, the pharmacodynamic and pharmacokinetic properties of new proposed drugs are studied extensively to obtain preclinical data. The anal-

ysed trial data must go through a regulatory body before clinical trials on humans can be performed. Conventionally, animal studies were done invasively by dissecting and sacrificing a large number of animals. Nowadays, PET animal studies have effectively reduced the amount of animal testing and the cost of experiments[17].

PET with ^{18}F is widely use to study the kinetic model of metabolic processes. The dynamic data can be acquired by analysis of the input function of ^{18}F in blood plasma at a specific region of interest. Input function describes concentration of tracer in fluid as a function of time. By comparing the input function of the organ of interest to the theoretical models, it is possible to measure the metabolic process of the drug.

The main method to acquire accurate blood input function requires numerous blood samplings from the subject over the course of the evaluation. This is challenging, in particular to small animals, due to the limited amount of blood and small blood vessels. There are other less invasive options to estimate the input function such as a beta-probe measurements and arterial shunts or a non-invasive methods, such as the Image-derived Input Function (IDIF)[18] and Factor Analysis (FA)[19].

1.2 Blood Input Function Measurement Methods

Blood input function used to study blood metabolic processes can be acquired in several ways. The radioactivity concentration in arterial plasma represents the input function, and is commonly acquired from measurement of the radioactivity level in arterial blood. Figure 1.1 showing example of input function from a real-time microfluidic chip detector. The blood radioactivity counts peak at the time of radiotracer administration and rapidly drop throughout the first 50 s of measurement because most of the radioactive fluid has passed through the micro

19

channel. There are several methods to acquire blood input function. The current methods can be categorised into two, (a) the Image-based Method and (b) the Blood activity method. These methods will be discussed further in the following sections.
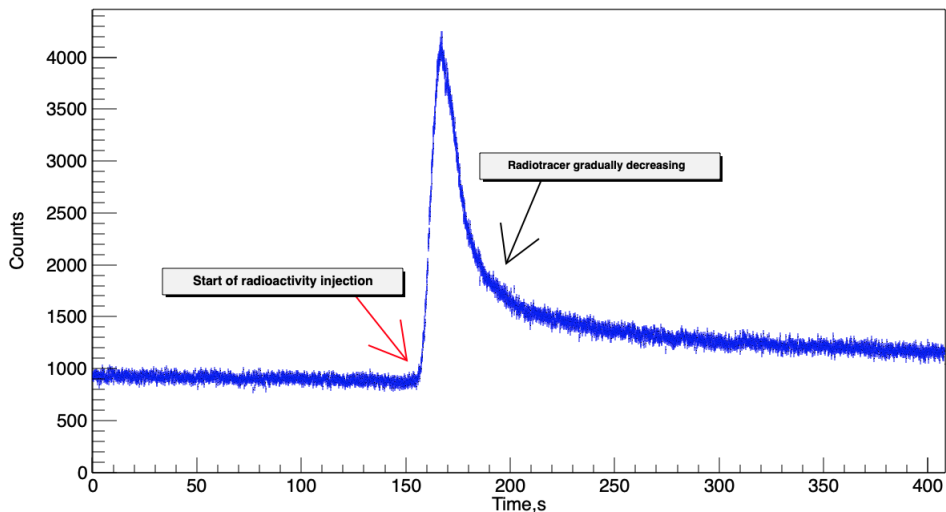
Figure 1.1: Input function measured in a microfluidic detector. At the instance of radiotracer administration in a flow through measurement, the radioactivity increases and reduces when radioactive fluid exit the micro channel.

1.2.1   Image-based Method

Image-derived Input function

Image-derived Input Function (IDIF) is the method of obtaining input function from direct measurement of dynamic PET images. Input function obtained by drawing a Region of Interest (ROI) over a blood pool organ such as heart, aorta or femoral arteries and then corrected with recovery coefficient which is calculated by Full width half maximum (FWHM) of the ROI of the centre of PET image and it is commonly utilised in human studies [20]. This method simplified scanning procedures, thus eliminates the need for blood handling and reduces the radiation exposure to research personnel in comparison to blood sampling method. How-

ever, the accuracy of the measurements is affected by the partial volume effect and spillover. Partial volume effect happens when small structure appear to loss of activity concentration, while region close to high activity may appear high in activity than actual is known as spillover. It has been successfully validated for large blood pool organs especially in humans, however, overestimation or underestimation of the input function can occur in small animals because of the relatively small size of their organs compare to the spatial resolution of the scanners. A typical spatial resolution of a small animal PET is in the range of 1-2 mm in full width half maximum [21]. Moreover, it has limitation for organs outside of the blood pool such as the brain.

Factor Analysis

Factor Analysis (FA) is used to eliminate the need for ROI drawing and spillover correction [22]. FA is a mathematical technique based on principle component analysis, used to resolve the input function of individual homogeneous regions of tissues and blood from the overall tissue component. It is based on the assumption that the total voxel intensity in the PET image is the summation of all counts by individual components, which are distributed linearly. While reports[22][19] showed successful implementation of this method for human analysis, validation for small animals is difficult due to the small size of the cardiac chamber. Despite that, there was a report showing good estimation using FA in rodents[1].

An example of dynamic images is shown in figure 1.2(A) and (C) taken from a rat heart for 60 min for ^{18}F study and 20 min for ^{11}C study. Figure 1.2(B) and 1.2(D) shows the extracted FA images of a rat Right ventricle(RV), Left ventricle(LV) and Myocardium done with ^{18}F and ^{11}C ,respectively. The image was obtained by adding the voxel intensity of the ROI over the course of measurement.
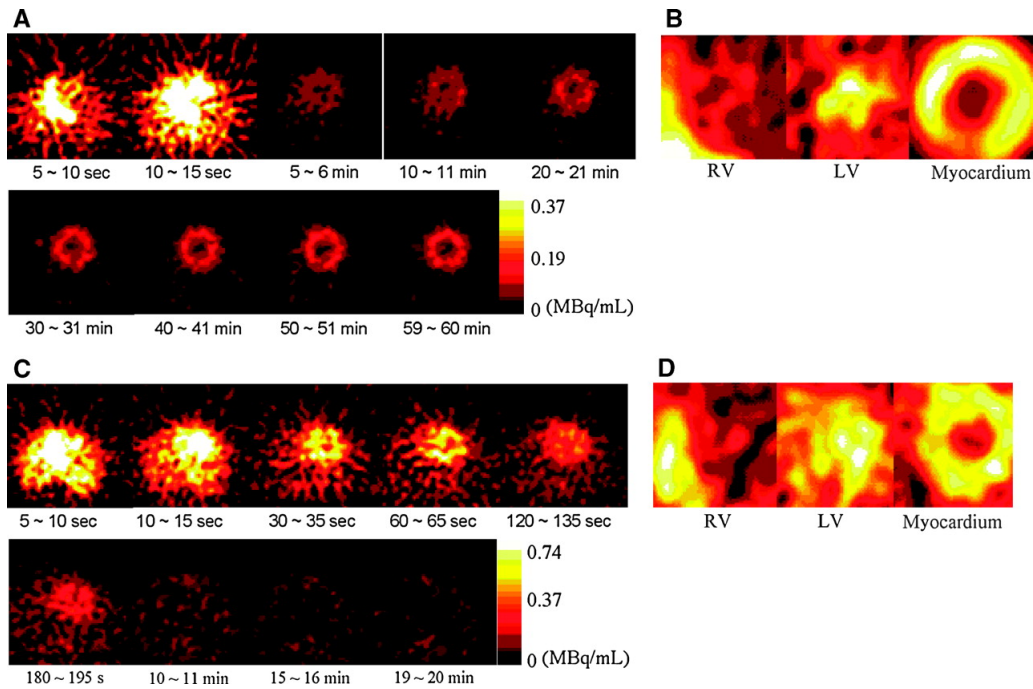
Figure 1.2: Example of Factor analysis images (B and D) obtained after factor analysis extraction for ^{18}F and ^{11}C studies on rat heart(respectively). Adapted from [1].

1.2.2 Blood Activity Methods

Although image-based methods have shown successful applications for blood kinetic analysis, the major drawbacks are spillover and partial volume effect on the ROI. Moreover, the methods can only be used for several PET radiopharmaceuticals and they are not entirely non-invasive because blood samples are still needed for reference, as it is the most accurate input function measurements method.

Direct blood activity measurement has been the gold standard to determine input function in small animals. The conventional way to quantify tracer activity in blood plasma in small animals is by drawing relatively large amount of blood and subsequently, analysis is done using a well counter which is labor intensive and may increase blood loss. Well counter was used because it has good geometric efficiency in order get most accurate photon measurements. There were numerous studies been done proposing methods to minimise the size of blood samples as well as reducing exposure to personnel such as automated micro blood sampling,

22

beta-probe and arterial shunt. The following section will discuss these methods.

The Arteriovenous Shunt

The Arteriovenous shunt technique requires a shunt to be placed between the artery and a vein while a detector measuring blood radioactivity is connected to the shunt by a tube. The method allows for online activity monitoring that will potentially increase the statistical quality of the input function and enable high temporal resolution. Furthermore, blood loss through manual sampling can be eliminated. On the other hand, the long tube connecting the shunt to the probe may cause dispersion effect. Dispersion of the fluid sample causes mixing and dilution of the sample resulting in distortion of the sample concentration. Dispersion in tube depends on the flow rate, temperature, length of tube and tube composition. This technique was proposed by a few groups[23][24] and had showed promising findings. A high degree of matching between a-v shunt probe with manual sampling, the goal standard, compared to the image-derived method as reported by Warnock et al. However, the method is very demanding in terms of animal preparation and close monitoring of the animals physiological states.

Beta Microprobe

The idea of the in vivo beta probe is to directly measure beta activity in the blood or fluid in an artery. It is also otherwise known as a fiber probe because of its geometry, the length is much larger than the thickness. The positrons have a relatively short range in matter, therefore such detector dimension is suitable for most positron emitting PET radiotracers. The ability to directly detect a positron in arteries, gives the detector better sensitivity and a better temporal resolution than manual sampling method and claimed to be less sensitive to gamma[25]. The whole detector and its electronics can be made quite compact and cheap. For the past decades, research [26][27][28] had been proposing potentially better beta

probe performance using fiber probes compared to manual sampling method for quantification of input function with PET radiotacer. The proposed beta probe constructions are composed of a thin scintillator, LSO [28] or thin plastic scintillating fiber glued to the tip of optical fiber and optically coupled to a photomultiplier tube(PMT). Coupling of the scintillators to the optical fiber can be a challenging task as they are tiny and need to be accurately coupled to reduce light loss. All of these previous studies have used a small scintillator (sensitive volume) on the tip of the detector with optical fiber to reduce gamma detection by the beta probe. A recent study[29] used a full length plastic scintillating fiber and showed no significant gamma signal from ^{99}Tc (140 keV) detected.

However, beta probes have some drawbacks as a minor procedure on the test subject is necessary to facilitate probe insertion. The probe needs to be light tight to prevent light from the surroundings to flood the photodetector. On the other hand, the thickness of the light seal has to be thin enough so it will not cause positron energy degradation. In addition to that, the total thickness of the probe must not be so large that it can cause interference to the blood flow and affecting the probe reading.

Arterial Blood Sampling

The blood sampling method is commonly regarded as the standard method for measurement of blood input function. In some studies, supplementary data from blood sampling techniques are needed for calibration purposes. Blood activity is measured directly by taking a small sample of blood (10-100 μL) for a certain time duration. The activity of the PET radiotracer can be measured by measuring beta particle decay or the annihilation photons. Nowadays, this is done by an automatic system to ensure reproducibility of the setup[30][31]. With the aim of reducing blood loss, studies have successfully measured blood sample activity from samples as low as 1 μL[32][33].

The conventional method of blood sampling is to repetitively withdrawing blood manually followed by blood separation and then measurement of radiation in a well counter. This is labor intensive and time consuming, and furthermore, increases radiation exposure to technicians. Moreover, when it comes to a small animal, blood volume is limited and constant blood withdrawal may interfere with the physiological condition of the animals. Automated sampling was introduced by Hutchins et. al. 1986[34] which has reduced measurement time and labor but correction such as dispersion and time shifts between time of blood withdrawal and time of measurement taken have to be account for. A computer operated high speed blood sampler was designed by Graham et. al. in 1993 but total blood volume was still large (2.6 mL)[35].

While most of the drawbacks of blood sampling has been overcome, problems arise from adsorption of tracer and metabolites on tubing and the sensitivity of the positron detector to annihilation gammas. These will alter the results of the input function obtained. Furthermore, photodetectors such as PMT are sensitive to magnetic fields, therefore restricting the application of such devices within Magnetic Resonance Imaging (MRI) scanners.

1.3 Quality Control of PET Radiotracer

Prior to radiotracer injection in humans, mandatory quality control(QC) tests are required by a regulatory body to ensure the safety of the produced radiotracer for clinical use. A toxicity tests are done to ensure the radiotracer is free from chemical contaminants. Likewise, radioactivity tests are done to ensure accurate patient dose and good quality images. Since PET radiotracers have short half lives (2 min to 109 min), QC tests must be done within a short period of time. Moreover, the tests must be done in a dedicated lab, fully equipped with analytical equipment. Caution has to be taken during handling due to the high radioactivity exposure.

For the past decade, PET radiotracer production processes have been miniaturised [36][37] successfully due to the reasons such as demand for a more personalised (dose-on-demand) radiotracer, use of less precursor, reliability and economical factors. Micro-reactor is a miniature size reactor for production of PET radiotracer. It consists of a series of microchannels that function as a "microfactory" to produce labelled radiotracer. All synthesising processes are done in the microreactor.

The downside of the dose-on-demand concept is that the radiotracer produced is sufficient only for single patient dose. With the limited volume of radiotracer being produced, performing quality control tests on the radiotracer on each production is difficult. Several studies[38][39][40] have reported successful method utilising microfluidic technology to reduce the scale of resources use in quality control aspect of PET radiotracer production. In quality control assessments, the proposed microfluidic detector can be use as a device to measure radioactivity of radiotacer to identify the type of radioisotope produced as well as to verify the dose activity for each patient. This detector works well along the microreactor as it do not utilize large sample volume.

1.4   Overview of Research Motivation

As discussed in the previous sections, microfluidic technology has found an application in the medical field. Attempts to improve its applicability in input function analysis has long been discussed, it was only just recently realised the use of microfluidic technologies in QC of PET radiotracer. Taggart et. al. has suggested the feasibility of microfluidic and SiPM for QC testing[40] and Tarn et. al. reported a promising finding of microfluidic for time-activity analysis[38]. These have motivated this research to investigate the possibilities of microfluidic chip application as an integrated particle detection system that can be use for both purposes. The proposed microfluidic detector presents a low cost and easy fabrication method

for a miniaturised positron detector system that can be used for input function analysis and to serve as a detector in a radiotracer microreactor system. Figure 1.3 is illustrating the principle setup and possible application of the microfluidic detector. The detector can be integrated to other system to run further radiotracer quality control assessments.
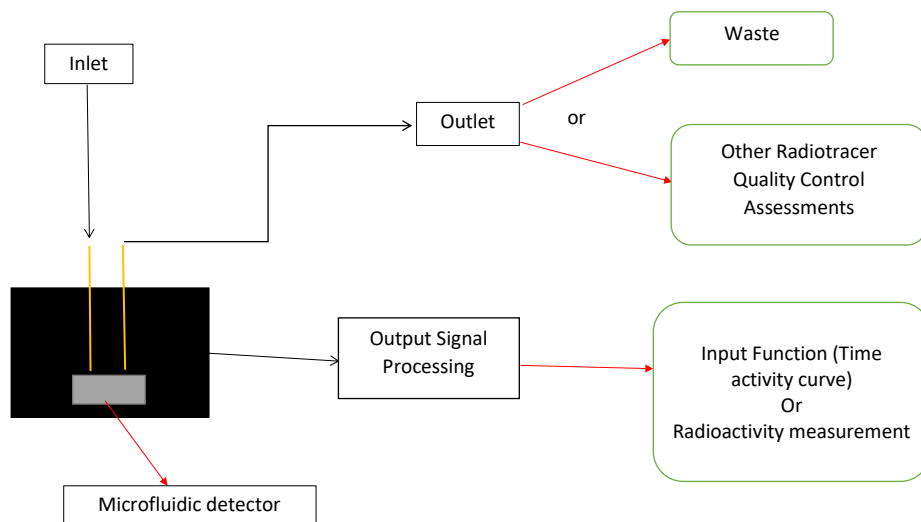
Figure 1.3: Principle setup of the microfluidic detector, showing the possibility of the system being implemented for some applications.

Likewise, the beta probe detector as a tool to obtain input function analysis has also been extensively researched. The proposed beta probe has increased the sensitive volume and eliminates the need for optical fiber as a light guide. Nevertheless, using scintillating fiber as the detector and as the light guide, may increases the detector gamma sensitivity. However, Knowland et. al. reported no count from gamma measured by scintillating fiber[29]. The proposed beta probe can also be used along side the microfluidic detector, especially when rapid activity measurement is needed i.e immediately after the injection of the radiotracer.

Different methods obtaining input function have their own benefits and limitations. Image based methods are limited by the spatial and temporal limitation of the imaging device. Blood sampling technique is considered as the reference stan-

dard as it produce accurate modelling. However, frequent blood sampling may result in blood depletion and has temporal limitation. The beta probe technique has excellent temporal resolution. The combination of both proposed detectors are able to reduce the volume of blood sample by using microfluidic technology that help to prevent blood depletion while maintaining excellent temporal resolution.

The two main goals of this thesis can be summarised as:

- fabrication and study of a microfluidic detector prototype to validate the performance of the detector in detecting fluid activity in a microvolume sample. It is a miniature detector fabricated using microfluidic technology and SiPM at a lower cost and it is reusable.

- fabrication and studies of plastic scintillating fiber as a beta probe for measurement of fluid activity for measurement within small constricted tube.

1.4.1 Thesis Objectives

The objectives of this thesis are to:

- fabricate microfluidic chips using a combination of PDMS-PDMS and PDMS-Glass by the replica molding technique

- investigate the effect of microfluidic material on residual activity in the fluidic channel

- calculate the detection efficiency, minimum detectable activity, linearity and sensitivity of the microfluidic detector prototype for measurement of ^{18}F and ^{68}Ga

- evaluate the effect of fiber bundles on photon yields at different distances.

- evaluate different photodetectors based on signal-to-noise ratio analysis

- fabricate a beta probe prototype coupled to SiPM

- investigate the beta probe light output for different sources i.e ^{137}Cs and ^{90}Sr

- calculate the beta probe ^{18}F decay time and sensitivity.

1.5   Thesis Structure

Chapter 2 presents an outline of the beta mechanism in matter and also the physics of the different scintillator types that are relevant to the study. It also describes a general introduction to scintillator detectors and microfluidic technology. GEANT4 simulation for evaluation of different microfluidic geometries, and light output and propagation in beta probe are detailed in chapter 3. Fabrication and characterisation of the microfluidic detector are explained in chapter 4. Chapter 5 presents the performance of plastic scintillating fibers and the fabrication of the proposed beta probe. General conclusion for both detectors and suggestion for future work are stated in chapter 6.

Chapter 2

Overview of Scintillation Detectors System

This chapter will discuss the theory underlying the operation of scintillation as well as light sensing technology. Section 2.1 will discuss passage of particles through matter while the properties and physics of scintillation is discussed in section 2.2. Section 2.3 will describe the scintillation light sensing technologies. Scintillation detector technologies are being discussed in section 2.4 focusing particularly on different types of scintillating fibers. Lastly, an introduction to microfluidic technology is given in section 2.5.

Since particle radiation is not visible by human sense, their detection principle utilises a medium that can absorb their energy and then convert it into a form such as electrical charge or scintillation photons. The fundamental science of particle detection is based on the knowledge of the particle interaction in matter. This interaction depends on the characteristics of the particle and detector material. Particles deposit their energy to surrounding molecules as they traverse matter. Some molecules convert this energy to light, which is known as scintillation light.

2.1   Passage of Particle Through Matter

A particle moving in matter interacts with surrounding atoms in the material. A particle loses energy as it passes through matter because of elastic collisions with nuclei and inelastic collisions with orbital electrons. The inelastic collisions may have two consequences. They can either cause excitation only or result in ionisation of the atom by knocking out an orbital electron[41]. This free orbital electron can lead to further secondary ionisation. Since excitation and ionisation of the atoms are a statistical process, there is no accurate deterministic event-by-event value of the energy loss. However, the mean rate of energy loss (stopping power) can be calculated using the Bethe-Bloch equation2.1,

$$-\frac{dE}{dx} = Kz^2\frac{Z}{A}\varrho\frac{1}{\beta^2}\left[\frac{1}{2}\ln\frac{2m_ec^2\beta^2\gamma^2T_{max}}{I^2} - \beta^2 - \frac{\delta}{2}\right] \tag{2.1}$$

where

- $K = 4\pi N_A r_e^2 m_e c^2 = 0.307 MeV mol^{-1} cm^2$

- $z =$ charge of incident particle

- $Z =$ atomic number of absorber

- $A =$ atomic mass

- $\beta = v/c$ is the velocity of particle

- m_e is the electron mass at rest

- c is the velocity of light

- $\gamma = \frac{1}{\sqrt{1-\beta^2}}$ is the Lorentz factor

- $\delta(\beta\gamma)$ is the density effect correction to ionisation energy loss

The Bethe-Bloch equation describes the mean energy loss per distance travelled of a heavy particle such as proton, alpha and ions but not electrons.

2.1.1 β Interaction Mechanism

Beta decay is the process of radioactive decay by the ejection of positive (β^+) or negative electron (β^-) from nucleus. The basic transformation is written as,

$$\begin{aligned} {}^{1}_{0}n &\rightarrow {}^{1}_{1}p + {}^{0}_{-1}\beta + \bar{\nu} &&(\beta^- \text{decay}) \\ {}^{1}_{1}p &\rightarrow {}^{1}_{0}n + {}^{0}_{+1}\beta + \nu &&(\beta^+ \text{decay}) \end{aligned}$$
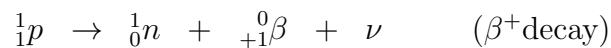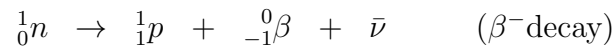
where ${}^{1}_{0}n$, ${}^{1}_{1}p$, $\bar{\nu}$ and ν stand for neutron, proton, antineutrino and neutrino respectively. Radionuclides lie above the region of stability have high neutron to proton (n/p) ratio. These nuclei achieve stability by reducing the n/p ratio through emission of negative electron. This is called β^- decay. Radionuclides with a deficit number of neutron and lower n/p ratio will emit positive electron or positron, in order to achieve stability. This is called β^+ decay.

In both mode of β decay, the disintegration energy is shared between the emitted particles. Since there is more than one particle emitted, the observed spectrum in the β decay is continuous. The β particles energies range from zero up to maximum energy. Figure 2.1 shows a typical beta particle energy spectrum.

The electrons can carry energy from almost zero up to the endpoint energy. The endpoint energy is the Q-value or the fixed decay energy.
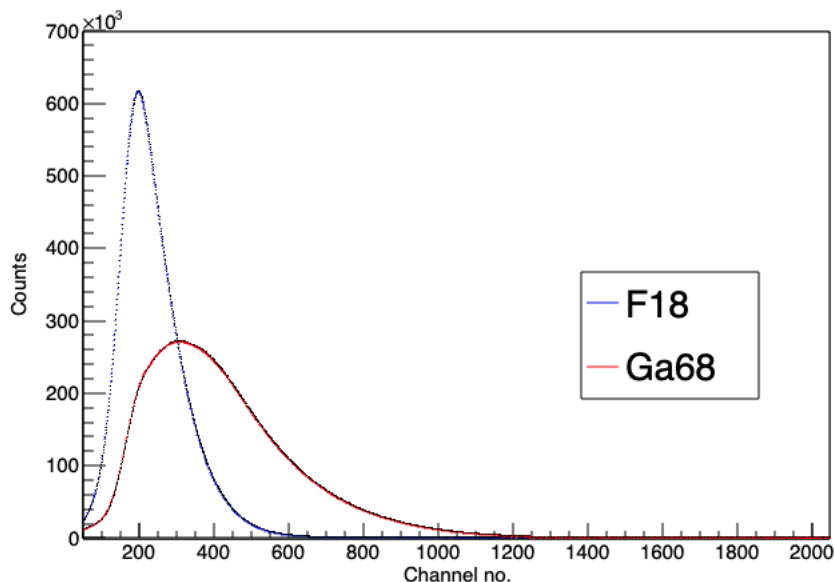
Figure 2.1: Beta energy spectra from typical Radiotracer, ^{18}F (Blue) and ^{68}Ga (Red).

The beta interaction mechanism in matter can be described by inelastic and elastic collisions. The beta particles loose energy via interaction with an orbital electron, which can then lead to excitation or ionisation of the atom. The maximum energy transfer during the collision can be expressed as,

$$Q_{max} = \frac{4mME}{(m+M)^2} \tag{2.2}$$

where E is the kinetic energy of beta, m is the mass of beta and M is the mass of orbital electron. Since $m = M$, the Q_{max} is equal to E. Since the beta collides with electron of equal mass, this results in a large scattering angle.

The incoming beta can also interact with atomic nuclei and experience deceleration. This will emit electromagnetic radiation called bremsstrahlung. The bremsstrahlung photons have a continuous energy distribution. The larger the deceleration, the higher the photon energy being produced and it can reach a

maximum energy equal to the beta kinetic energy. The behaviour of electron passing through matter is largely influenced by the electron energy. Typical positron emitting nuclides for PET purposes ranges from 600 keV to 1900 keV. As shown in Figure 2.2, the dominant mode of β interaction in plastic scintillators at this energy range is collision of the beta with orbital electrons.
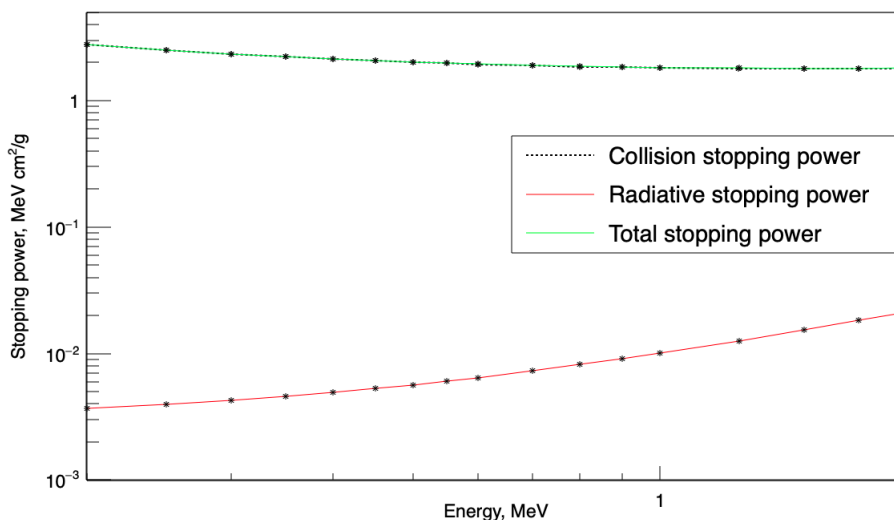
Figure 2.2: Collision (black dotted line) and radiative (red line) stopping powers in plastic scintillator that determine energy losses of electrons. At low energies (<2 MeV) ionization losses are maximum.

2.1.2   Electron-positron Annihilation

Positron is a positive charge particle that has similar mass as electron. During positron interaction in matter, it losses energy through Coulomb force interaction similar to electron, regardless of its charge. Regardless of repulsive or attractive interaction, energy transfer is similar. Thus the track, stopping power and range are analogous to the electron.

At the end of positron range, when it comes close to an electron, they will annihilate and as a result produce two identical photons. These photons each carry 511 keV of energy and travel in opposite direction. Annihilation photons are used

34

in PET imaging to produce images.

2.2   Scintillation Materials

As discussed in section 2.1, when a particle transfers its energy to a material, it will produce excited electron or photons. In a scintillation material, part of this energy is converted to optical photons. This process is called scintillation. Scintillation material can be classified into two categories, organic and inorganic. They are different in chemical properties as well as light production mechanism. In the context of this thesis, organic scintillator ie. plastic scintillator has been chosen as the scintillator for both prototypes.

2.2.1   Inorganic Scintillator

Inorganic scintillators are solid crystalline that scintillate due to their characteristic crystal structure. They can only scintillate light in their crystalline form. However, the inorganic scintillators can scintillate in their pure form such as NaI crystal at liquid Nitrogen temperature. Most of the crystals require impurities to change its crystalline structure that is responsible for the scintillation effect. For instance, NaI crystal can only scintillate light efficiently at room temperature when a small amount of Thallium impurities is added.

Most inorganic scintillators are dense ($\rho \sim$ 4 - 8 g/cm^{-3}) and have high atomic number. They are commonly used for particle or photons of high penetrating power. Inorganic scintillators have higher light output ($\sim$40 per keV) compare to other scintillators hence giving better energy resolution. Nevertheless, some inorganic scintillators are hygroscopic and fragile. Exposure to moisture or external stress may impair the light transmission.

The principle of scintillation light production in an inorganic scintillator is

graphically illustrated in figure 2.3. The empty conduction band and electron-rich valence band is fully separated by an energy gap. When ionising radiation passes through an inorganic scintillator, the energy absorbed produces an electron-hole pair and elevates the electron across the gap to the conduction band, leaving a positive charge hole in the valence band. Eventually, the electron will fall back to valence band and recombine with the hole. This will emit photons. In the case of a pure crystal, photons emitted will have high energy with respect to the visible light range. Impurities help to enhance the visible light emission by introducing an intermediate energy state within the energy gap. Upon recombination, the electron will transition to this intermediate level and then fall back to the valence band. Since the intermediate energy level is lower than the full energy gap, the photon emitted is within the visible light range.
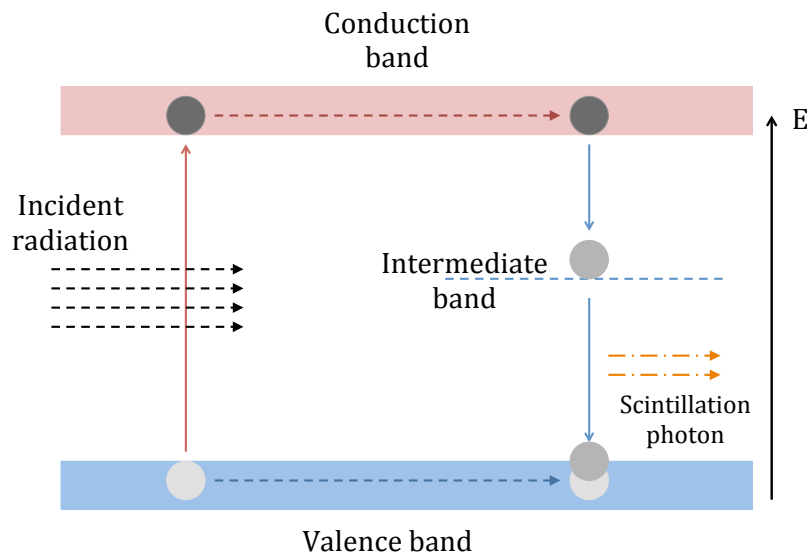
Figure 2.3: Scintillation mechanism in inorganic scintillator. The electron is excited to conduction band and moves freely. Upon recombination with a hole, the electron transit at the intermediate level. A photon emitted is in the visible light range.

Inorganic scintillators such as BGO, GSO and CWO are commonly used in spectroscopic application. LSO, LYSO and LFS are amongst the popular choice of scintillator for PET imaging when high position resolution, high efficiency and

high depth of interaction resolution are required [42][43][44]. Inorganic scintillators also exist in the form of noble gases and glasses. Scintillator gasses suffer from low light yield, despite that, it is still being used for heavy ion spectroscopy [45]. Cerium activated lithium or boron silicate are scintillating glass that are widely used in neutron detection because of high cross section of Li and B, but these scintillators only emit 3-4 photon per keV.

2.2.2 Organic Scintillators

Unlike inorganic scintillators, the fluorescence process in organic scintillators is an inherent molecular property. This means the scintillator can fluoresce, independent of its physical states. Organic scintillators can exist in the form of organic crystal e.g naphthalene, stilbene and anthracene or plastics and liquid. Plastic and liquid scintillator are the most commonly used organic scintillator because they are easily available in any shape and sizes while organic crystal is not a popular choice because of difficulty in manufacturing.

The scintillation mechanism in organic scintillators is basically excitation of an atom in the scintillator molecule. While de-excitation happens, it emits scintilation photons. The complete explanation of the mechanism is illustrated in figure 2.4. Incident radiation transfers energy to the molecules, where it excites an electron causing electron transitions from S_0 ground level to higher vibrational level in singlet states S_1, S_2, ... or triplet states T_0, T_1, T_3, ... This induces instability in the system, thus rapidly causes the electron transition to S_1 ground state or in the case of electron in triplet states, it will decay to T_0 ground state through radiationless transition. After that, the electrons will decay to S_0 ground state, releasing excess energy in the form of scintillation photons.

There is also possibility of molecules of T_0 state interacts with other molecules of same state, leaving one molecule in S_1 excited state. That molecule will then undergo fluorescence transition and emits UV photons. Since triplet state is more

37
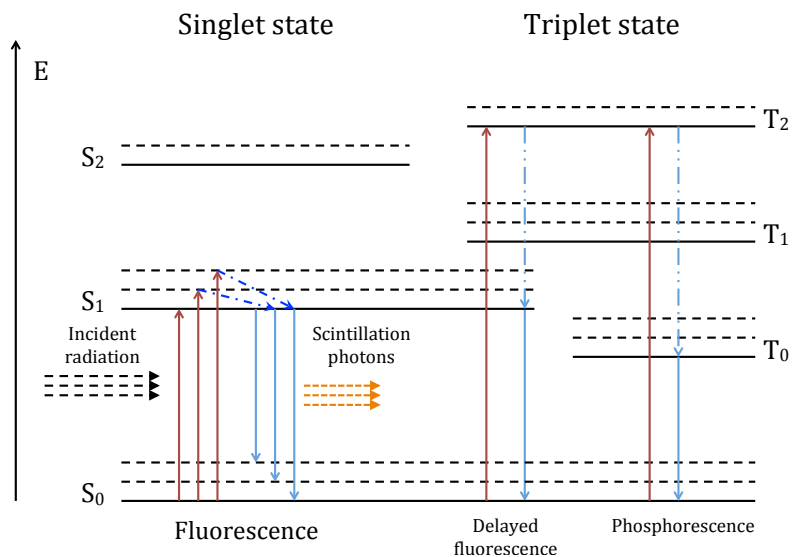
Figure 2.4: Scintillation mechanism occur in organic scintillator. Fluorescence generated through $S_1 \rightarrow S_0$. The same $S_1 \rightarrow S_0$ transition happen for delayed fluorescence but prior to that $T_0 \rightarrow T_0$ interaction between molecules of similar states. Phosphorescence is the slowest interaction where electron fall from $T_0 \rightarrow S_0$.

stable than singlet state, it takes more time for electron transit between these states ($\sim$100 ms). This is called delayed fluorescence. Another possibility is the electron from T_0 states falls directly to S_0 states producing UV photon of shorter wavelength. However, the probability of this process to occur is low. This is the phosphorescence component in scintillator.

However, the scintillation photons have a rather short attenuation length because their energies correspond to the definite energy states. To overcome this, fluor need to be added to the scintillator to help absorb the emitted UV photons and re-emit at longer wavelength. Another fluor is added to the scintillator called wavelength shifter. The function of the fluor is to absorb the UV photons and emit light photons.

2.2.3 Plastic Scintillators

Common plastic scintillators are fabricated using base material such as polystyrene, polyvinyltoluene and polymethylmethacrylate. It is made by dissolving one or more fluor to the base material. Plastic scintillators are inexpensive and come in different shapes of rods, sheets and fibers. Plastic scintillator has been used in a variety of detector applications. However, plastic scintillator is not the scintillation of choice when it comes to gamma spectroscopy. Probability of photoelectric effect is low in plastic scintillator due to its low atomic number. Therefore, only Compton edge can be seen when using plastic scintillator. Plastic scintillator is extensively used in particle detection [46][47]. Recently, studies has been done using plastic scintiillator for low energy X-ray in diagnostic radiology [48][49]

Scintillating fiber is a unique type of plastic scintillator that has scintillating fiber core cover with cladding. It has properties as optical fiber with added ability to scintillate light when radiation passes through the core. Depending on the size of fiber chosen, scintillating fiber has good spatial resolution that makes it good for particle tracking as well as for calorimetry application. Further discussion on scintillating fiber are discussed in section 2.4.1.

2.2.4 Light Yield

Light yield is perhaps the most important characteristic of scintillators. In any scintillator detector, it is the ultimate goal to collect as much as possible light emitted in the material. Low light output can cause degradation of signal-to-noise ratio. This is especially important for spectroscopic analysis. Light yield is measured by the number of photons per unit energy of incident radiation. Common scintillators yield between 20000-30000 light photons per MeV.

Plastic scintillator response to electrons is linear for energies above 125 keV. Figure 2.5 shows light output of common plastic scintillator material as a func-

tion of particle energy. Response to proton is less and nonlinear for much higher energies.
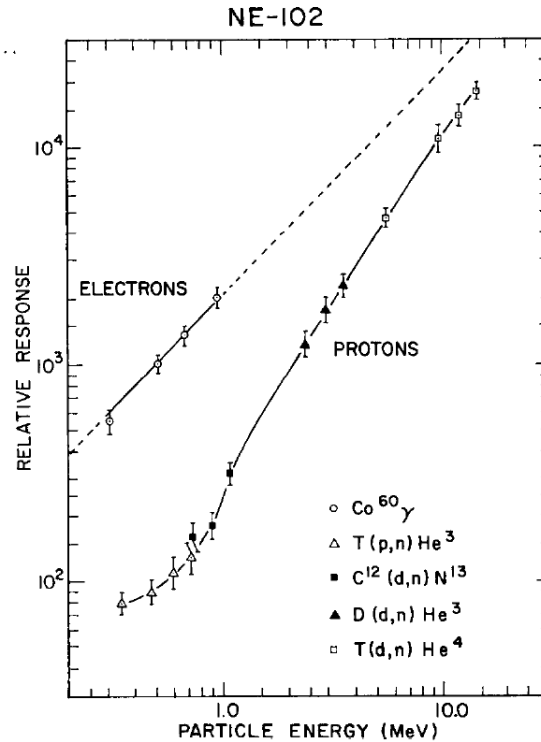
Figure 2.5: Relative light output by common plastic scintillator (NE-102) at different particle energies [2].

2.3   Photodetector

Scintillating light needs to be converted to an electrical signal for it to be useful for analysis. A photodetectors function is as a device to convert light to electrical signal. There are a few main technologies used for light detection and conversion. These technologies have their own pros and cons which, will be discussed in the following sections.

2.3.1 Photomultiplier Tubes

Photomultiplier tubes (PMT) are devices that can convert light to a large number of electrons. In general, a PMT consists of photocathode, series of dynodes and anode or readout electronics concealed in a vacuum tube. The components are illustrated in figure 2.6. Photons enter the PMT via a transparent window and hit the photocathode at the inner layer of the window. The photons get converted to an electron through the photoelectric effect. The electrons are accelerated towards the dynode placed behind the photocathode by the potential difference between dynodes. Each dynode is more positive than the previous one. Dynodes are metallic structure made of nickel or steel. More electrons are emitted at the dynode, and are again accelerated toward another dynode where more electrons emitted. This process is continuous until the electrons reach the anode. The anode will convert electrons into output current, which is measured by readout electronics.
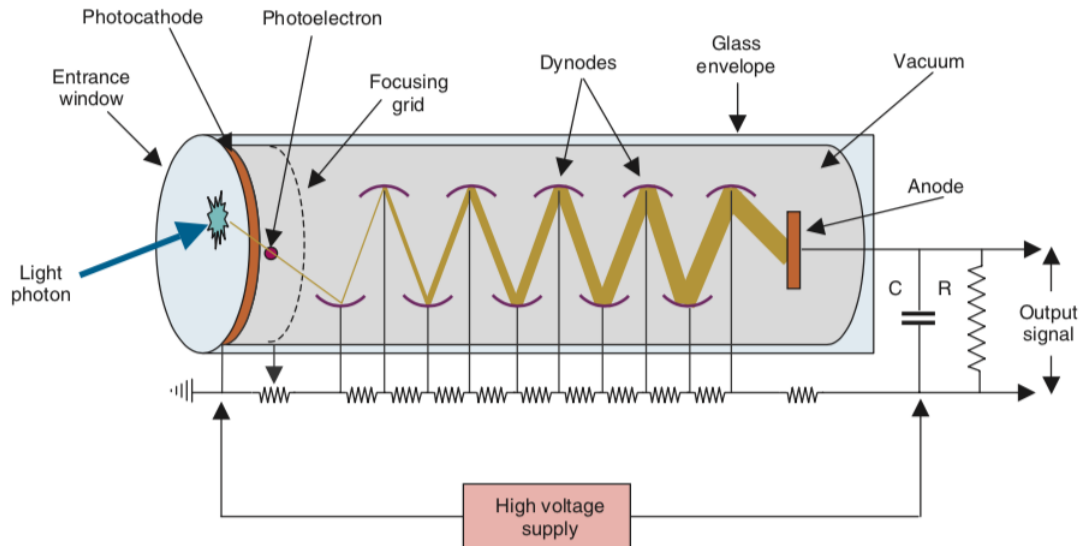
Figure 2.6: Longitudinal cut of a photomultiplier tube showing the basic working principle of the tube [3].

Among major advantages of PMTs are that they are extremely sensitive to light (UV, visible light and infrared), have fast time response and result in good signal-to-noise (SNR) ratio. As for the disadvantages, PMTs have low quantum

efficiency, are bulky size, operate at high voltage and are sensitive to magnetic field. Size is the one of the main factor when choosing photodetector for the proposed detectors system especially when the dimension of scintillators used are relatively small. Furthermore, it is preferable to have photodetectors that are not sensitive to magnetic field so the detector system can be use for PET-MRI devices. Recently, a μPMT, the smallest version of PMT, has been developed by Hamamatsu that can be operated with low voltage supply.

2.3.2 Photodiodes

PMTs are not the only means of detecting light photons. Photodiodes are a semiconductor photodetector. This detector has higher quantum efficiency and it operates based on a p-n junction in reverse bias.
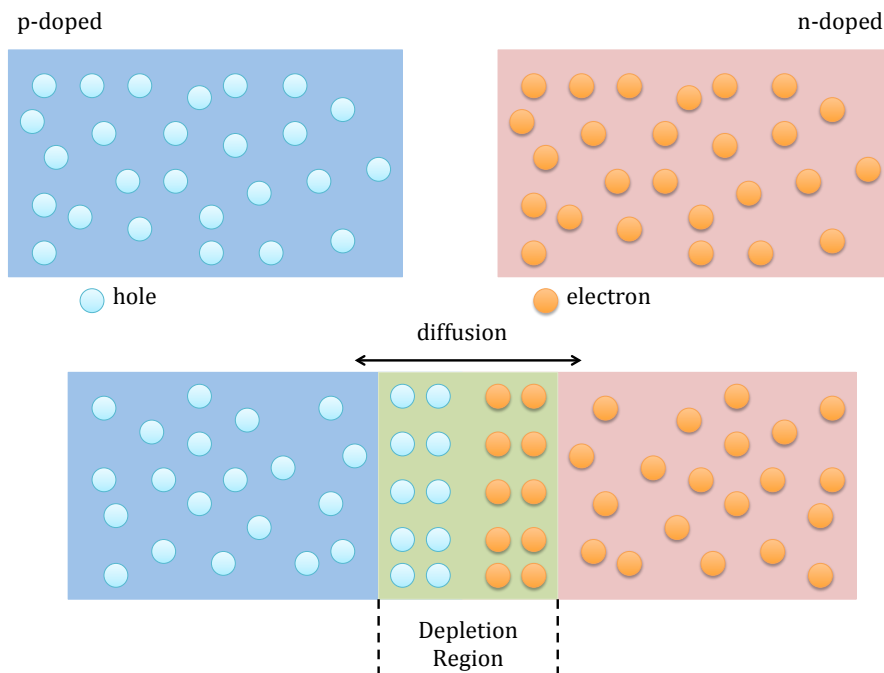
Figure 2.7: Schematic illustration of a pn-junction showing p-doped and n-doped semiconductor. When these semiconductor are in contact, electrons and holes recombine until it reach equilibrium.

Figure 2.7 shows the schematic diagram of the working principle of photo-

diode. The pn-junction is created by bringing two layers of semiconductor in contact to each other, one has p- and one has a n-dopant. This causes charge imbalance across the junction, and charges will flow automatically to compensate this imbalance. Diffusion of charges across this region is continuous until it reaches equilibrium. When it is at equilibrium, the region is called depletion region. When reverse bias is applied, the depletion is broadened. This is the active area where electron-hole pairs are produced by light photons via photoelectric effect. The electron and hole will drift to electrodes and produces current.

The pn-junction has a thickness in between 1-10 μm. Therefore, the junction cannot effectively be used since it is too thin. Furthermore, potential difference across the pn-juntion is very small. To increase the thickness of the active area, an undoped layer is added between the doped sides, this is called a PIN photodiode. Hence, signals produced are proportional to the light photon current. Although, amplification of the signal is not possible, therefore detection of single photon is difficult.

Avalanche photodiodes (APD) were introduced to deal with this particular problem. APD is a semiconductor photodiodes that converts light photons to electricity through photoelectric effect. The primary electrons produced by incident photons obtain high velocity due to the high external voltage applied. The electrons can produce more secondary electrons by impact ionisation process. The secondary electrons, being in the influence of the electric field produce tertiary electron and so on, and that process creates avalanche. Only one charge type is amplified in the APD for linear amplification and optimised noise. For silicone based APD, ionisation probability for electrons is higher than holes therefore only electrons produce the avalanche not the holes. Signals are amplified by the avalanche therefore increases signal-to-noise ratio, making it possible to detect low signal.

43

2.3.3 Silicon Photomultipliers

To be able to detect a single photon, higher gain is needed, APDs can achieve higher gain if operated at Geiger mode. APDs operating in this mode is called Geiger-mode avalanche photodiodes (GAPDs). In Geiger mode both electrons and holes produce avalanches while propagating to electrodes. It is possible only when bias is applied above the breakdown voltage. The avalanches can reach infinity, therefore, quenching resistors are required to stop the avalanche, so the system is ready for new electron-hole pairs. GAPDs are capable of detecting single photons.
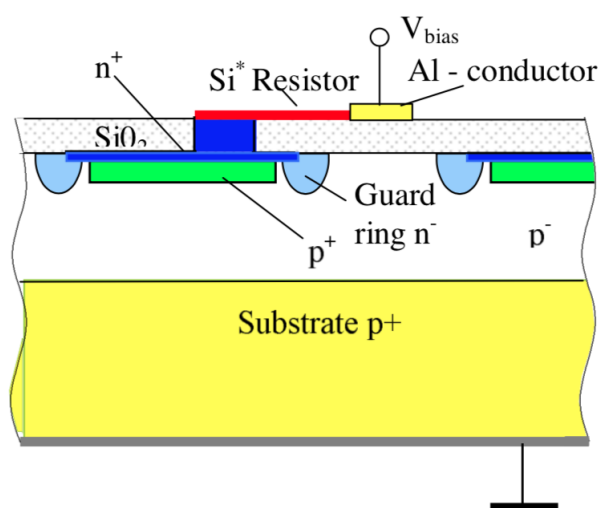
Figure 2.8: Cross section of SiPM microcell. The silicon resistor prove electrical coupling between pixels. Al strip connecting all microcells in order to sum up all readout signals[4].

Silicon Photomultipliers (SiPM) are photodetectors that consist of GAPD cells densely arranged and connected parallel to each other as illustrated in figure 2.8. These photodetectors have high gains and sensitivity. When a number of photon reach the device, these cause APD cells to saturate resulting in signals produced that are proportional to the number of photons. After it saturates, the APD becomes insensitive to new photons. The system require quenching resistor to reset the APDs to correct bias setting.

An important parameter for SiPM is the photon detection efficiency (PDE). The PDE is defined as the probability of converting light photons to electrical

signal. It is given as [4]

$$\varepsilon = QE.\varepsilon_G.A_{pixels}/A_{total} \qquad (2.3)$$

where QE is the quantum efficiency of the GAPD, ε_G is the probability of carrier created at the active pixel area to initiate Geiger mode avalanche and A_{pixels}/A_{total} is the filling factor of SiPM, indicating which fraction of the device is sensitive to photons. The overall photon detection efficiency of SiPM is around 20-30%.

SiPM has several advantages over PMT such as it is a more stable device, have low bias voltage, is insensitive to magnetic field, compact in size and is cost effective. Studies [50][51][52] have successfully show the potential of SiPM replacing PMT.

2.4 Scintillation Detectors

A scintillation detector essential elements are the scintillation material and photosensor optically coupled together. When radiation reaches a scintillator, it deposit energy and the material scintillates. The light will propagate through the scintillator until it reaches photosensor. The photosensor will convert lights to electric signals. Configuration of scintillator detectors depends on its application. However, there are general detector requirement that needs to be preserved such as sensitivity, linear response and fast response time.

The following section will discuss the scintillation detectors in relation to the work presented in the following chapters.

2.4.1 Scintillator Fiber

A scintillator fiber consists of a scintillating core which scintillate when radiation pass through it. It has cladding of a non scintillating material that has lower refractive index than the core. The fiber does not just act as the scintillator but it also helps to guide scintillating light in the fiber to the photodetector. The fiber standard diameter sizes are between 0.2 mm to 5 mm and are available in square and round shape. The thickness of cladding is in a few microns, usually 3% of the thickness of the core.
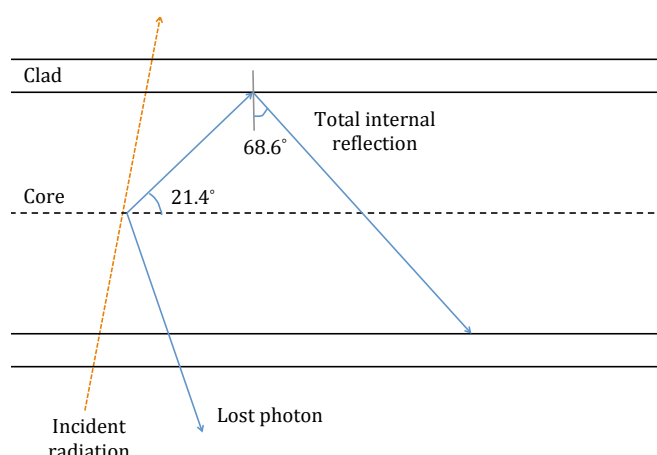
Figure 2.9: Longitudinal cut of fiber(Saint-Gobain BCF-10) showing total internal reflection angle.

Lights travelled in the fiber core are trapped by the total internal reflection of light at the core-cladding surfaces. Total internal reflection can only happen if the incident angle of incoming light is more than the critical angle. Figure 2.9 illustrates light propagation in a fiber scintillator. This can be explained by Snell's law as,

$$\frac{Sin\theta_a}{Sin\theta_b} = \frac{n_b}{n_a} \tag{2.4}$$

The angle of refraction depends on the angle of incident light and the refractive indices of interface media. To achieve this, the refractive index of cladding material

46

has to be lower than the core. If the incident angle is less than the critical angle, light photon will travel out of the fiber core.

Plastic Scintillating Fiber

Plastic scintillating fiber typically has polystyrene based, acrylic based or polyvinyltoluene(PVT) based core. Although PVT is a cheaper option and acrylic has better durability, plastic scintillating fibers are easily manufactured. With index of refraction of 1.59 and surrounded by acrylic cladding with refractive index of 1.49 single cladding plastic scintillating fiber has trapping efficiency within 3%. More recently, additional outer cladding with lower refractive index $n = 1.42$) was introduced to increase the critical angle, therefore increasing the trapping efficiency. Trapping efficiency of multicladding plastic scintillating fibers can reach up to ~6%[53].

About 80-90% of primary scintillating lights are lost rather rapidly. For thinner fiber, this may produce crosstalk between adjacent fibers. White or black coating, an extra-mural absorber, can be applied on the outer surface of scintillating fibers to prevent crosstalk. However, this layer would not change the trapping efficiency.

Scintillation efficiency of the fiber is 2.4%. This gives the photon yield approximately 8000 photons per MeV. The attenuation of light varies from 2.2 m to 4.0 m depending on type of scintillating fiber. The attenuation length is the length over which the light intensity fall by a factor of $1/e$.

Plastic scintillator has been the popular choice for detector application because of its flexibility, fast fluorescence time, better photon yield and longer attenuation length. However, among the disadvantages of plastic scintillating fiber are the problems of crosstalk between adjacent fiber due to poor trapping efficiency, that in turn reduce the efficiency of the fiber.

Glass Scintillating Fiber

Glass scintillating fiber has been favoured in particle tracking research. The glass fiber is doped with activator such as Ce+ or Tb+ for scintillating light. The core refractive index is 1.59 and surrounded by clear fused-silica glass followed by fluorinated polymer cladding with refractive index of about 1.51. The fiber dimension can easily be drawn to as small as 10μm due to the material strength. The trapping efficiency in glass scintillating fiber is about 3%.

Quantum efficiency of Ce-doped glass is rather low, 5000 photons per MeV, meanwhile for Te-doped quantum efficiency is approximately 8000 photons per MeV. Although Tb-doped glass has higher photon yield, long decay time (msec) has limit its application to low flux beam. Glass scintillating fiber has poor attenuation length (2.2-2.5 cm) compare to plastic scintillating fiber.

In glass fiber, the light emission is produced in close proximity to the original energy deposition that will give better tracking accuracy. Therefore, it will not suffer from signal crosstalk. Another advantage of glass scintillator is that it has a fast fluorescence time and compare to plastic scintillating fiber, it can withstand radiation up to 10^6 rad.

Liquid Core Scintillating Fiber

The liquid core scintillating fiber is known to function the same way as plastic and glass fiber. The fibers have diameter ranging from 15-200 μm and are formed from thin glass wall filled with liquid scintillator. With an appropriate choice of liquid scintillator, the performance characteristic of liquid fiber is comparable to plastic and glass fiber. The liquid fiber can possibly obtain high photon yield (10000 per MeV), fast response time, large attenuation length ($\sim$3 m), and higher trapping efficiency (7.5%).

The liquid core scintillator fibers are usually in the form of capillaries of 20-

25 μm diameter. They are bundled together in a glass tube. Example of liquid scintillating fiber is shown in figure 2.10.
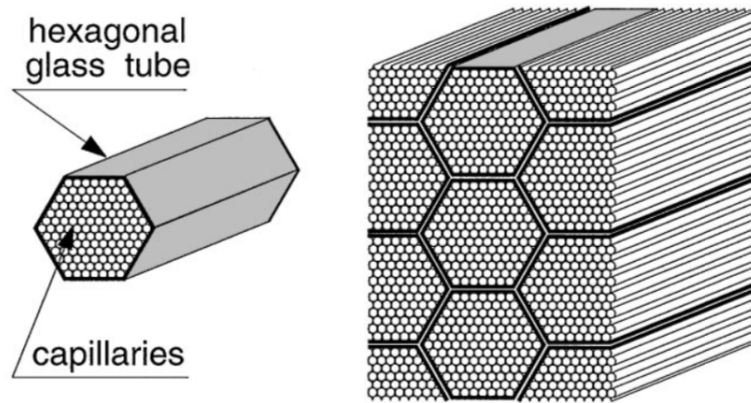
Figure 2.10: Diagram showing bundle of capillaries containing liquid scintillator arranged in hexagonal glass tube. Adapted from [5].

Table 2.1 summarizes the properties of the plastic scintillating fiber, glass scintillating fiber and liquid core scintillating fiber.

Table 2.1: Properties of different types of scintillating fiber.

Properties	Plastic	Glass	liquid core
Photon yield, per MeV	8000	5000-8000	10000
Refractive index	1.59	1.59	1.52-1.62
Attenuation length, cm	220-400	2.2-2.5	300
Trapping efficiency, %	3	3	7.5

2.5 Microfluidic

Microfluidic technology is an analytical technology that utilises small amount of fluid in channels of micrometer in dimensions. It has been extensively used in chemistry[54] and biotechnology[55][56] laboratories. The microfluidic concept has been manipulated in laboratories to allow usage of minimal amount of chemical reagents and samples and reducing cost. This technology has also shortened anal-

ysis time as well as has a small footprint. The key concept of microfluidic is integrating network of channels operations in a microsize system.

Microfluidic chip is the tool used for microfluidic analysis. Material of microfluidic has gain large interest. It is because in microscale, the surface properties of channel are greatly influenced by the device material and that is largely affecting the performance of the device. Therefore, choosing suitable material is the first crucial part in microfluidic fabrication. Various materials have been introduced in microfluidics but among the most used are glass and elastomer. Glass is transparent, insulating and resistance to inorganic solvent. However, the cost of fabricating glass microfluidic is high and dangerous as it involves dangerous chemicals (e.g HF)[57]. This has motivated the used of easily fabricated material such as elastomer. Elastomer is inexpensive and flexible to fabricate complex channel network. The drawback of using elastomer is that it is permeable to gas. Although gas permeability is favourable in some application, it also can lead to absorption of fluid molecules in the channel walls.

Due to its small size, microfluidic fabrication technique has been adapted from the fabrication of semiconductor industries. Microfabrication techniques such as micromachining, replica moulding, embossing and photolithography are commonly used to fabricate microfluidic chip. Micromachining is a more costly technique. It requires a clean room and involves techniques i.e wet and dry etching and photolithography. Material suitable for micromachining is glass and silica. Figure 2.11a is illustrating fabrication of glass microfluidic chip. A more economical technique is adapted for elastomer. Replica molding is a simple technique done by pouring elastomer mixture directly onto the silicon master and cured in 60°-70° for two hours (figure 2.11b). It is also a fairly fast process. Without the need for clean room, this technique can easily implemented in any laboratories.
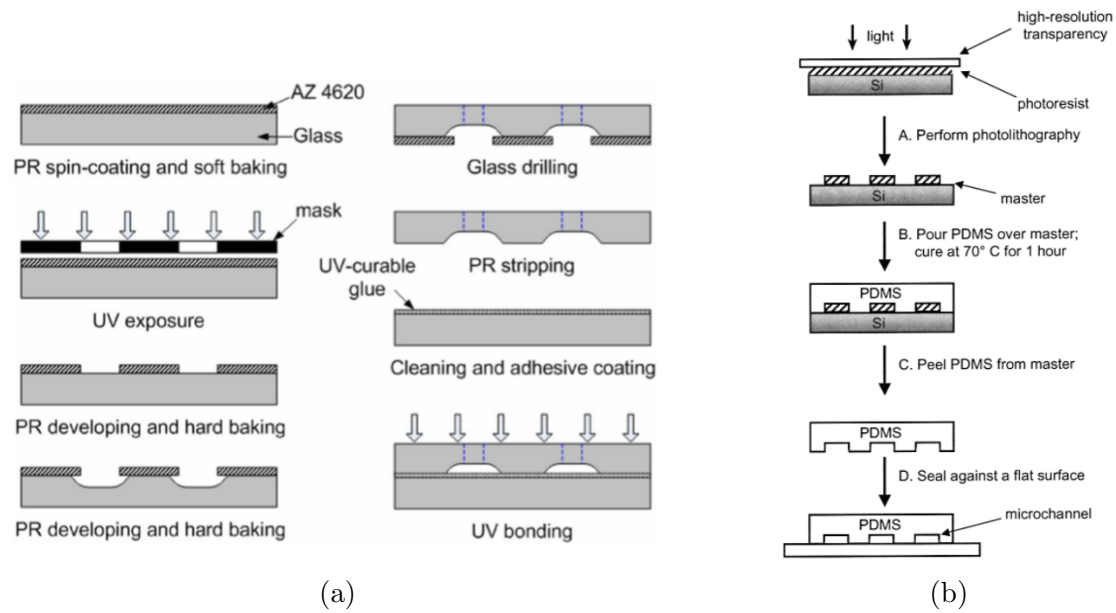
Figure 2.11: (a)Schematic diagram showing photolithography and wet-etching technique involve in fabrication of glass microfluidic chip. Adapted from [6], (b)Schematic diagram showing photolithography and wet-etching technique involve in fabrication of PDMS microfluidic chip. Adapted from [7].
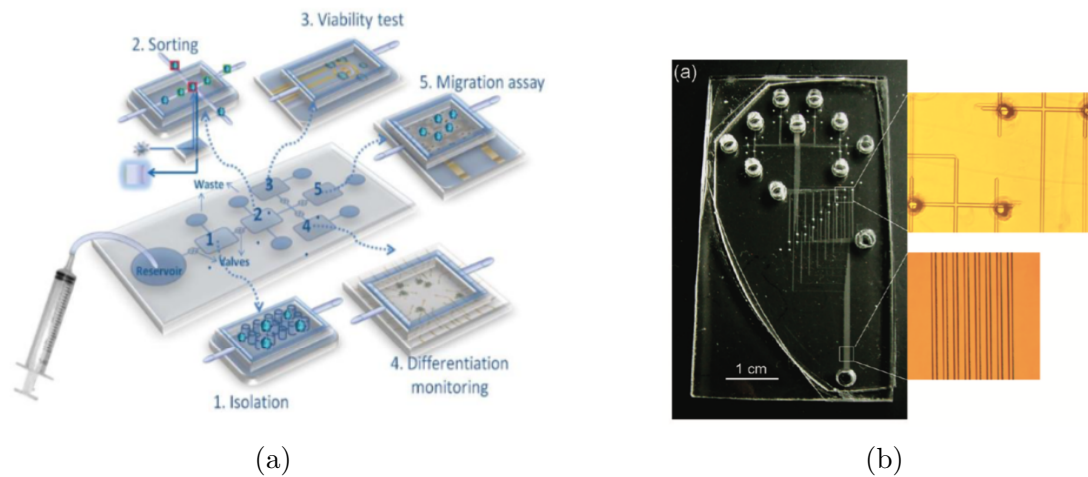
Figure 2.12: (a)Schematic diagram showing chain of microfluidic channel interconnected forming a miniature laboratory. Adapted from [8], (b)photo showing micofluidic chip network constructed in multiple layers. Inset on the top right are showing fluidic channel of first layer and bottom right is showing second layer. Adapted from [9].

The fluidic channel designs are an important aspect in microfluidic function. The earlier design of channel was a single line channel only limited for certain analysis. With the wide benefits of microfluidics in various fields, the design of fluidic

channel has become more complex. It can consists of multiple layers of channels or chains of channels interconnected to each other[9]. Integrating a network of channels to a wide range of microfluidic component such as pumps, valves, mixer and flow sensor, offers versatility to the microfluidic system. Figure 2.12a and 2.12b showing examples of fluidic channel network in microfluidic system. This system of microinstrument that can carry out biological and chemical processes is called Lab-on-chip (LOC). The addition of the proposed microfluidic detector to the LOC network system will compliment the existing system in quality control and radioactivity assessment for PET radiotracer production.

Chapter 3

Geant4 Simulation of Prototype Design Foundation

This chapter presents the simulation done to evaluate the design of the microfluidic detector and beta probe detector. In section 3.2, simulation of microfluidic detector module design are discussed by investigating the positron penetration depth in plastic scintillation material and the effect of channel dimension on counts detected. While in section 3.5, the scintillation fiber module design are reported by analysing spatial distribution of scintillating fibers.

3.1 Introduction

In most experiments, research and development can be conducted using simulation without the need to have the real prototype. Simulations are helpful in predicting results of an experiment that is impractical to perform.

Prior to fabricating the microfluidic chip and β-probe prototypes, simulation work was done to evaluate the expected performance of the proposed detector system. This is an effective method to optimise the development of miniature detectors that produce low photon statistics. The simulation deals with optical propagation and distribution within the devices.

GEANT4[58][59] toolkit is a Monte-carlo simulation that is used for simulating particle transportation in matter. The software offers flexible detector and physics modelling. It allows users to modify geometry description, physics processes, managing hit events and detector response.

In this research, GEANT4 was used to assess the key characteristics of the microfluidic scintillation detectors and fiber scintillating probe in particular optimising photon collection and determining the feasibility of the detectors as a β radiation counting system.

3.2 Microfluidic Chip Cetector Module

The Microfluidic chip was developed based on the need for low detection volume for a miniaturised detector system. A cross sectional view of the planned prototype is shown in Figure 3.1. Essentially, the fluidic channel is milled on the top layer of a material. The channel will then be sealed on top of the plastic scintillator. Finally, SiPM is attached to the bottom of the plastic scintillator for photon detection. For the purpose of simulation, the geometry of the channel is kept as a simple hollow cuboid tube with 6 mm and 12 mm length but varying width and thickness to

keep the volume constant.
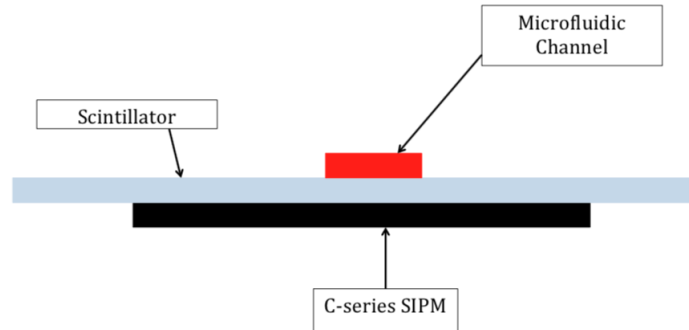
Figure 3.1: Illustration of a simple microfluidic detector setup featuring the fluidic channel volume on top of a plastic scintillator.

In scintillation detector, it is crucially important to maximise the number of photon detected in the photodetector. Thus, this simulation study examines the relationship between photon count and scintillator thickness for two different channel lengths. The aim is to optimise the channel design to maximise the number of photons detected.

3.2.1 General Simulation Parameters

All simulations were performed using GEANT4 Ver. 10.1.03. It was modified from an existing example in GEANT4 toolkit. OpNovice is a documented example that demonstrates optical photon generator and transportation in matter.

Geometry

The detector construction class is responsible for modelling the detector geometry, assigning the bulk material and optical properties. The simulated Microfluidic chip detector is shown in Figure 3.2. A $0.5 \times 0.5 \times 1$ mm^3 and $0.5 \times 0.5 \times 2$ mm^3 plastic scintillator was simulated with polished surfaces, and a 0.025 mm glass window was placed behind the plastic scintillator. It acts as the readout

55

(a)

(b)   (c)
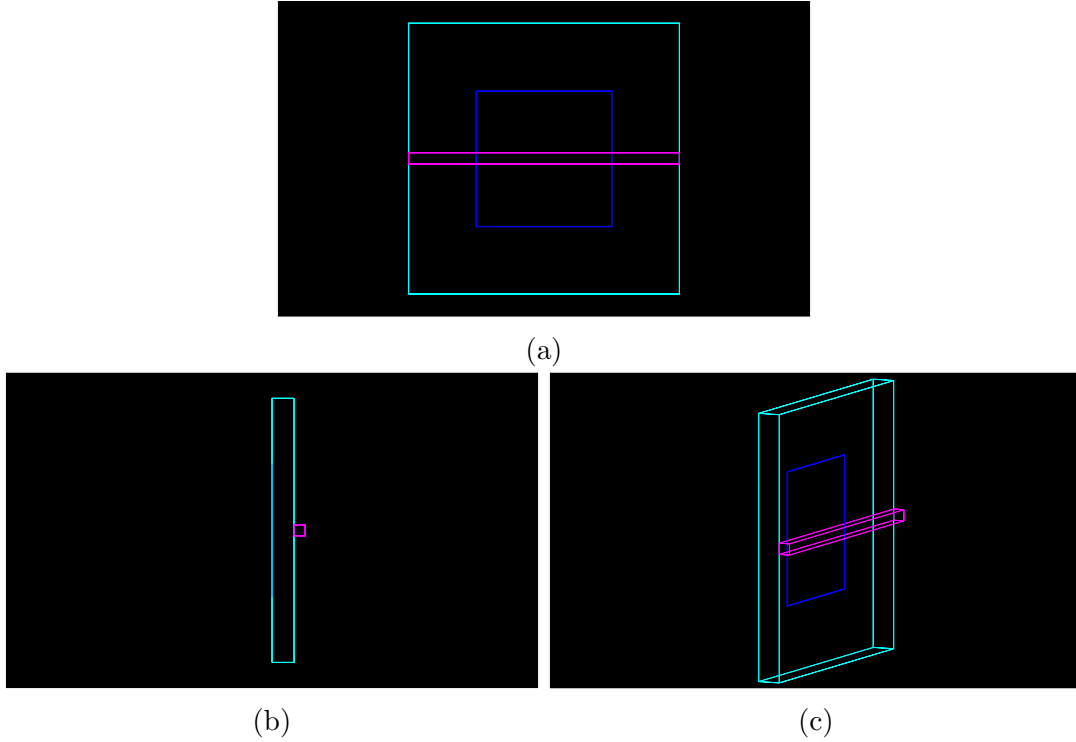
Figure 3.2: Drawing showing the simulated microfluidic detector. The dark blue line represents the photodetector volume, the green line represents the plastic scintillator volume and the pink line represents the fluidic channel volume.

plane or as the sensitive detector. The physical volume of the actual microfluidic was attempted but it has given errors, therefore the volume of micro channel was constructed as a simple hollow cuboid volume. This may not affect the simulation data significantly as PDMS has a low autofluorescence[60]. On the front of the plastic scintillator surface, a cuboid channel was placed. The channel dimensions are modified according to the requirement of analysis, and will be mentioned in a later section. The whole detector is covered by a layer of Teflon, acting as a white diffusive reflector. The main characteristics of the detector materials are summarized in Table 3.1. The glass window, which acts as the photocathode, is assigned as sensitive detector in the simulation.

Table 3.1: Properties of materials as defined in the simulation.

Material	Base	Scintillation yield, (/MeV)	Refractive index	density, (g/cm^3)
Scintillator	Polyvinyltoluene	10000	1.58	1.023
PTFE[61]	Teflon	-	1.36	2.20

To emulate photon reflectance on surfaces, the GLISUR model was used to simulate photon propagation between "dielectric-metal" surfaces by assigning a polish coefficient while the UNIFIED model was used for "dielectric-dielectric" surfaces. The UNIFIED model has various surface type, "ground-back-painted" is used between scintillator-teflon surfaces to model the diffusive reflector. The surface roughness for this model assumed to consist of micro-facet, which assumed to consist of microscopic small surfaces. The degree of roughness is defined by the standard deviation of microfacet distribution around the surface normal(σ_α). σ_α for polished surface is equal to 0. The type, finish and value of σ_α of each of the optical interfaces in Figure 3.2 are given in Table 3.2.

Table 3.2: Type and surface finish of each of the optical interfaces defined in the simulations.

Optical interface	Type	Finish	σ_α	Reflectivity
scint-photodetector	dielectric-metal	polished	0	1
scint-Teflon(PTFE)	dielectric-dielectric	groundbackpainted	0.1	0.97

Physics Processes and Detector Hits

The *Physicslist* class lists all the processes involved in the interaction. For this simulation study, the relevant processes are the electromagnetic process, optical processes and radiation decay. A *Hit* is created when a particle or photon deposit energy in a sensitive detector and stored in *hit collections*. The simulation stores all the tracking information of the hit. This study was primarily looking at the amount of photons arrive at the glass window and number of particle hitting the scintillator. Additional tracking information was also used to support the output of the simulation such as the path length and energy deposited by the particles and photons.

Therefore, there are two *hit* classes for this simulation work. The *Scinthit* class stores hits when a beta particle hits the scintillator. Hit information includes

particle type, energy deposited, position and *scintillator id*. The *glasshit* or in this case called as *SiPMhit*, stores number of scintillation photons, position, energy and *SiPM id*. However, realistically not all photons reaching the glass window are detected. It depends on the photon detection efficiency (PDE) of scintillator.

Primary Particle Generator

G4VUserPrimaryGeneratorAction is the class to control the generation of primaries. GEANT4 provides *G4GeneralParticleSource* (GPS) as a concrete class of this base class. GPS is capable of randomizing kinetic energy, position and/or direction following a user-specified distribution. GEANT4 also offers a radioactive decay module, which generates all the decay components radiated from a specified source. In this study, the GPS and decay module are used to simulate ^{18}F and ^{68}Ga isotropically which are randomly distributed in the micro channel.

3.3   Positron Range Calculation

Prior to the fabrication of the microfluidic detector, a number of studies were done to guide the choice of the thickness of scintillator and dimensions of the fluidic channel. The aim is to optimise the amount of photon collection while still utilises micro volume radioactive solution.

In the scintillator, the photon yield is affected by the amount of energy absorbed. Thus, it is the main objective to increase energy deposition by particles in the detector active volume. This is proved difficult when developing a miniature detector.

Positron interaction in matter is assumed to be similar to electrons as both have the same mass and only differ in the charge. The range of particle in matter can be calculated using an empirical equation 3.1 in g/cm^2,

$$R = 0.412E^{1.27-0.0954lnE} \tag{3.1}$$

where E is particle energy in MeV. This investigate the penetrability of positron for ^{18}F and ^{68}Ga at their average energies, 249.3 keV and 829.5 keV respectively. Using equation 3.1, the calculated positron ranges are 0.0571 cm and 0.3048 cm for ^{18}F and ^{68}Ga in plastic scintillator(PVT based) with the density of 1.032 g/cm^3.

In a web database Estar, the continuous-slowing-down approximation (CSDA) range was obtained by integrating the reciprocal of the total stopping power with respect to particle energy. CSDA range data for PVT based plastic scintillator obtained from Estar are plotted in figure 3.3. CSDA range of ^{18}F positron is approximately 0.0641 g/cm^2 at 250 keV and ^{68}Ga positron of 830 keV is 0.3504 g/cm^2. If we are to consider the maximum beta energies for both radioisotope, the CSDA ranges are 0.2459 g/cm^2 for ^{18}F at 633 keV and 0.9411 g/cm^2 for ^{68}Ga at 1899 keV.
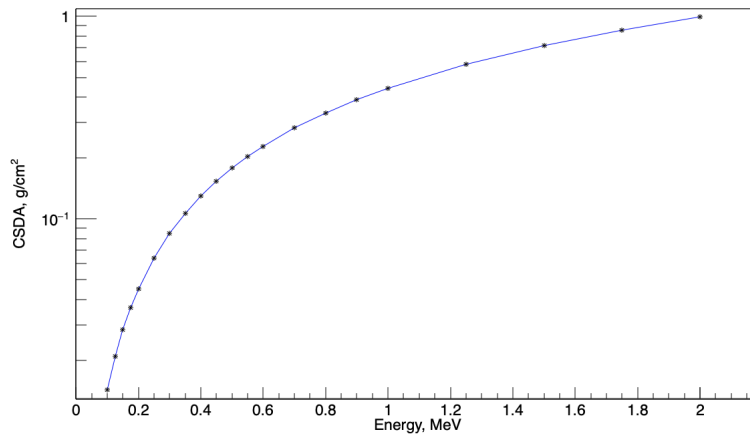
Figure 3.3: Range of positron/electron in PVT based Plastic scintillators obtained from EStar database[10].

3.3.1 GEANT4 Positron Depth Simulation

A simulation analysis was done to simulate the range of positron particle emitted by radioactive in the micro channel. 30000 events were emitted towards the plastic scintillator.
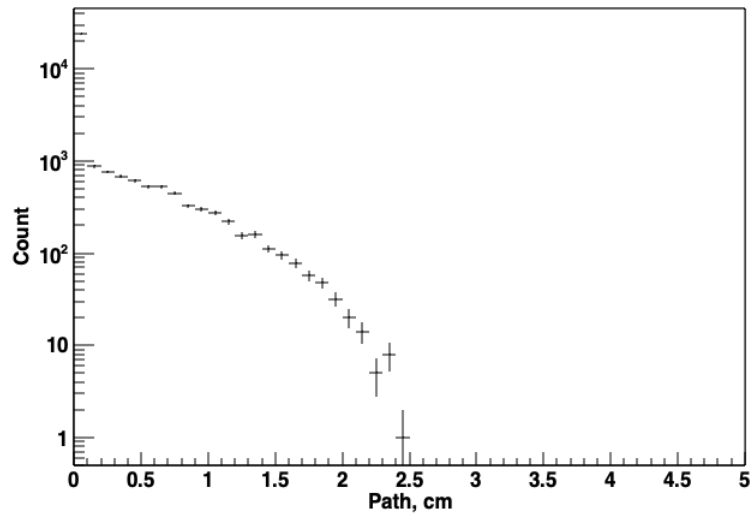
Figure 3.4: ^{18}F positron particles counts detected in a plastic scintillator as a function of depth.
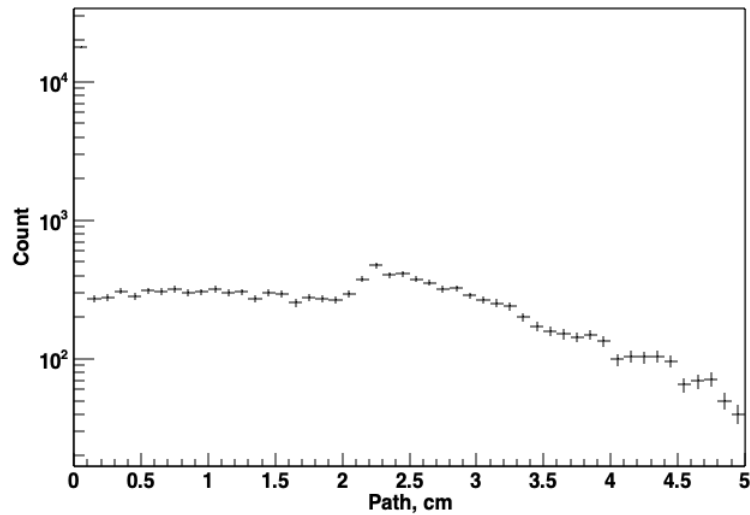
Figure 3.5: ^{68}Ga positron particles counts detected in a plastic scintillator as a function of depth.

The result of the simulation are shown in Figure 3.4 and 3.5. The histograms

are showing positron counts as a function of depth in plastic scintillator. The maximum depth of the positron particle is approximately at 2.4 cm for ^{18}F and approximately 5.0 cm for ^{68}Ga for the proposed microfluidic detector configuration. The maximum range for ^{18}F from the simulation agrees with the CSDA range from EStar. The 50 mm plastic scintillator is enough to stop all positrons from ^{18}F. However, 50 mm is not enough to stop higher energy ^{68}Ga positrons therefore the range obtained from GEANT4 does not represent the maximum positron range of ^{68}Ga.

3.4   Effect of Channel Dimensions

The microfluidic channel was constructed to allow more beta particles to interact with the scintillator material. The way to achieve this, is by increasing the volume of radioisotope solution. Since reducing the detection volume is the main aim of the thesis, increasing the detection volume is not favourable for this prototype detector, therefore a different approach was proposed by manipulating the fluidic channel dimension.

| (a) | (b) |
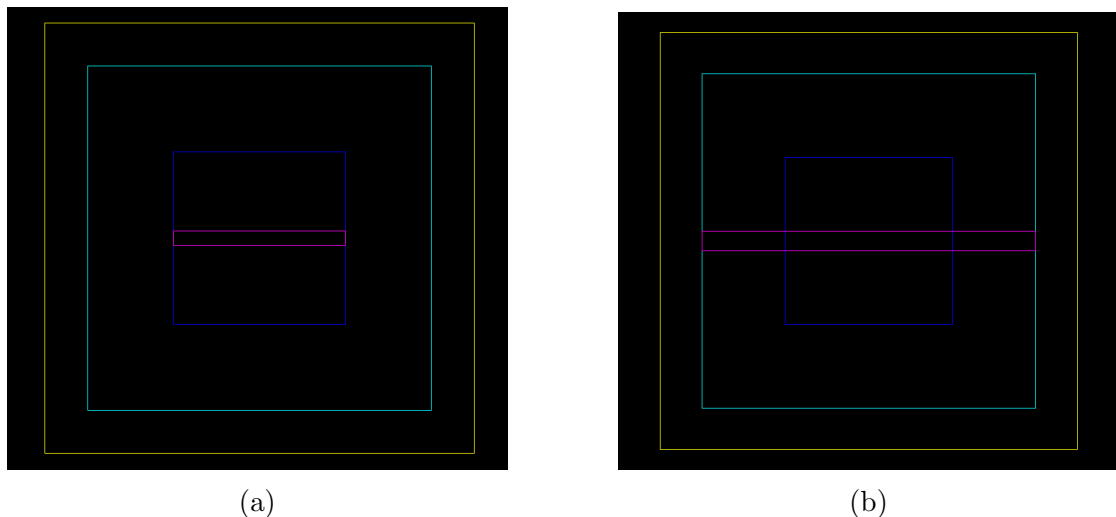
Figure 3.6: Drawing of the simulated channel in pink (a)$6 \times 0.5 \times 0.5$ mm^3 (b)$12 \times 0.35 \times 0.36$ mm^3 micro channel configuration.

In this simulation test, the channel volume was kept constant at 1.5 μL. The

changes were made on the length and thickness of the fluidic channel. The channel dimension simulated was $6 \times 0.5 \times 0.5$ mm^3 and $12 \times 0.35 \times 0.36$ mm^3. Drawings and photons distribution of the effect of channel dimension for ^{18}F is shown in Figure 3.6 and 3.7, for the two channels respectively.
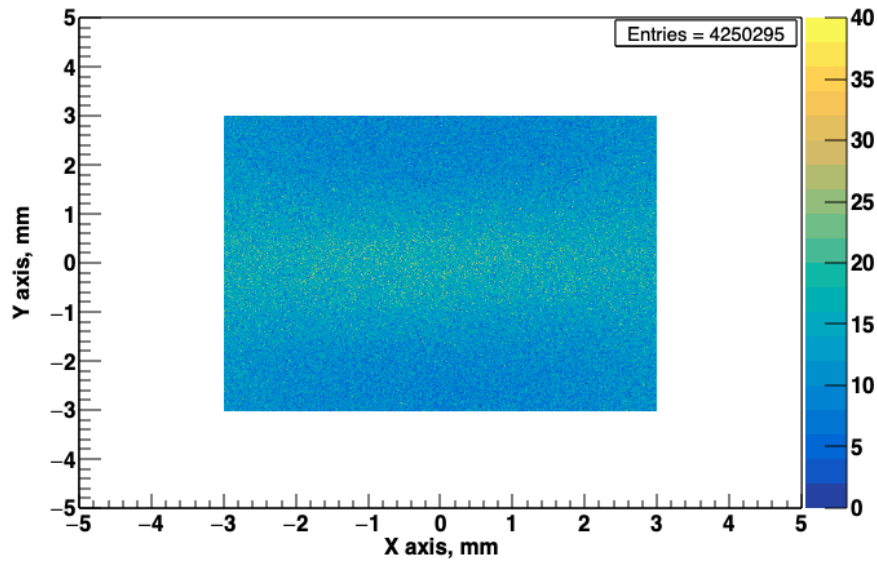
(a)
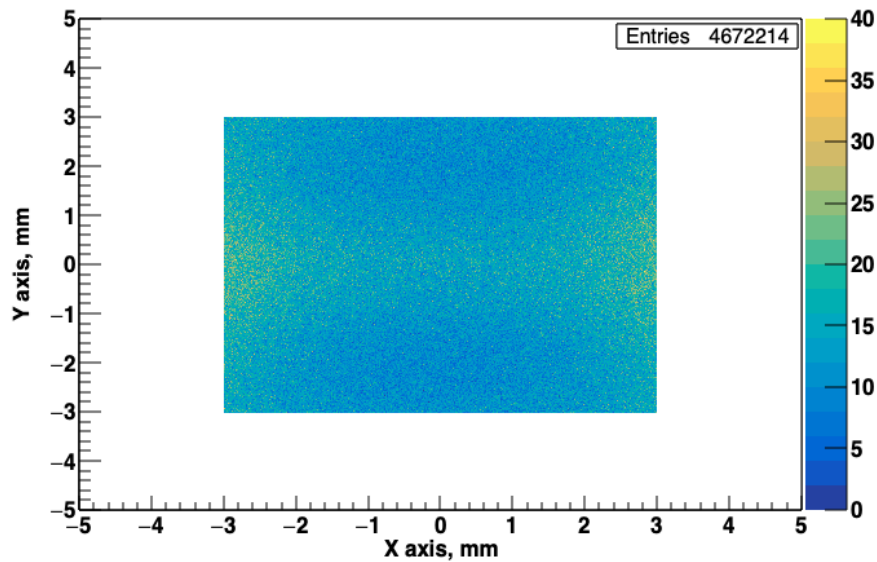
(b)

Figure 3.7: Spatial distribution of photon hits deposited on glass window from the (a)$6 \times 0.5 \times 0.5$ mm^3 (b)$12 \times 0.35 \times 0.36$ mm^3 micro channel configuration.

Figure 3.8 shows the simulated energy spectrum of ^{18}F from the short and long micro channels. The spectrum show continuous distribution of beta spectrum where 5928 positrons were detected on the short channel and 7144 on the long channel.

(a)   (b)
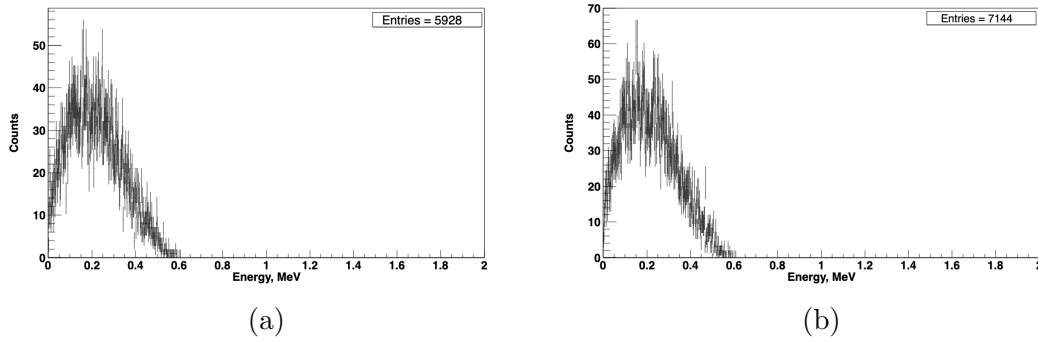
Figure 3.8: Energy spectra of ^{18}F obtained from GEANT4 simulation from (a)$6 \times 0.5 \times 0.5$ mm^3 (b) $12 \times 0.35 \times 0.36$ mm^3 micro channel configuration.

More photons were detected with the longer channel, more photons were detected with more counts were detected on the lateral edges of the channel compare to the short channel. Total photon detected in the short micro channel was 4250295 while long channel total photon counts was 4672214, that gives an increase of 9.0% photon detected on the glass window. The longer and thin channel is more efficient as it has slightly increase the detection efficiency as evidence in figure 3.7 and 3.8. The loss of detection efficiency for low energy particle is much less significant with the longer channel.
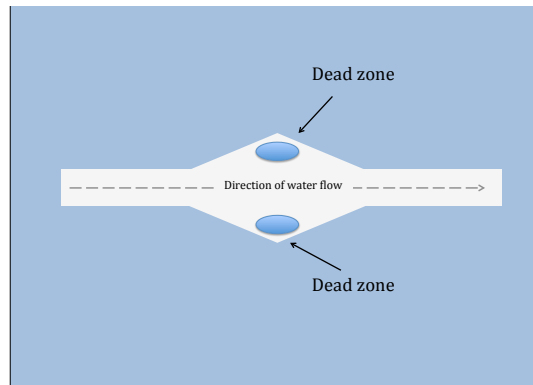
Figure 3.9: Illustration of dead zone area that can cause fluid trap in micro channel.

These GEANT4 findings are important for the fabrication of the microfluidic detector. From this simulation, it was found that the length and depth of channel influence the detection. The findings suggest that the photon detection rate will be maximised by having the microfluidic detector with a longer and thinner channel. To have a thin channel, the width of the channel must be widen, in order to maintain the volume of the channel. In addition, wider channel will increase the area of detection, however, realistically this is not possible. The width of the channel must be identical to the diameters of the inlet and outlet tubes to ensure fluid in the channel can easily be flushed out after measurement. Wider channel will create dead zone or trap fluid, as visualise in figure 3.9.

3.5 Scintillating Fiber Module

The simulated fiber detector is simply a fiber positioned on a photo sensor without wrapping as illustrated in figure 3.10. The fiber cladding function is to trap photon in the fiber core and let it propagate towards the photodetector. The main question when developing this β-probe is how any photons are produced in the fiber core as a result of the geometry of the fiber being small in size. In addition to that, the fibers small trapping efficiency only permits the propagation of less than 4% of the scintillation photon produced in the fiber core which will degrades the detection.
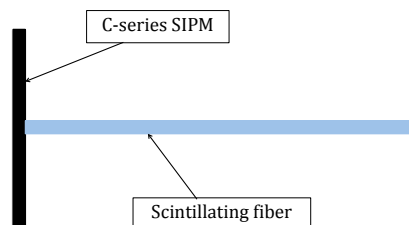
Figure 3.10: Illustration of a simple beta probe detector setup showing the fiber(blue) on a photodetector(black).

3.5.1 General Simulation Setup for Beta Probe

In general, simulation parameter setup for the fiber is similar to microfluidic chip as discussed in section 3.2.1. The fiber probe simulation code is a modification code from OpNovice example in GEANT4 document.

Fiber Geometry

(a)

(b)   (c)
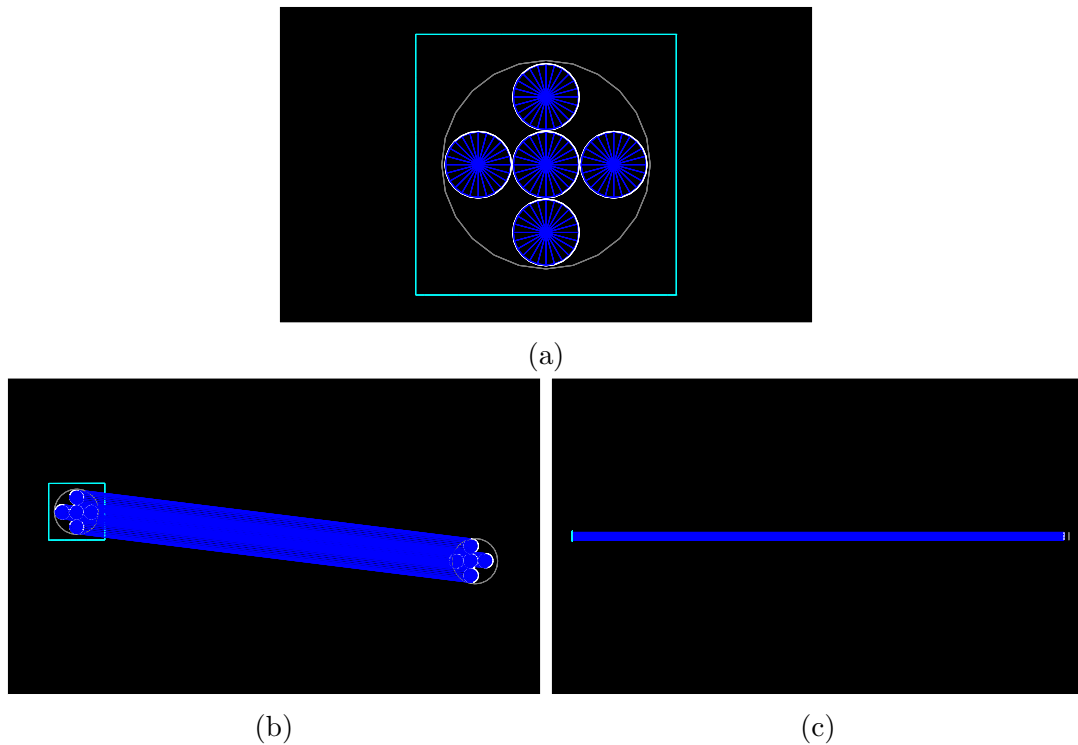
Figure 3.11: Drawing of the simulated fiber detector showing five fibers(dark blue) covered by reflective paint geometry. The photodetector(green) is placed at the fiber end.

The fiber detector was designed by placing a fiber of 250 μm diameter on a 1×1 mm^2 glass window. The glass window is a *physicalvolume* assigned as the readout plane. Initially, no reflective paint volume was introduced around the fiber detector assembly, since the cladding is there to trap photon in the fiber core. Photons reflecting at the surface between fiber core and the cladding should follow Snell's law. Detail properties of the materials and surface type are summarised in

65

Table 3.3 and 3.4 and simulation drawing of the geometry for 5 fibers is shown in Figure 3.11.

Table 3.3: Properties of materials assigned in the fiber simulation.

Material	Base	Scintillation yield, (photon/MeV)	Refractive index
bcf12 core[53]	Polystyrene	∼8000	1.60
bcf12 clad[53]	Acrylic	/	1.49
Reflective paint[62]	Titanium Dioxide	/	1.61[61]

Table 3.4: Type and surface finish of each of the optical interfaces defined in the fiber simulations.

Optical interface	Type	Finish	σ_α	Reflectivity
core-sipm	dielectric-metal	polished	0	0
clad-paint	dielectric-dielectric	groundbackpainted	0.1	0.955[61]
core-clad	dielectric-dielectric	polished	0.3	1

A surface boundary was introduced on the fiber to glass window surface. Here, the GLISUR model in GEANT4 was used between "dielectric-metal" surface and the surface finish was set to polished. In GEANT4, reflectivity can be set between 0 to 1, 0 means 100% absorbing and 1 means 100% reflecting. In this simulation reflectivity fiber to glass window was set to 0. Therefore, any photon hitting the glass window surface will be absorbed and counted as hit depending on the photon detection efficiency of photodetector. This is set only for the purpose of single fiber analysis to simulate the intrinsic properties of the scintillating fibers. As the study is only concerned with the number of photons hitting photodetector, no further photons simulation is needed beyond the glass surface.

3.5.2 Single Fiber Analysis

Reflector

A simulation of the fiber response has been performed without and with reflective paint. In both cases, the fiber was simulated in the vacuum environment with 5000 events of positron of monoenergetic 633 keV energy to mimic the maximum energy of ^{18}F placed on the center of the long edge of the fiber firing towards negative -Y axis direction.
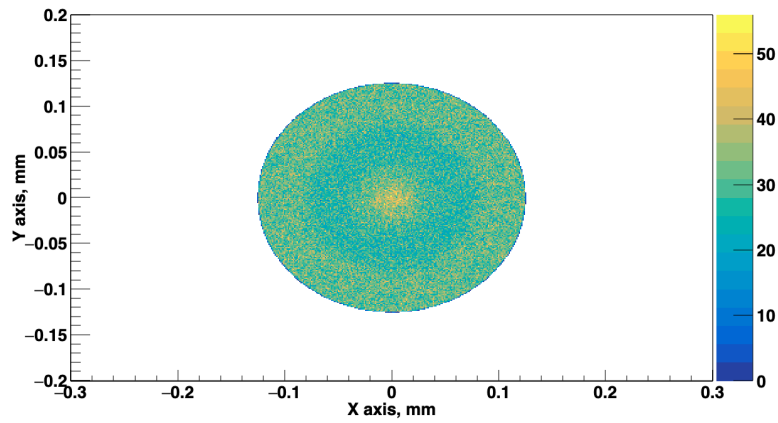
(a)
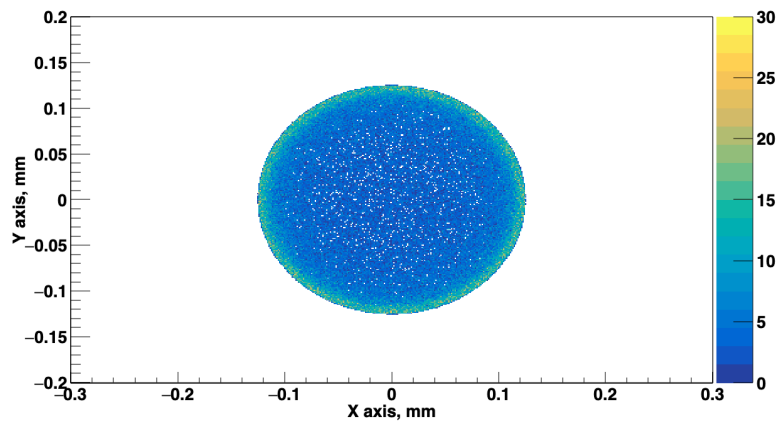
(b)

Figure 3.12: 2D photons distributions of single fiber at the fiber end (a)without reflective paint and (b)with reflective paint.

Figure 3.12a and 3.12b showed the XY spatial distribution of the simulated

photon reaching the fiber end, for simulation without and with reflective paint respectively. About 179203 of photons were detected on the photodetector from fiber simulation without reflective paint while 1022173 photons were detected from fiber simulation with 0.11 mm thick of reflective paint. It is evidenced that Snell's law is obeyed in these simulations. As can be seen in figure 3.12a, more photons we being trapped when simulation was performed without reflective paint. This is due to a much lower refractive index of air as compared to the reflective index of paint (1.0027 and 1.6100 respectively) and this will lead to more photons undergoing total internal reflection on clad-to-air surface. Meaning that more photons will escape the fiber at clad-to-paint surface because the critical angle is much smaller than the critical angle at clad-to-air surface. High counts on the borders of the fiber are due to the skew rays and high count on the axis of the fiber is caused by meridional rays. In theory, skew rays have higher trapping fraction compare to meridional rays[41][63]. For this reason, distribution in 3.12b shows only counts detected due to skew rays as most of the meridional rays might have escape the fiber.

Since the majority of the photon produced travel along the fiber border for both cases the photodetector should therefore be at least as large as the fiber cross section. While the result without paint is better, this setup is rather impossible to achieve because without wrapping, external photon might interfere with the measurement value.

Fiber Properties

The fiber thickness is negligible compared to its length, therefore, the photons produced in the fiber depend on the amount of energy deposited in the fiber and where the particle crosses the fiber. Positron crossing at the center of the XY plane of fiber will deposit more energy when compared to a positron crossing off center. This can be explained simply by the difference in the path length taken by positron in the fiber core. Due to this phenomenon, the following work is being

68

done to simulate the optical properties of the fiber in order to obtain the correct trapping efficiency and also to collect the correct amount of light on the photon detector surface.

The dependence of the number of photons generated from the energy deposited in the fiber end is shown in Figure 3.13. The mean energy deposited in the fiber is 46.6 keV. From figure 3.13, 46.6 keV deposited energy corresponds to about 6 detected photons. Given that the trapping efficiency provided by manufacturer is 3.44 %, the fiber would have produce 407 photons in the fiber at 46.6 keV. This will give an average of 8 photons per keV of positron particle, which agrees to the fiber photon yield provided by manufacturer. This shows that the fiber optical surface properties are able to collect correct amount of photon and matches standard scintillating fiber trapping efficiency.
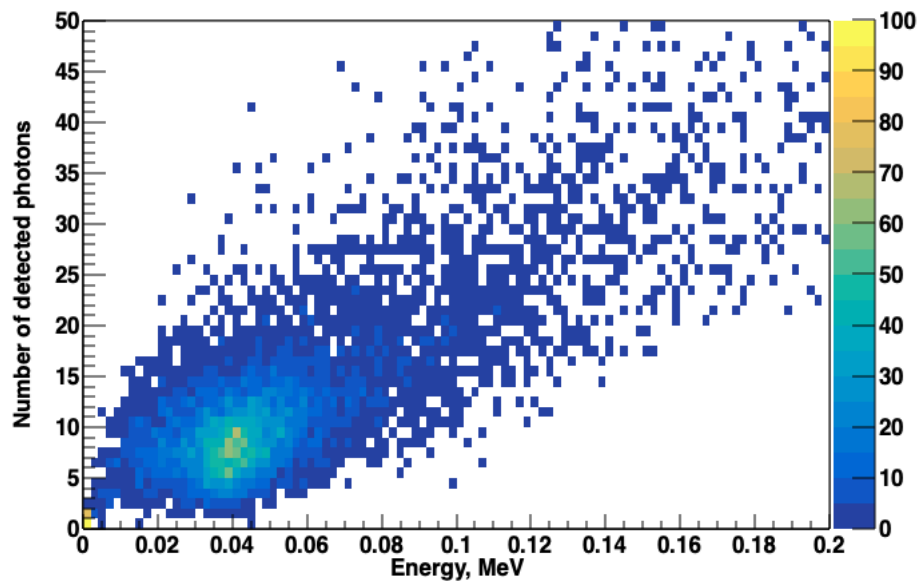
Figure 3.13: The number of photons generated which reach the end of the fiber as a function of the deposited energy.

3.5.3 Fiber Probe Analysis

With the understanding of the single fiber properties, different configuration of the fiber has been tested. The configuration was set parallel to the initial idea, that is to optimise the number of fibers for maximum energy deposition, while at the same time minimising the fiber diameter, which is a requirement of this application. Therefore, the simulation was done for five fibers that make the total diameter of the detector to be effectively about 0.88 mm which is a reasonable size for such intravenous beta probe. 10000 events of monoenergetic positron of 633 keV energy to mimic the maximum energy of ^{18}F placed on the center of the long edge of the fiber firing towards -Y axis direction.
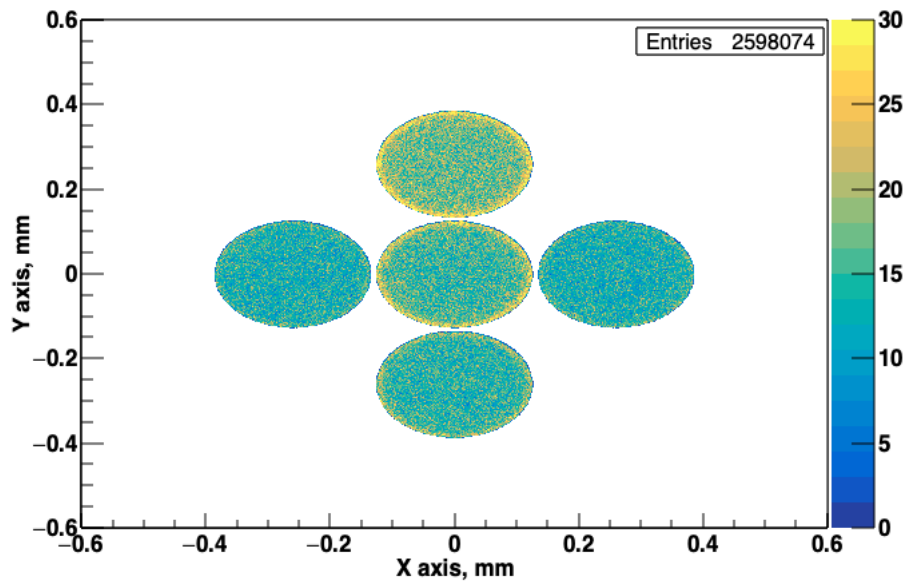
Figure 3.14: Photons output distribution when positron of energy 633 keV crossed the fibers at y-direction.
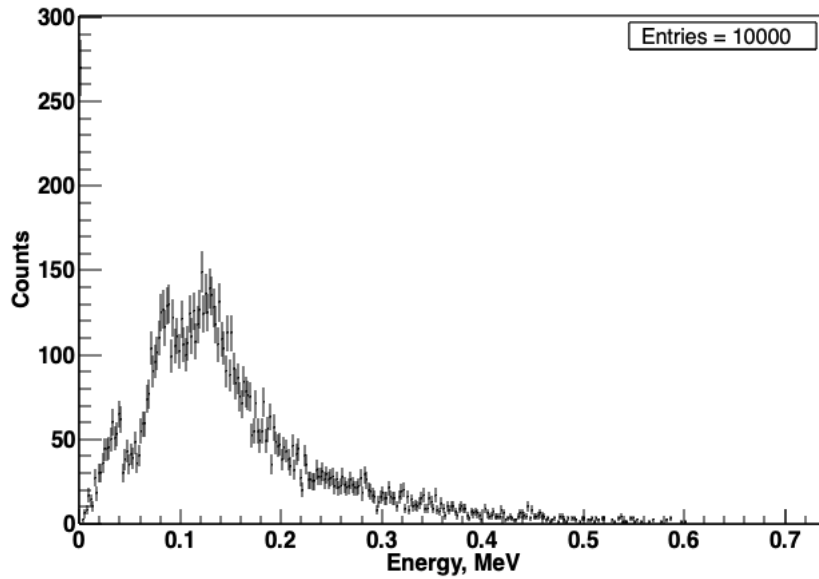
Figure 3.15: Energy spectrum of positron particle of energy 633 keV in fiber probe.

Figure 3.14 shows the photon output at the fiber end when 10000 events crossing the fibers from y-axis direction and figure 3.15 shows the energy spectrum obtained. A more dense distribution was observed on the fibers along the particle path, hence the three peaks observed in figure 3.15. Due to the fiber trapping efficiency being low, most of the photons will escape the fibers and cause crosstalk to adjacent fibers. Furthermore, by increasing the number of fibers, the fiber cross section is increased allowing positron to deposit energy on adjacent fibers. The fibers are thin (250 μm) therefore positrons are likely to penetrate more than one fiber as they cross the fibers.

3.6   Summary

The simulation studies have help to evaluate the performance of the proposed system as well as to optimise the system. The simulation work on microfluidic detector system was to investigate the suitable plastic scintillator thickness and the effect of channel dimensions on the photon collections. The maximum depth of the

positron particle in the plastic scintillator is approximately at 2.4 mm for ^{18}F and approximately 5.0 mm for ^{68}Ga. Reducing the thickness of plastic scintillator to 2 mm may reduce photon collection by approximately 10% for ^{18}F and approximately 40-50% for ^{68}Ga. By changing the micro channel length from short to longer (constant volume), there is an increase of 9% photon detection.

Simulation work of the fiber detector was done to investigate the effect of reflector on the photons propagation in the fiber as well as number of photon generated in the fiber and number of photon detector at the fiber end. The simulation result shows that by adding reflector, the number of photons reaching the end of the fiber is reduced compare to the fiber without reflector. A study was also done to simulate the optical properties of the fiber to obtain the correct trapping efficiency provided by manufacturer. With the accurate optical properties configuration, the fiber was simulated to a bundle of 5 fibers. It was found that, due to the poor trapping efficiency of the fiber, photons may escape to adjacent fibers.

Chapter 4

Scintillation Particle Detection Based on Microfluidic Chip

This chapter reports the work process on designing, fabrication and preliminary test done on the microfluidic detector prototype. In section 4.1.1, microfluidic design criteria and scintillator dimension choices are discussed. The microfluidic detector prototype fabrication methods are discussed in section 4.2. In section 4.3 and section 4.4, methodology used to characterise the prototype and result obtained are presented.

4.1 Introduction

A particle detector based on microfluidic technology was developed. This development combines ideas between knowledge in development of particle detector with microfluidic fabrication techniques. Such device is capable to detect low beta particle activity in microliter volume within high gamma background using plastic scintillator. The device was coupled to silicon photomultiplier that can detect low intensity light photons. It is a simple to manufacture and low cost device that can be use for diagnostic of metabolic processes and can be added to instrumentation for radioisotope production quality control assessment.

This chapter presents the design, fabrications and characterisation studies on the microfluidic detector in terms of efficiency, minimum detectable activity, sensitivity and linearity. Residual activity study was performed to observe molecules absorption on fluidic channel material.

4.1.1 Microfluidic Detector Design

Based on the findings in the previous chapter, the prototype were designed to have single straight channel with cross section dimension on the order of 500 μm. Fabrication of a thinner micro channel is difficult because the PDMS layers tend to bond in to the channel wall, that will caused blocking of the fluid flow in the channel. Although based on earlier attempt, the serpentine curve (S-shaped curve) channel would be a better choice, it was evident that fluid will likely to be trapped in the 'dead zone'- where fluid velocity is small or none and usually happen in channel corners - in the fluidic channel. The channel is then sealed with a thin layer of monomer that also separates the channel from the plastic scintillator by approximately 10 μm.

There are a few essential criterion that are being considered in designing the detector. To get sufficient amount of light, the radioactive fluid should be

present in the scintillator window for a sufficient amount of time. Therefore, the channel should be long enough to allow more particles to interact with the scintillator. In addition, the channel must be tightly sealed to ensure no radioactive contamination within the detector, which can affect subsequent measurements. Ideally, radioactive fluid should be in direct contact with scintillator, this is to eliminate particles interaction within the barrier. Finally, the surface on the PDMS layer between the scintillator and photo sensor has to be a perfectly smooth to guide light towards the photo sensors.

Several microfluidic fabrication utilising different materials such as Polydimethyl-siloxane (PDMS), perspex and glass were attempted in this research. Finally, PDMS and glass have been chosen for the microfluidic fabrication. PDMS is a silicone-based organic polymer which is optically clear and non reactive to aqueous solvent. Fabrication of microfluidic in PDMS and glass using photolithography method provides faster, more accessible fabrication method and less expensive. Compromise has to be made on the barrier between channel and scintillator by adding a thin layer of PDMS to aid containing fluid in micro channel. Without the thin layer, the channel tends to leak fluid to surroundings. Material such as perspex was undesirable as it is difficult to seal the channel to prevent leakage and microscopic cracks are visible on the channel walls due to the milling process perspex.

In the end, three designs of the microfluidics were proposed for this study using different type of plastic scintillators, with various thicknesses and various micro channel cross section dimensions.

4.2   Fabrication of Microfluidic Detector

The proposed basic microfluidic design is illustrated by the schematic diagram in Figure 4.1. A number of microfluidic chips of different designs were fabricated

in this study. Due to various technical failures such as fluid leaking from fluidic channel, channel blockage and PDMS sealing difficulties, only three microfluidic designs were successfully fabricated for further tests.
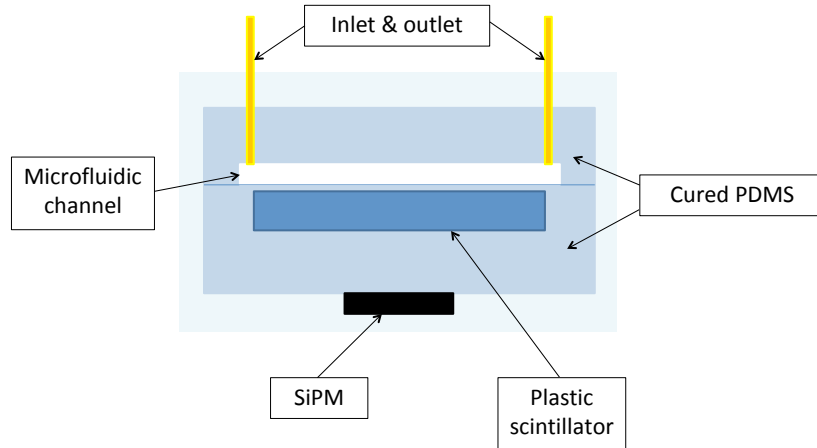
Figure 4.1: Schematic diagram of the cross section of a typical micro fluidic chip and the SiPM detector. In the center of the chip is a microfluidic channel where radioisotope solutions can be loaded.

The first design of microfluidic chip (MC1) consists of 2 pieces of PDMS. A channel of 0.5×0.5 mm^2 cross-section with 10 mm length (2.5 μL) was fabricated on one piece of PDMS using replica-molding technique using a master mould which was milled to the fluidic channel dimensions on top of an Aluminium sheet (Figure 4.2a and 4.2b). The PDMS prepolymer mixture was poured onto the mould. After thermal curing at 60° for 6 hours, the PDMS replica mold was peeled off the master mould. Holes were punched perpendicularly at each end of the channel for the inlet and outlet tube.

Meanwhile, a $6 \times 6 \times 2$ mm^3 plastic scintillator (EJ-212, Eljen Technology) was submerged in PDMS prepolymer mixture and cured in oven for 6 hours at 60° (Figure 4.2c). Alternatively, the PDMS mixture can be cured overnight at room temperature. The PDMS left approximately 10-30 μm of PDMS layer on top of the scintillator interface, and a thicker PDMS on the bottom part. The thin layer
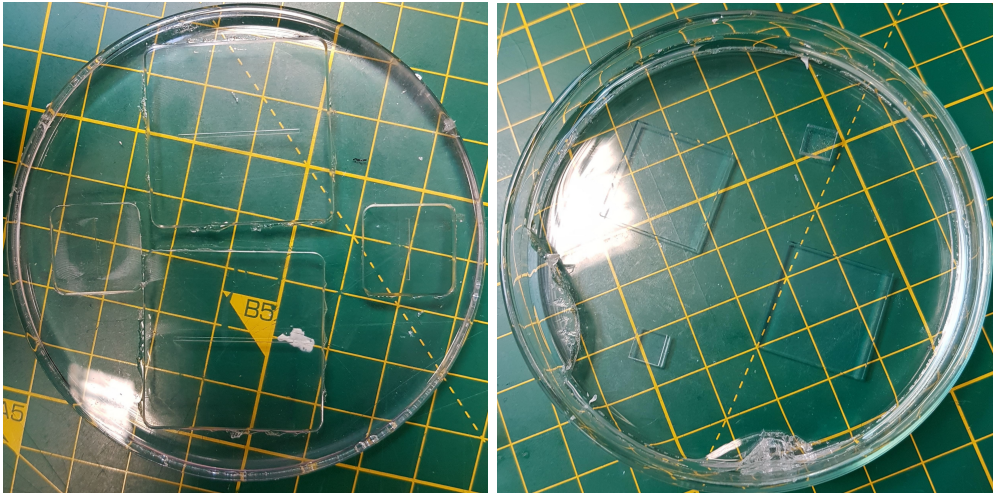
Figure 4.2: (a)Aluminium master mould milled to the dimensions of fluidic channel (b)Impression of fluidic channel on a cured PDMS (c) Plastic scintillator submerged in cured PDMS.

is essential to seal the channel. Using plastic scintillator alone will not help to seal the channel because PDMS-Plastic bond is not strong and can easily detached from the plastic scintillator. After that, these two PDMS pieces were then treated with oxygen plasma to initiate bonding. The treated surfaces were placed onto one another to bond the PDMS pieces together which is essential to sealing the fluidic channel. The PDMS-PDMS assembly facilitates permanent bonding and confines radioisotope in the channel. Photos of this design is shown in Figure 4.3a and 4.3b.

The second microfluidic detector (MC2) design was similar to the first design in terms of material preparations and fabrication process. However, in this design,

the dimensions of fluidic channel and placement of the fluidic channel in the plastic scintillator were different in comparison to MC1. The channel dimension was $25 \times 0.5 \times 0.5$ mm^3 and it was placed diagonally on top of the PDMS-scintillator assembly as shown in Figure 4.3c.
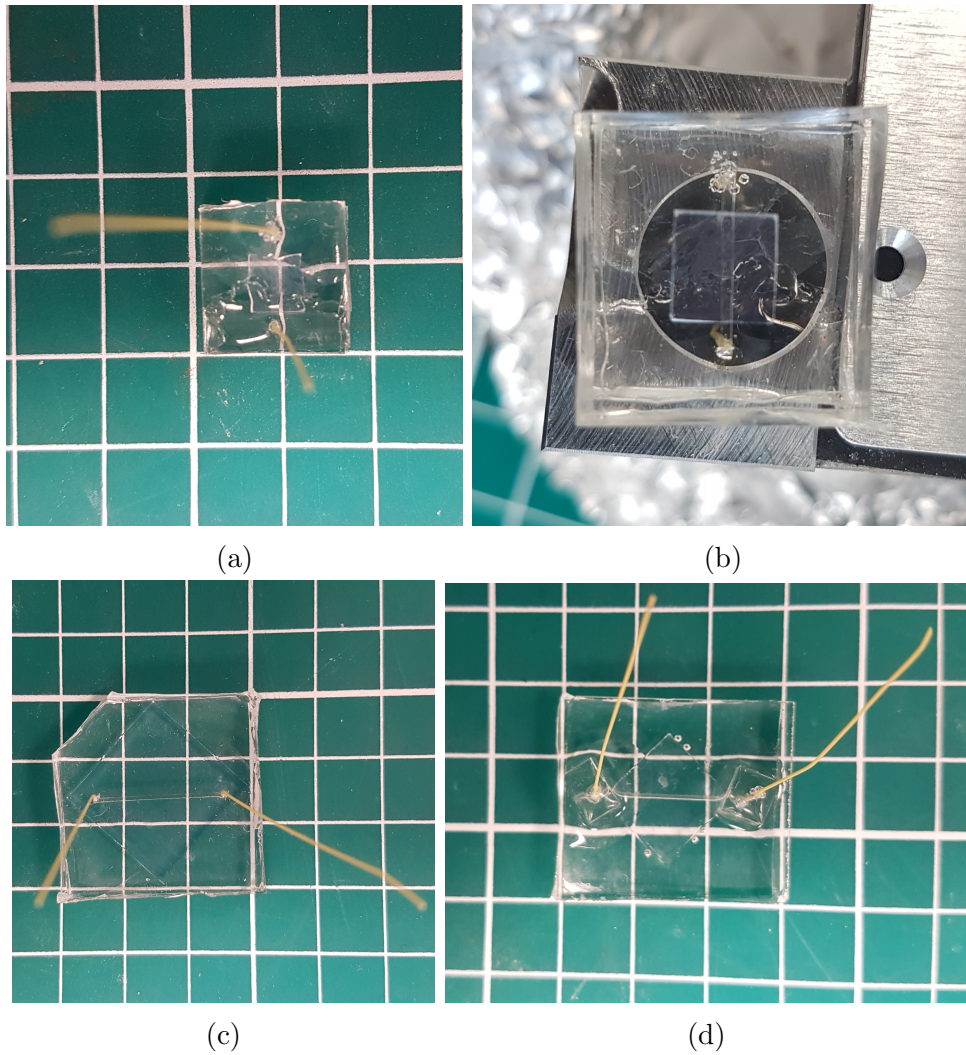
Figure 4.3: Picture of the microfluidic detector (a-b) top and bottom view of MC1 (c) MC2 (d) MC3.

The third design (MC3) was a larger channel with volume capacity of 6.25 μ compared to the previous 2 designs. For this prototype, the channel was milled on top of a glass slide. The channel length is 25 mm with 0.5×0.5 mm^2 cross-section. Glass was chosen because it can permanently bond to PDMS and moreover, there was a report on reaction of F-18 with PDMS that produces volatile compound[64].

This will be discussed further in section 4.4.1. The similar method of fabrication was implemented for the plastic scintillator-PDMS piece. However, the plastic scintillator dimensions used for this microfluidic chip is a $15 \times 15 \times 1$ mm^3 (BC-404, Saint-Gobain).

Finally, inlet and outlet PEEK tubes of 360 μm were attached to the microfluidic chips holes and sealed with PDMS. The tubes must be able to withstand high pressure cause by high velocity fluid flow. Figure 4.3 is showing the finished microfluidic chip for all the different designs.

4.2.1 Photodetectors and Electronics

Nowadays, PMTs are being replaced with silicone photodiode in scintillator detector technology. This photodiode has the advantage that they can be made very small and few millimeter thick. Silicone Photomultiplier (SiPM) is a readout device consisting of multiple micro counters, typically 20-30 μm, in a silicone substrate. It is a very fast response device. Furthermore, it has high gain, which eliminates the need for preamplifier. It operates in a low voltage and low electronics noise. The overall photon detection efficiency of SiPM at around 20-30%. It is ideal to be integrated to microfluidic chip because of its relatively small compare to other similar device with similar function.

Figure 4.4: Microfluidic detector is wrapped with several layers of PTFE to ensure light photons do not escape out from detector.

A single C-Series MicroFC-SMA-60035 SiPM (SensL, Cork, Ireland) was coupled to the first microfluidic. This SiPM model contains 18980 microcells per 6×6 mm^2. The microfluidic-SiPM assembly were wrapped with layers of PTFE tape (Figure 4.4) and Aluminium sheet to prevent light loss as well as to shield it from surrounding light. The SiPM were connected to the MCA527Micro (GBS electronic GmbH). The μMCA was powered over by micro USB connector at 28.5 V bias voltage and 0.01 mA current. It is able to perform digital signal processing and operated in two modes; a) Pulse height analysis and b) Multi-channel Scaling (MCS) mode. The MCS Module is capable of converting the output signal from the SiPM to number of particle detected as a function of time.

4.3   Experimental Setup

Before injection with radioactive fluid, the detector prototype were placed in a light-tight black-box. A pair of tygon tubes was connected to the inlet and outlet tubing from outside of the box. The length of the tubes was kept as short as possible to minimize the dispersion within the tube. The filling in of the radioactive

fluid in the fluidic channel was executed with a syringe controlled manually by hand. The chips were filled with ^{18}F solutions. Later on, the same procedures were repeated for ^{68}Ga solutions but were not done on the same day. This was to allow any residual isotope to fully decay. After every activity measurement was done, the fluidic channel was flushed with water to wash-out all the radiaoactive fluid as much as possible. Residual counts were recorded each time. The experimental setup of the detector prototype is illustrated in Figure 4.5. Prior to each experiment, the prototype was injected with water several times to observe any leaking within the microfluidic chip.
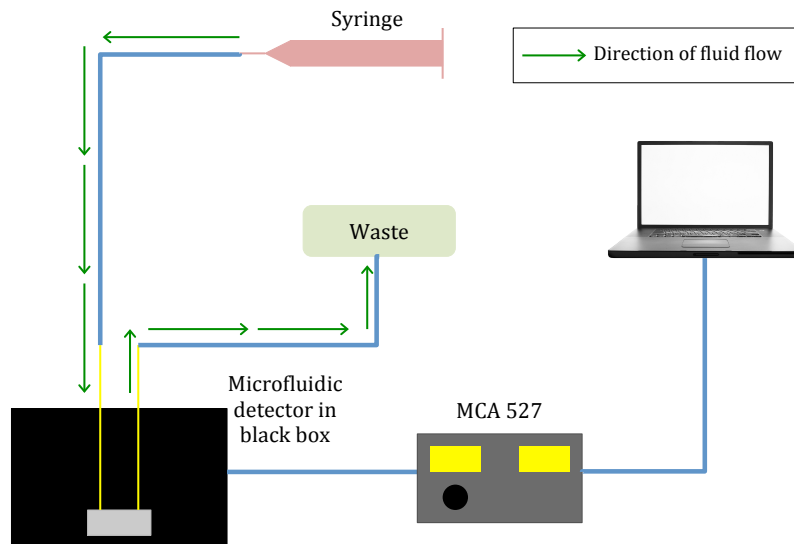
Figure 4.5: Experimental setup of the micfluidic detector. MCA 527 is powered over by micro USB connector and has an integrated power supply for SiPM and for internal preamp.

4.4 Results

The detector characteristics were studied. Firstly, study on the effect of microfluidic material on residual activity after each injection. Subsequently, detector characteristic such as efficiency, sensitivity and linearity were investigated.

4.4.1 Residual Activity Due to Molecules Absorption

Choosing the suitable material to fabricate the microfluidic chip is an important aspect to consider. Various material has been used to cater for the vast application of microfluidic[57]. This study requires material that is optically clear, therefore glass and PDMS are the best choices. Glass is most inert material to solvent or chemical, however, the hardness of glass limits its application for a complicated design. On the other hand, PDMS is easy to fabricate with various integrated components but PDMS tend to absorb small hydrophobic molecules which will limit their application for organic solvent.
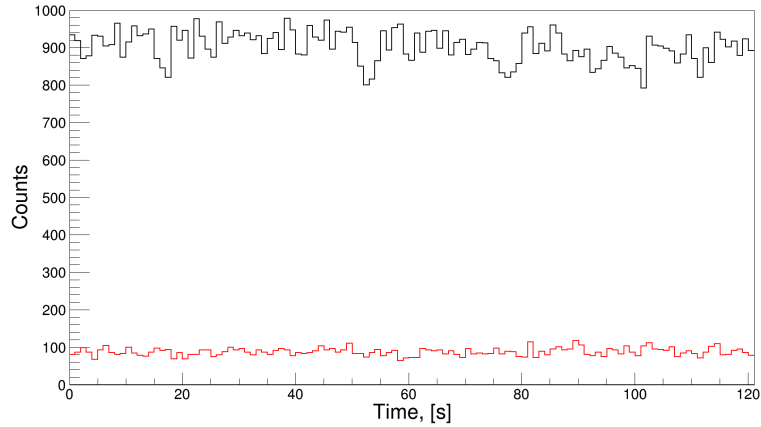
(a)
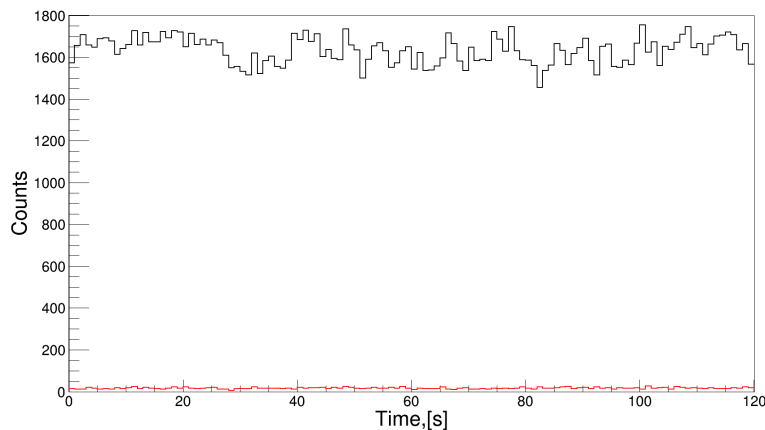
(b)

Figure 4.6: Count measured overtime of ^{18}F in microfluidic detector (black) and residual activity after flushing with 100 μL water (red) (a) PDMS-PDMS microfluidic chip (b) Glass-PDMS microfluidic chip.

A test was done to observe the effect of molecules absorption by PDMS. This was done by investigating the residual activity in fluidic channel after flushing with water. MC2 and MC3 are both injected with 50 μL of 5 kBq/μL and 10 kBq/μL of ^{18}F (respectively) to fill the fluidic channel and count were taken for 120 s. To flush out all the ^{18}F fluid from the channel, 100 μL of water slowly injected into the channel and measurements were taken for 120 s. Figure 4.6 is showing the number of counts recorded for 10 kBq/μL of ^{18}F and residual activity left in channel after flushed by water. Ratio of counts before and after flushing were calculated and compared. PDMS has almost 10 times higher residual activity compare to glass with 9.6$\pm$0.1%. This shows that there was ^{18}F reaction to the PDMS substrate. Elizarov et al. [65], in their study have reported that ^{18}F molecules are reactive to PDMS. There are ways to tackle PDMS permeability such as applying coating on the channel surface or chemically treat the channel surface.

4.4.2 Detection Efficiency

Detection efficiency is defined as the ratio of counting rate recorded over the actual activity in the micro channel[66], assuming there is no counting loss due to dead time. Efficiency varies with energy of incident radiation but independent of the intensity. The efficiency of each radioisotope is different as it depends on the energy loss of the isotope in plastic scintillator. Therefore, the efficiency for every radioisotope needs to be measured.

These measurements were performed for both ^{18}F and ^{68}Ga. Each microfluidic detector were filled with approximately 10 kBq/μL of radioactive solutions. The energy spectrum and counting rate were recorded for 180 s but only counts within 120 s were taken for efficiency measurement because some of the measurements were done for 120 s. The pulse height spectrum and counting rate were recorded for efficiency measurement as illustrated in figure 4.7. Thresholds were set to be just above the electronic noise and were fixed for the same microfluidic detector.

Above the threshold, background noise was within 3 Hz.
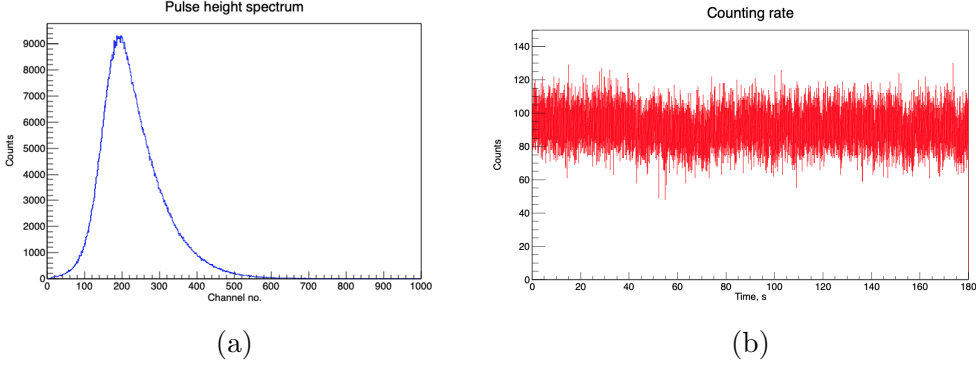
Figure 4.7: ^{18}F solution filled in the micro channel and counted for 180 s (a) pulse height spectrum of ^{18}F (b) counts recorded as a function of time.

Detection efficiency of the detectors was calculated using this expression4.1,

$$\eta(\%) = \frac{m}{CV} \qquad (4.1)$$

where m is the average measured count rate, corrected for decay, C is the solution concentration and V is the device detection volume. Data were gathered in histograms, in order to obtain the count integral of the detector output signal. For all three detectors, the detection volumes were taken as the volume at the fluidic channel of the SiPM which are 2.5 μL for MC1 and 6.25 μL for both MC2 and MC3. It was assumed that only the positrons energy was deposited in the plastic scintillator, which determined the efficiency.

Table 4.1: Absolute efficiency of MC1, MC2, and MC3 for ^{18}F and ^{68}Ga.

Detector	Absolute efficiency,(%) for ^{18}F	Absolute efficiency,(%) for ^{68}Ga
MC1	unavailable	18.3
MC2	7.6	33.9
MC3	2.5	6.6

The absolute efficiencies for different isotope and microfluidic chip were calculated using Equation 4.1 and are summarised in Table 4.1. The efficiency of MC2

is higher compare to MC3 for ^{18}F and ^{68}Ga. This was expected as the thickness of both plastic scintillators are different, hence lesser positrons stopped in 1mm BC404 plastic scintillator. Unfortunately, absolute efficiency of MC1 for ^{18}F was unavailable due to the channel leakage on the start of the ^{18}F experiment.

4.4.3   Minimum Detectable Activity

The sensitivity of the microfluidic chip simply refers to the lowest and the highest detectable limit that can be measured reliably by the system. The minimum sensitivity is the function of the background count. This was introduced by Currie[41] by this function known as Currie equation,

$$N_D = 4.653\sigma_{N_B} + 2.706 \tag{4.2}$$

where N_B is the number of count detected and σ_{N_B} is the background standard deviation. To be able to determine the minimum and maximum detectable activity, absolute efficiency η must be taken into account. Therefore, the above Equation 4.2 can be expanded into two equations 4.3 and 4.4 [31] as follows,

$$A_{min} = \frac{2.706 + 4.653 \times \sqrt{b}}{\eta \times V} \tag{4.3}$$

$$A_{max} = \frac{N_{max}}{\eta \times V} \tag{4.4}$$

where b is the background count rate obtained without radioactivity and N_{max} is the maximum counting rate allowed by the Mini MCA 527 which is 14bits.

In this experiment, performances of the microfluidic chip at the minimum detectability were assessed. Approximately 10 kBq/μL of isotope was injected in the

Table 4.2: Minimum detectable activity for ^{18}F.

Detector	Min activity(A_{min}),Bq/μL
MC1	NA
MC2	13.2
MC3	40.4

Table 4.3: Minimum detectable activity for ^{68}Ga.

Detector	Min activity(A_{min}),Bq/μL
MC1	19.7
MC2	40.4
MC3	13.0

channel and measurements were taken for 120 s. The counts of each measurements were used to calculate the minimum detectable activity using Equation 4.3. The A_{min} values for ^{18}F and ^{68}Ga were reported in Table 4.2 and 4.3.

4.4.4 Detector Linearity and Sensitivity

Linearity response study is an important characteristic because it helps to define the range of detector measurement, which gives out accurate results. The microfluidic detector response linearity in relation to the variation of the sources activities was the decay method, which consists of measuring the activity of a radiotracer along time, allowing for the plotting of the total count versus time curve and the comparison of the experimental activity values with the expected theoretical values for the source at the different measurement times. Assessments on the linearity of the microfluidic detector are presented in this section. Due to leakage of fluidic channel of MC1 and MC2, the tests were done only for MC3. The linearity test was done by measuring the decay of ^{18}F and ^{68}Ga in MC3 fluidic channel over the course of several hours. About 20 kBq/μL of ^{18}F was filled in the detector channel and decay measurement was taken for 170 minutes. Similarly, detector channel

was filled with 10 kBq/μL ^{68}Ga and left for 279 minutes to decay. This was done on a different day from ^{18}F to ensure no ^{18}F residual activity affecting the ^{68}Ga measurement. Figure 4.8 and 4.9 shows the ^{18}F decayed signal over time.
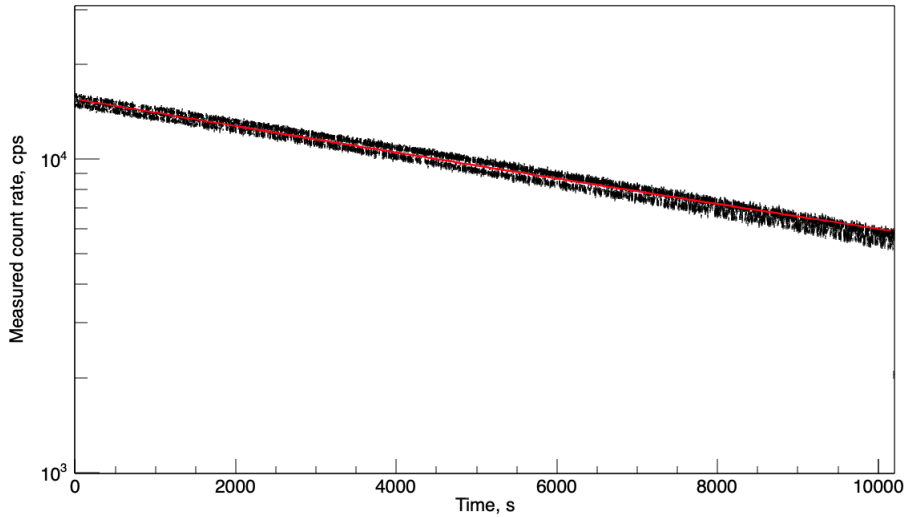
Figure 4.8: Measured net counts per second after background subtraction plotted as a function of time. The theoretical decay of ^{18}F is shown as a red line and measured counts are in black.

The background corrected signal data were fitted to mono-exponential to obtain the decay constant, λ and the measured half-life, $T_{1/2}$ was calculated. The half-life for the ^{18}F signal was 109.0$\pm$0.1 min. which is consistent with the expected value for ^{18}F, 109.8 min. However, for ^{68}Ga , the calculated half life was 76.0$\pm$0.1 min which is 8.3 min more than expected. As can be seen in Figure 4.9, at higher activity, the detector system detect less count than expected. At this point, the dead time is too high therefore the detector was unable to process all counts. This might be contributed by the fact that the size of the SiPM is considerably small, therefore affecting the dynamic range.

From the same data, sensitivity of the microfluidic detector can be calculated for ^{18}F and ^{68}Ga. Sensitivity was derived by calculating the ratio of the measured count rate to the activity of ^{18}F and ^{68}Ga in the channel. Figure 4.10 and 4.11 show the measured data against the actual activity for ^{18}F and ^{68}Ga, respectively.
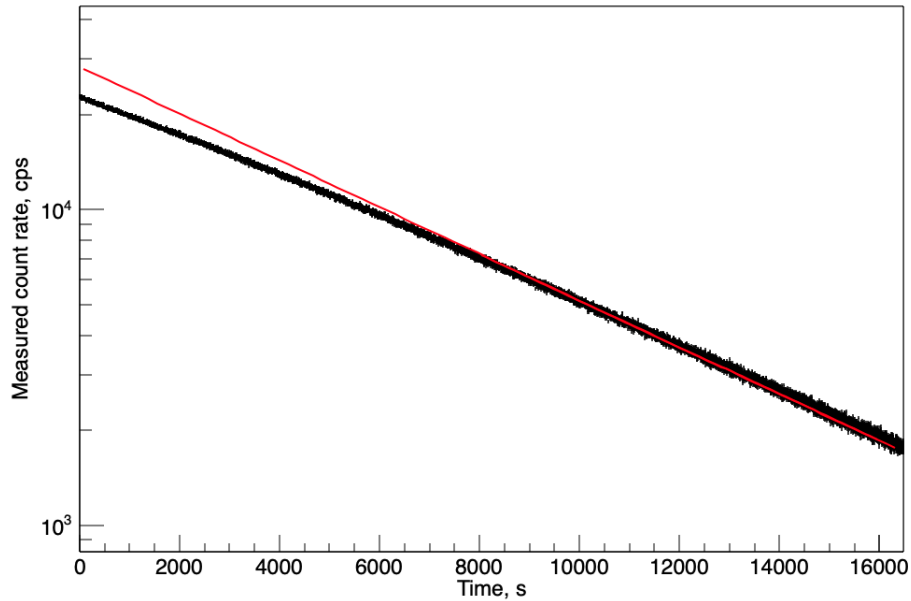
Figure 4.9: Measured net counts per second after background subtraction plotted as a function of time. The theoretical decay of ^{68}Ga is shown as a red line and measured counts are in blue.

These data were fitted using a linear least square for the count rate between 9000 to 14000 cps for ^{18}F and 2000 to 8000 cps for ^{68}Ga. Sensitivity of the detector for ^{18}F is 0.8% and 2.9% for ^{68}Ga. Sensitivity of ^{18}F is smaller than ^{68}Ga this is due to ^{18}F positron energy (E_{avg}=249.8 keV) being lower than ^{68}Ga(E_{avg}=836 keV). It is because a larger fraction of the particles do not reach the detector or produce a signal below the noise threshold. The fit was extended to the maximum count rate to determine the linearity of the detector response. ^{18}F is linear up to 11000 cps while the linearity of ^{68}Ga is only up to 8000 cps. Figure 4.10 appear skewed due to high which we suspect caused by applied setting.
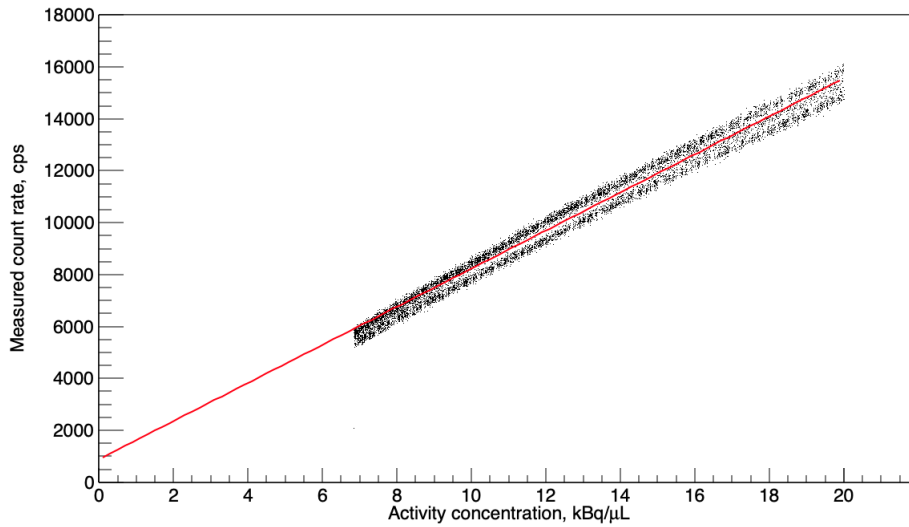
Figure 4.10: Measured of net counts rate versus activity of ^{18}F is shown as black and linear fit for data between 9000 to 19000 in red.
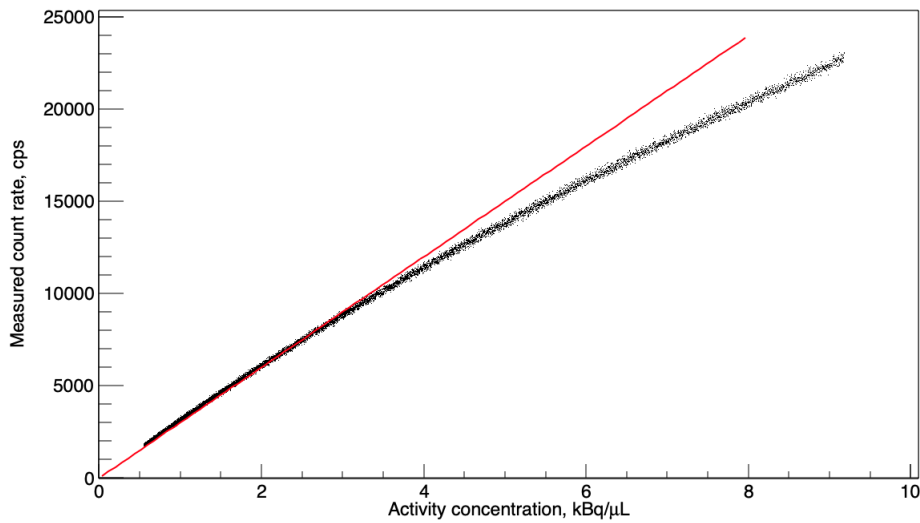
Figure 4.11: Measured of net counts rate versus activity of ^{68}Ga is shown as black and linear fit for data between 2000 to 10000 in red.

4.5   Summary

The experiments has successfully demonstrated the working principle of the microfluidic detector. Standard microfluidic fabrication processes have enable integration of plastic scintillator with microfluidic chip technology. The fluidic chan-

nels with a capacity of 6.5 μL and 2.5 μL were fabricated using the combination of PDMS-PDMS and glass-PDMS. The residual activity left in the channel was highly affected by the type of material used. About 10% higher activity observed in the PDMS-PDMS fluidic channel. The detection efficiency of the microfluidic detectors ranges from 6.6-33.9% for ^{68}Ga and 2.5-7.6% for ^{18}F. The minimum detectable activity varies between 13.0 Bq/μL and 40.4 Bq/μL for ^{18}F and for ^{68}Ga respectively. Overall, the microfluidic detectors are linear up to 10000 cps.

The results obtained show promising future for the development of the microfluidic detector. However, this study is at a very early stage of the development, therefore it requires further assessments using different material and channel configuration and measurement delay correction or dispersion correction, and eventually progressing from a prototype to an actual detector.

Chapter 5

Scintillating Fiber beta Detectors

This chapter presents the design, fabrication and characterisation of the beta probe prototype. The plastic scintillating fiber performance evaluation is discussed in section 5.2.1. In section 5.2.5, assessments of suitable photodetector for plastic scintillator is being discussed. The experiments performed with the beta probe prototype are reported in section 5.3.

5.1 Introduction

The design of the fiber beta probe was based on the need of high sensitivity to positron and decrease sensitivity to background photons. The design also requires the probe to be small and compact to allow it to be inserted to blood vessel. The probe configuration basically consists of scintillating fibres coupled to a SiPM. This reduced volume, low Z and low density scintillator provides a solution to decrease the gamma sensitivity. Furthermore, the beta probe produces low dark count rate due to the fast response of plastic fiber scintillator and the fast response of the SiPM. The basic properties of the plastic scintillator fibers were investigated in the laboratory. Selections of state of the art photodetectors coupled to the plastic scintillating fibers were studied to investigate the signal-noise ratio. Based on the result obtained, has led to the fabrication of the beta probe prototype. Further tests were done to characterise the detector concept such as the light output, decay time measurement linearity and sensitivity.

5.2 Plastic Scintillating Fiber

The plastic scintillating fiber used in this study is a single cladding BCF-10 polystyrene based (Saint Gobain)[53] with 250 μm diameter. The thickness of the cladding is at about 3% of the core thickness. The fiber attenuation length is 2.2 m and it produces ~8000 photon/MeV.

5.2.1 Preliminary Studies

The initial investigations have been carried out in the laboratory to evaluate the properties of the scintillating fibers. For this investigation, the fiber was used to study the light production and its propagation in the fiber. Different photodetectors were also tested with the scintillating fibers to assist on determining the best

photodetector for the prototype.

5.2.2 Fiber Preparations

Five bundles of fiber, each containing 1, 5, 10, 20, 40 and 80 fibers were assembled to obtain outer diameter ranging from 0.5 mm to 2.3 mm. Both ends of the fibers were cut off flat to a near-polished condition. Each bundle was hold tightly together using 3-4 layers of PTFE tape. To ensure no background light being detected by the fiber front end, the front end surface was wrapped with PTFE tape while the opposite end surface was left exposed to the background lights. The fiber component is illustrated as in Figure 5.1.
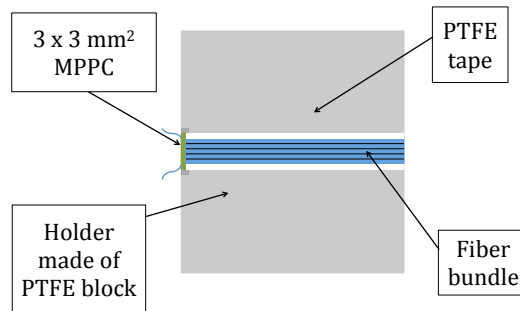
Figure 5.1: Schematic diagram showing the scintillating fiber of 20 mm length in bundles (1, 5, 10, 20, 40 and 80) inserted in PTFE holder coupled to 3×3 mm^2 MPPC S13360-3025PE by Hammamatsu.

The fiber bundles were tested with the same photodetector, namely the 3×3 mm^2 MPPC S13360-3025PE by Hamamatsu. Anode voltage pulses were amplified using a NIM Ortec 527 shaping amplifier prior to pulse height analysis by Multi Channel Analyzer(kromek) Model K102.
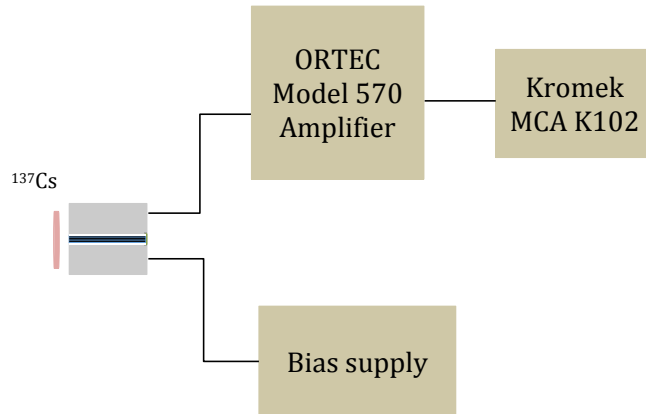
Figure 5.2: Experimental setup for the fiber bundle coupled to Hamamatsu 3×3 mm^2 MPPC S13360-3025PE ($\sim$68 V). ^{137}Cs was placed head-on to the fiber front end. Signal obtained were processed by ORTEC 570 shaping amplifier and Kromek K102 MCA.
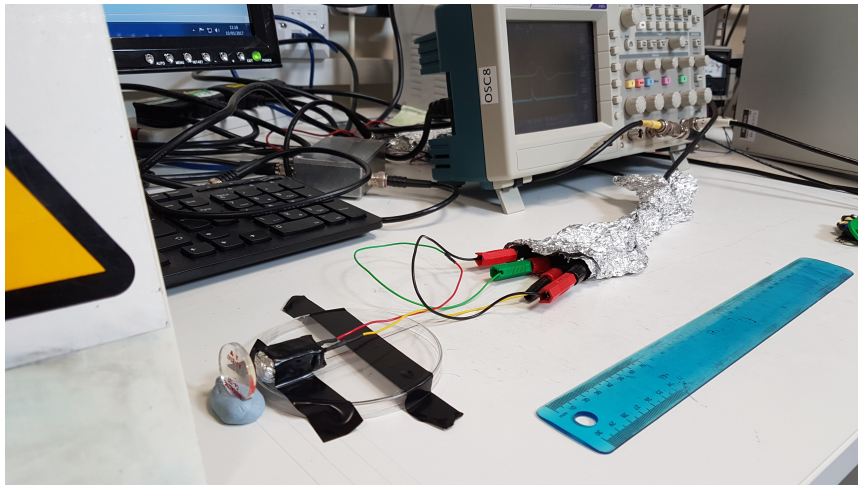
Figure 5.3: The detector system setup for the preliminary studies done in University of York Nuclear Application laboratory. The detector assembly was wrapped tightly to ensure light tightness of the system.

5.2.3 Photon Yield

Since the scintillation photons carry the count rate information, it is crucial for scintillation detector to maximise the photon throughput to the photodetector. One identified challenge was the low number of photons produced when beta par-

ticle transverse a rather thin scintillating fiber. From the simulation result in chapter 3, it is expected at 40 keV, only about 8 photons reach at one end of the fiber. This can be a challenging configuration, especially when fiber coupled to SiPM whose single count rate can reach hundred thousand per second. This particular study was performed to investigate the measured photon yield at fiber end.

Experimental Setup

Since there was no known β source available, a ^{137}Cs point source was placed at a distance from the fiber (Figure 5.2 and 5.3) and the pulse height spectrum were collected using multichannel analyser(MCA). Figure 5.4 presents pulse height comparison for different fiber configurations at different distance from source ^{137}Cs. Photon yield as a function of number of fiber was studied for 3 different source-to-fiber distances. The bundle fiber used were 1, 5, 10, 20 and 40 and measurements were taken for 20 minutes. Threshold was set at 85 mV to reduced dark count rate to 6.5 Hz. The photon counts at 1 cm is shown in Figure 5.5.

Results

Figure 5.5 shows the total count of gamma events detected at the fiber end. As can be seen clearly in this figure, the number of count increase linearly as the number of fiber increases. After 20 minutes measurements, about 600 counts were detected by 1 fiber at 1 cm distance. Photon yield from 5 fibers does show notable amount of detection despite the reduced sensitive area. Although the photon yield for 10, 20 and 40 fiber bundle were better, however, due to the outer diameter that they yield, they are not suitable to be employed as the beta probe prototype. One of the main characteristics to consider during the development of the beta probe is its size. The diameter is the main concern due to the fact that it needs to be small enough to allow it to be inserted in intravenously. Typical diameter of femoral
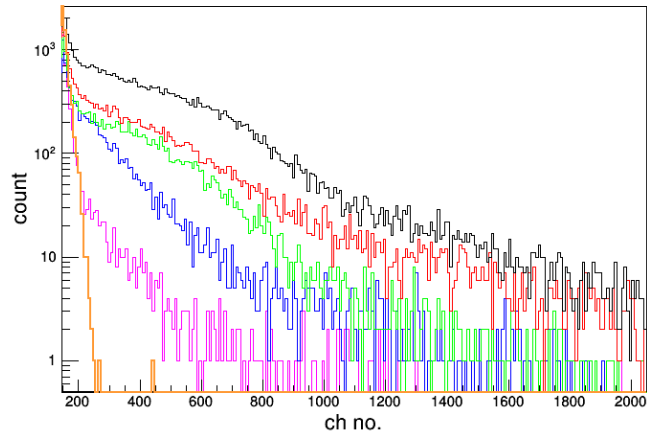
(a)
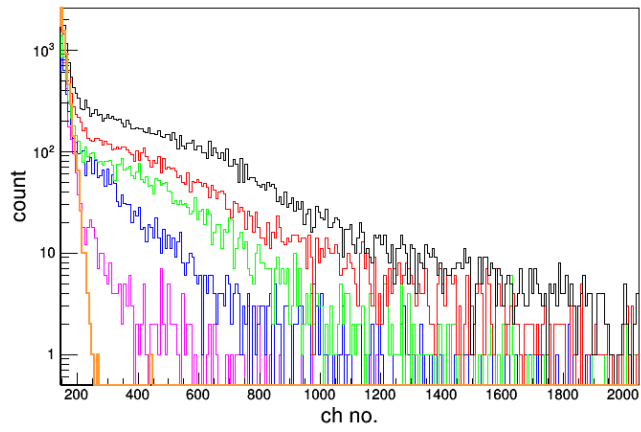
(b)
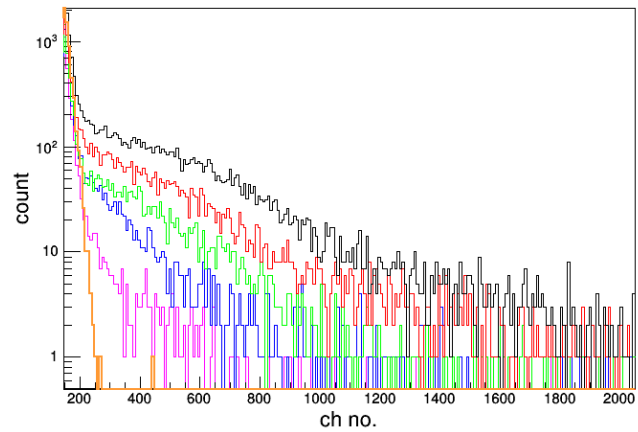
(c)

Figure 5.4: Comparison of the lights detected in for 1(violet), 5(blue), 10(green), 20(red) and 40(black) fiber bundle configuration and dark count rate(orange) at (a)1 cm, (b)2 cm and (c)3 cm distance from a ^{137}Cs source.

arteries in small animals is between 0.6 mm to 0.8 mm.
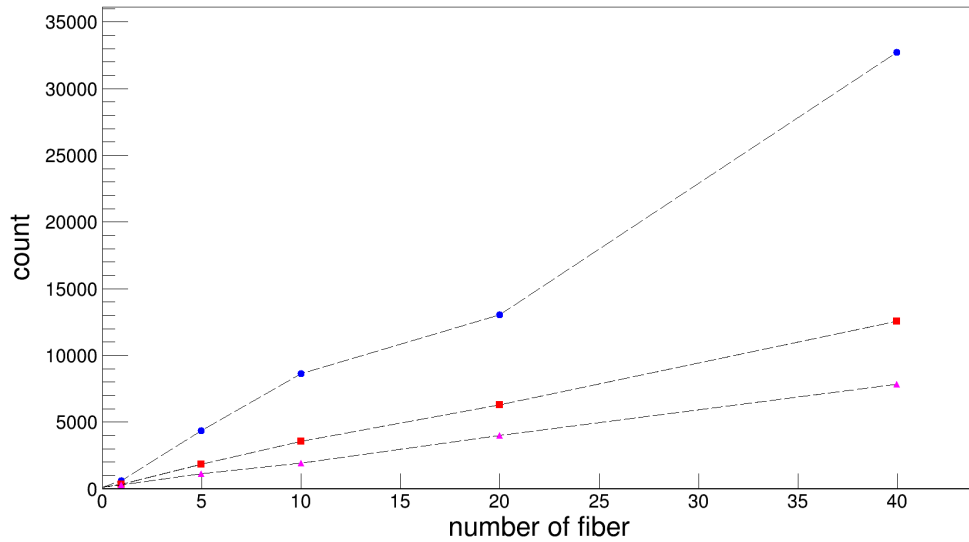
Figure 5.5: Total counts of gamma events as a function of total number of fibers in a bundle at 1 cm(blue), 2 cm(red) and 3 cm(pink) ^{137}Cs source to fiber distance.

5.2.4   Optical Fiber as Light Guide

The use of optical fibers in radiation measurements has gain popularity. The optical fibers are widely used as wavelength shifting fibers to help collect and guide the lights from scintillators to the photodetector. The benefits are a reduced sensitive area of the detector system and reduced external electromagnetic interference[41]. However, the challenge of developing this setup is to transport maximum amount of light produced in the scintillator to the photodetector. This involves optimising the coupling technique and surface treatment of all components. In this section, the study investigates light detection capabilities of the scintillating fibers and SiPM detector system with and without optical fibers

Experimental Setup

To determine whether optical fiber can be used in the setup, measurements were carried out by coupling the 80 scintillating fiber bundle only to 1 inch long optical fiber. The diameter of optical fiber is 1 mm, therefore, 4 optical fibers needed to match the 2 mm diameter of the fiber bundle. The measurement was also repeated for $2 \times 2 \times 16$ mm^3 LSO crystal. LSO is an organic scintillator which has high scintillation yield and fast decay time therefore it will produced better statistics compare to the fiber. Better statistic is needed in order to verify the effect of optical fiber as light guide, since plastic scintillator is less sensitive to gamma.

Result
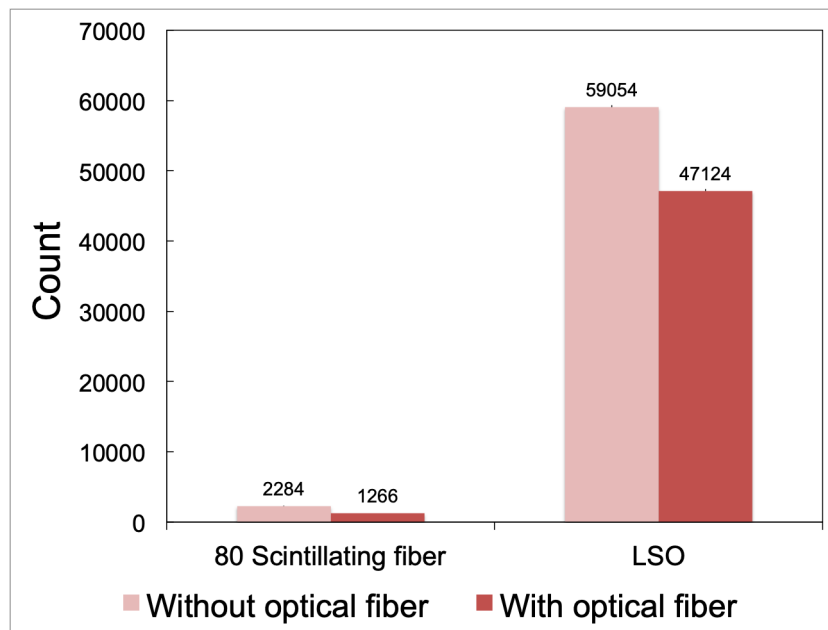
Figure 5.6: Comparison of counts between 80 fiber bundle with and without 1" optical fiber as a light guide. LSO crystal was also tested to verify the setup result as it has higher light yield compare to scintillating fiber.

Interestingly, figure 5.6 clearly shows count difference between fiber scintillator and LSO with and without optical fiber. The result indicates between 20-40 % reduction of light detection when coupled to optical fiber. This experiment shows

that coupling optical fiber to the beta probe prototype reduces light collection.

The flaws of the coupling method between scintillator and optical fiber may have cause the degradation of light detection. Although the overall size matches for both fiber bundle and LSO with optical fiber bundle, light loss can occur at the gaps between adjacent optical fibers. Therefore, the diameter of must accurately match individual scintillating fiber in order to obtained accurate measurement. This can be challenging job especially when dealing with scintillating fiber of sub-millimeter diameter.

5.2.5   Photodetectors

The key aspect of the beta probe is to detect as much light produced by the fiber scintillator as possible. The photodetector has an important role in the detection system in converting the light produced to "readable" electronics signal. Due to the thin geometry, plastic scintillating fiber yield low intensity light. Therefore, it essential to choose a photodetector that able to detect low intensity light and convert it to signal. Among other characteristics of a photodetector that should be considered are the photo detection efficiency (PDE), operational voltage, gain and dark count rates.

Experimental setup

Table 5.1 shows the type of photodetectors coupled to the scintillating fibers to assess their performance with scintillating fiber. An interesting feature by the MPPC TE-Cooled module is that it has a built in temperature control function that able to thermoelectrically cool to -20°. Dark count rate can be minimised by cooling the photodetector to subzero temperature.

Table 5.1: Types of photodetector used to compare the amount of light detected from fibers for the same experimental setup.

Photodetector	Active area, mm^2	Operational voltage, V	PDE %	Dark count rate, kHz	Gain
C-Series SensL SiPM	1×1	28.5	41	30	3×10^6
MPPC S13360-3025PE	3×3	69.5	40	400	7×10^5
MPPC TE-Cooled	1.3×1.3	5	40	2.5	-
μPMT	3×1	4.5 to 5.5	25	0.3 nA	2×10^6

The same experimental setup was prepared for all 4 photodetectors. The front end was exposed to ^{137}Cs source while the opposite end was attached to different photodetectors (Figure 5.2 and 5.3). Similarly, the fiber front end was placed 10, 20 and 30 mm from ^{137}Cs source and the acquisition time was set to 20 minutes for each measurement. Being aware that the proposed probe has to be small and compact, the 80 fiber bundle was not included in the test. Threshold was set just above the electronic noise of each photodetector.

Results

Examples of the comparison of signal pulse height and the noise pulse height for each photodetectors are shown in figure 5.7. Counts recorded for all photodetectors for every fiber bundle are plotted in 5.8

The plot in Figure 5.8 reveals that all the photodetectors performed comparatively equal. Strangely, the MPPC and MPPC TE cooled have similar total count. It would be expected for the MPPC TE cooled to have the highest count as it offers a built in temperature control function, that reduce noise. There is a possibility of lower count caused by the gap between photodetector to the MPPC module window. μPMT came as the best photodetectors from all of them. Despite that, for smaller fiber bundle (1 & 5 fibers), the μPMT and SensL do not show

(a) 1×3 mm^2 μPMT.

(b) 1×1 mm^2 SensL SiPM.

(c) Hamamatsu 1.3×1.3 mm^2 TE-cooled MPPC module.

(d) Hamamatsu 3×3mm^2 MPPC S13360-3025PE.
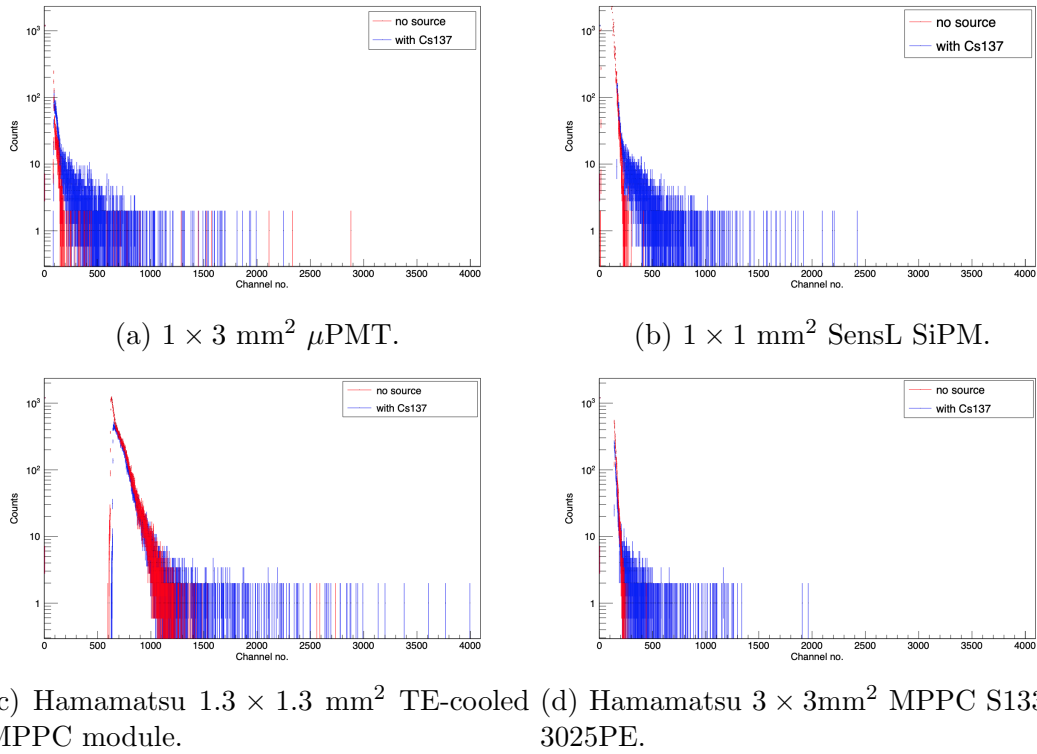
Figure 5.7: Signal pulse height and noise pulse height for each photodetector.

massive differences in total count.
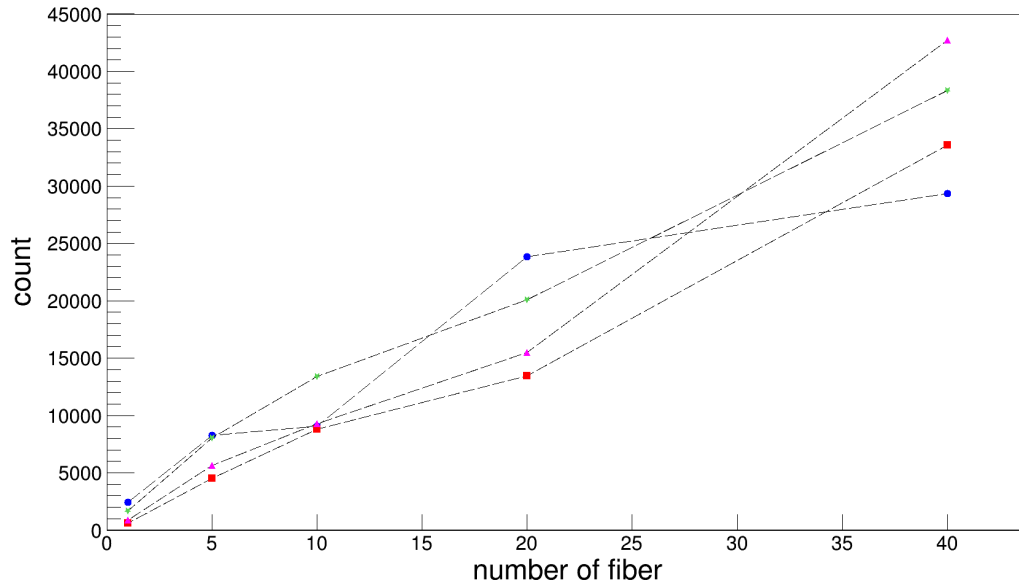
Figure 5.8: Count detected by 1×1 mm^2 SensL SiPM (blue), Hamamatsu 3×3mm^2 MPPC S13360-3025PE(red), Hamamatsu 1.3×1.3 mm^2 TE-cooled MPPC module(pink) and 1×3 mm^2 μPMT(green) for 1, 5, 10, 20 and 40 fiber bundle at 1 cm distance from ^{137}Cs source.

The noise produced in solid state photodetector is caused by the thermal excitation and this can be a limiting factor in detecting low intensity light. Pulse height signal produced by low intensity photon may fall in the noise level. In order to be able to produce readable signal in photodetectors, the signal pulse height should be high enough compared to the noise signal. A signal-to-noise ratio (SNR) analysis was done to investigate signal pulse height generated from photodetector.

By observing figure 5.9 SNR analysis, μPMT gives the highest SNR. It has the highest gain and lowest dark count compare to the others. In contrast, the MPPC TE-cooled has the lowest SNR value. This could again be caused by the air gap between MPPC and glass window that might cause light reflection or absorption to happen multiple times before the light reach the photodetector surface. There is no significant difference of SNR value for MPPC 3×3 mm^2 and 1×1 mm^2 SensL SiPM for less than 20 fibers.
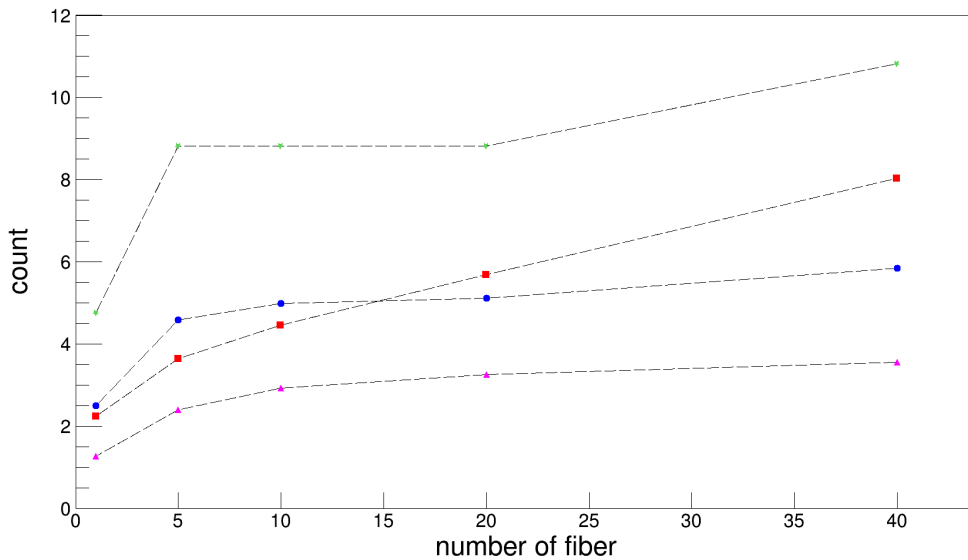
Figure 5.9: Signal-to-noise value for different fiber bundle and by 1×1 mm^2 SensL SiPM (blue), Hamamatsu 3×3mm^2 MPPC S13360-3025PE (red), Hamamatsu 1.3×1.3 mm^2 TE-cooled MPPC module (pink) and 1×3 mm^2 μPMT (green) at 1cm distance from ^{137}Cs source.

Taken together, the findings from the photon yield and photodetector have helped on finalising the beta probe prototype. By observing the physical geometry of the fiber bundle, 1 fiber and 5 fibers are seen fitting the criteria for intravenous

insertion. Photon yield of 1 fiber has seemingly showing good SNR, however, 5 fibers has higher SNR which gives better count statistics. There is no need for optical light guide for this proposed prototype as can be seen from results obtained, coupling to optical fiber of different diameter causes light loss. Likewise, C-series SensL SiPM was chosen for this prototype as it has lower dark count rate and high gain and it is very small and offers compactness compared to the other photodetectors (e.g. MPPC 3×3 mm^2, 1.3×1.3 mm^2 TE-cooled MPPC and μPMT). Based on the results, the 5 fiber bundle and 1×1 mm^2 SensL SiPM were singled out as the baseline for the beta probe due to the higher statistics they provide which is important for accurate characterisation of the prototype.

5.3 Beta Probe Prototype

Based on the previous results and analysis, the beta probe prototype components and configuration was determined. The performance of the prototype was investigated via irradiation with radiotracer solution. Various characteristics such as decay time measurement, sensitivity and linearity have been quantified in PET research center, University of Hull. Accompanying measurement was taken in York laboratory, with standard calibration source.

5.3.1 Fabrication of Beta Probe Prototype

For the prototype, the fibers length in the fiber bundle is 6 cm and are thinly painted with white reflective paint (Figure 5.10b), leaving only the bottom end surface attached to SensL SiPM unpainted. Prior to this, both ends of the fibers were cut off flat to near-polished condition. To prevent surrounding ambient light from entering the sensitive photodetector, a layer of black paint was painted on the fiber component. On completion, the outer diameter measures approximately 1.03 mm.

(a)
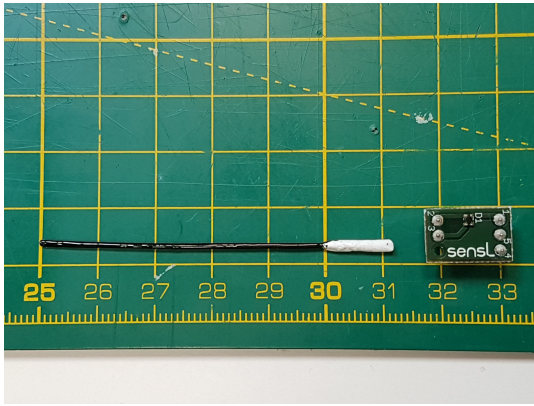
(b)   (c)

Figure 5.10: (a) Bottom end of the fibers are wrapped with PTFE and left exposed to be coupled to SiPM, (b) the length of the fiber is 60 mm, the bottom end was wrapped with PTFE tape. Next to the fiber is the 1×1 mm^2 SensL SiPM on PCB(c) Complete assembly of the fiber-SiPM encased in custom Aluminium case.

The bottom end was wrapped with several layers of PTFE tape until the fiber component perfectly fit inside a 2 mm diameter hole in a custom-made PTFE holder. Caution must be taken during wrapping to prevent from covering the fiber end surface (Figure 5.10a). Silicone optical gel used to facilitate light transport between fiber to SiPM coupling. The fiber-PTFE holder assembly was placed on top of the 1×1 mm^2 SiPM and being hold together using PTFE and black tape. Finally, the assembly was inserted in an aluminium casing, only the fibers protrude out from the casing as illustrated in Figure 5.11 and 5.10c.
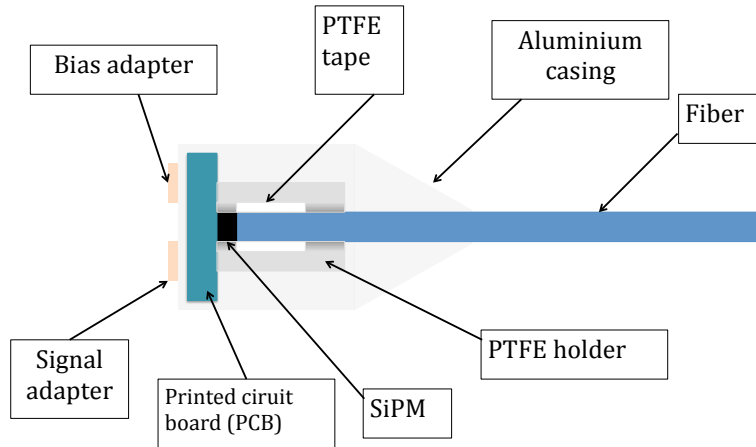
Figure 5.11: Diagram showing the beta probe design. The probe was coated by three layers of white reflective paint and a black paint coating on the outer. The fiber and SiPM is encased in an Aluminium case.

5.3.2 Light Output Measurement

Experimental Setup

The setup for measuring the light output is shown in Figure 5.12. The measurements were taken for electron from ^{90}Sr source and γ from ^{137}Cs source. The sources were placed close to the lateral surface of the probe. The SiPM was operated at +28.5 V. The output signal was connected to a CAEN DT5730 digitizer. All signals were then processed using CAEN CoMPASS DAQ software to get the energy spectrum. An important functionality of the CAEN CoMPASS DAQ is that it controls the firmware on the FPGA such that it can deliver energy, timing, and PSD spectra at the same time. It features a user-friendly interface and allows possibility to save the output in ROOT TTree format.
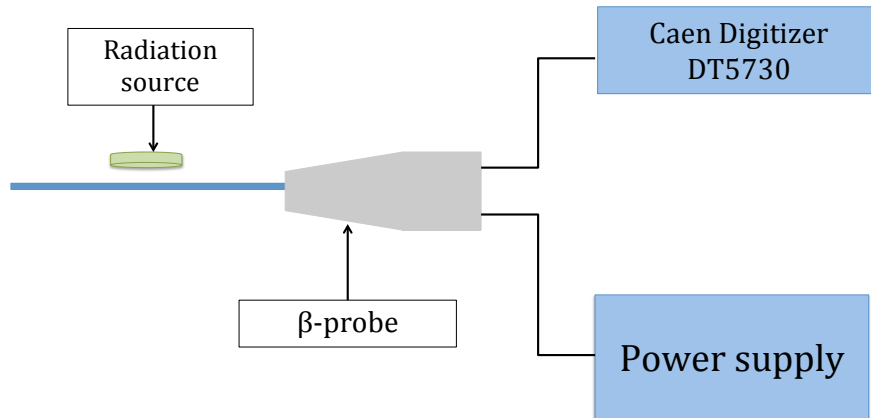
Figure 5.12: Diagram showing the light output experimental setup. Signals were collected and processed using the Caen DT5730 digitizer.
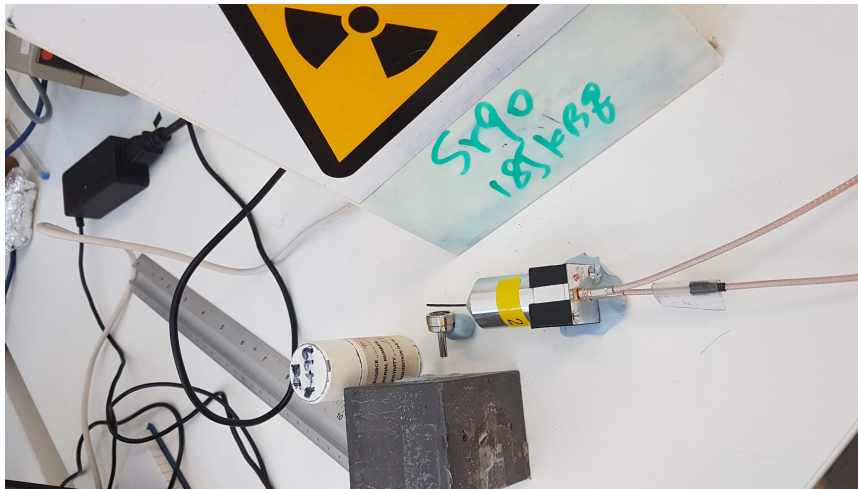
Figure 5.13: Light output experimental setup performed in Nuclear application laboratory to examine the beta probe response to gamma and beta radiation.

Results

Almost exclusively, the interaction of a high energy γ-ray in the plastic scintillator are by Compton scattering due to plastic low density and low atomic number. Evidently, in Figure 5.14, no photopeak can be observed in the ^{137}Cs spectrum. Compton scattering is predominant over the energy range of interest so that it is

difficult to find a photopeak in a spectrum. As can be seen in the ^{90}Sr spectrum, more light output were detected compared to light output from ^{137}Cs. The ratio between beta and gamma counts was calculated as 3.22. This value can easily increase by increasing the threshold value to reduce the dark count rate. ^{90}Sr has a continuous spectrum with mean beta energy of 196 keV and maximum energy of 546 keV. The diameter thickness of the beta probe is not enough to completely stop the high energy beta particles, but only fraction of the energy deposited in the fibers.
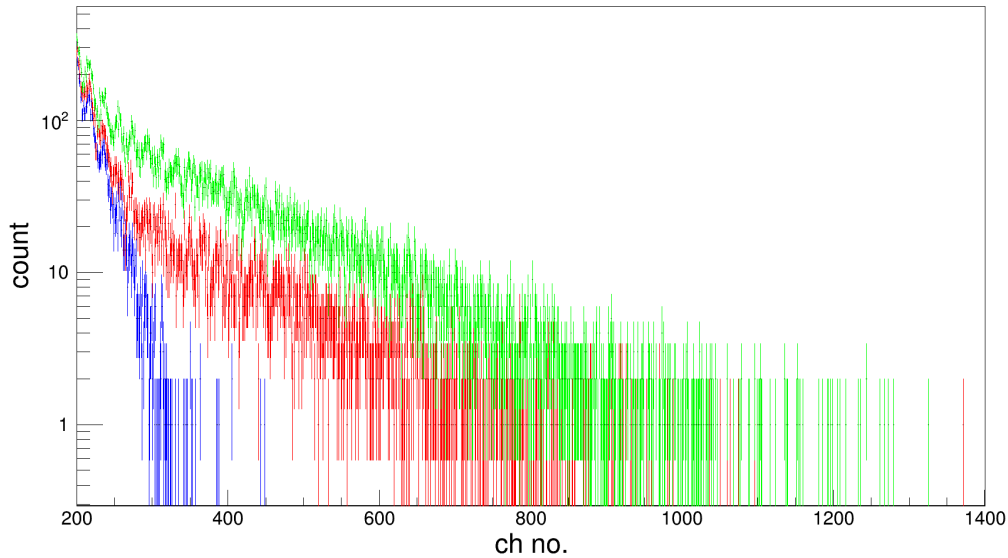
Figure 5.14: Gamma (red) and beta (green) energy spectra from ^{137}Cs and ^{90}Sr, respectively. Background data(blue) was taken with no source.

5.3.3 Decay Time Measurement and Sensitivity

Experimental Setup

The beta probe was tested at PET research centre in the University of Hull. The centre has kindly provided the laboratory space and ^{18}F aqueous solution. To test the decay time and sensitivity, the beta probe was partially submerged in a vial containing 1 ml ^{18}F solution with activity concentration approximately 1 MBq/ml as shown in Figure 5.15. The half-life of ^{18}F is 109 minutes. Therefore, the decay

rate of ^{18}F data were measured for 240 minutes ($\sim$ 2 half lives) while the ^{18}F decay from 1 MBq/mL to 0.21 MBq/mL by counting event as a function of time. Ideally, it will be best to leave the solution to decay up to when the pulse heights fall in the noise. However due to restriction of time and laboratory in the University of Hull, the study time was shorten. Nevertheless, the data acquired were sufficient to test the working condition of the prototype.
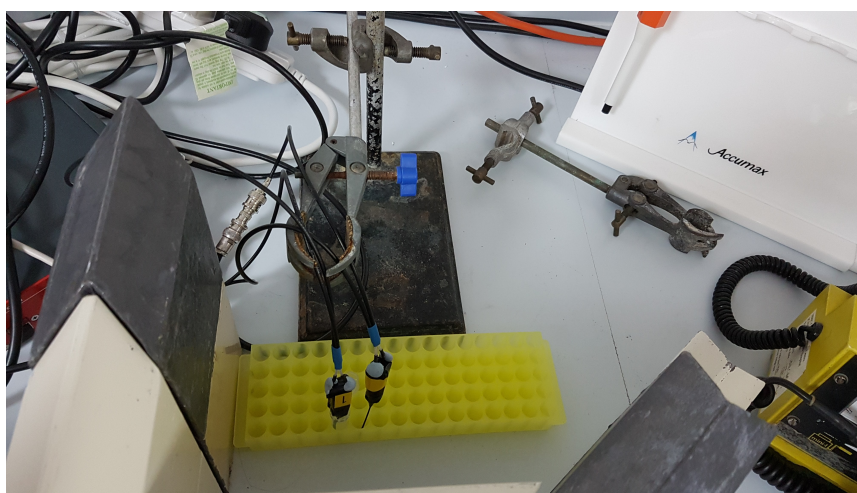
Figure 5.15: Setup of beta probe in PET Research Center at University of Hull. Fiber was submerged in 1 MBq/mL ^{18}F aqueous solution and left to count the decay for 240 minutes.

Results

2D distribution of counts as a function of time and pulse height are shown in figure 5.16 and the pulse height spectrum is shown in figure 5.17. A peak in the spectrum shown in figure 5.16 corresponds to a certain number of photoelectrons. The number of counts reduced following the decay of ^{18}F overtime. One can see single photoelectron distribution peaks in green (Figure 5.16). The dark count rate showing count decays, indicating a large amount of low energy photon being detected fall in the noise level. Hence for this reason, improvement can be made by operating at lower temperature.
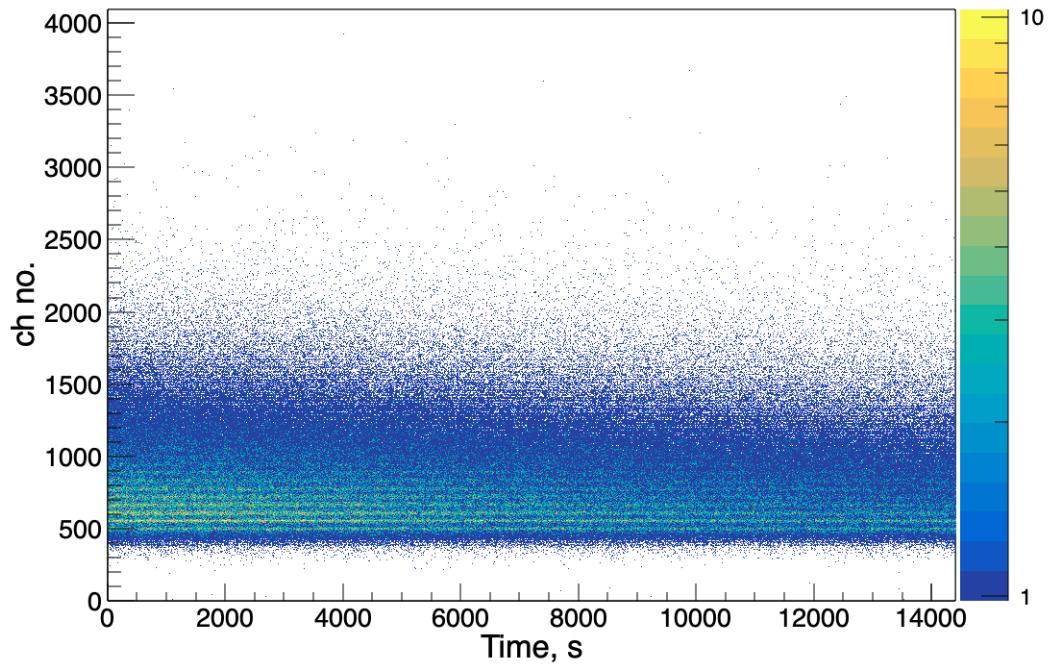
Figure 5.16: 2D Plot of ^{18}F decay over 14400s. The single photon spectra can be clearly seen in the plot. As the ^{18}F decays, count intensity was reduced.
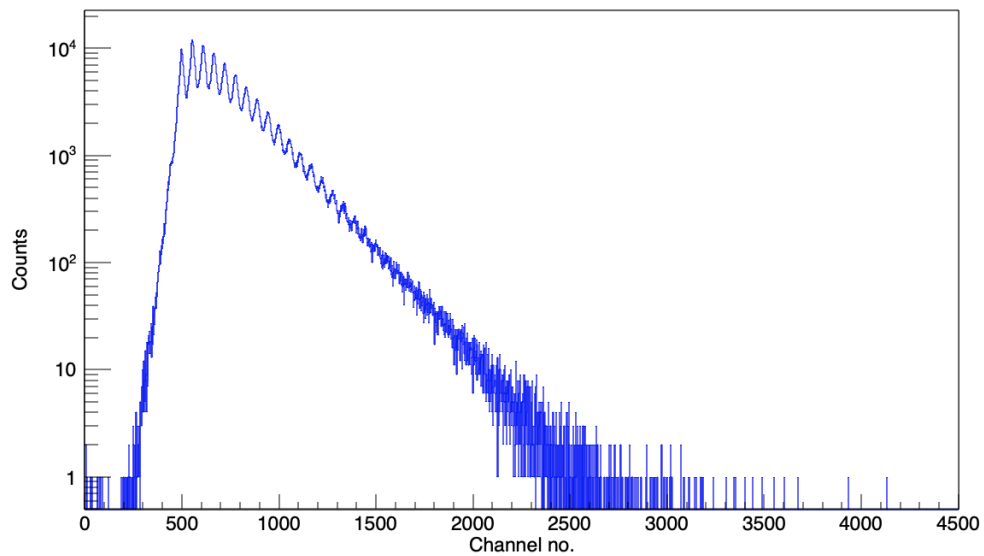
Figure 5.17: Energy spectrum of ^{18}F taken using the beta probe prototype over 14400s. One can see single photon charge spectrum. A peak in the spectrum corresponds to a certain number of photoelectrons.
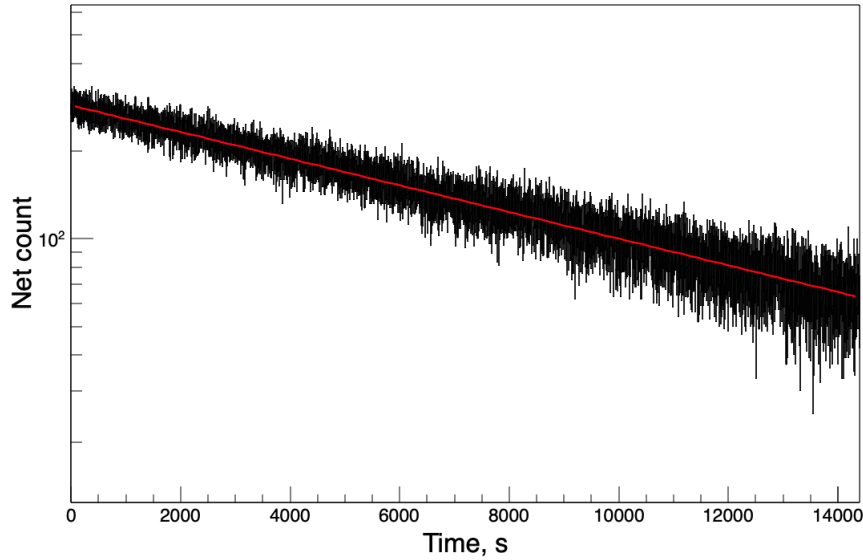
Figure 5.18: Measured net counts plotted as a function of time. The theoretical decay of ^{18}F is shown as a red line above the data points.

Figure 5.18 shows events recorded as a function of time. Decay constant,λ obtained from the exponential fit of the measurement is 1.066 x 10^{-4}/s. As a result, this gives the value of the measured half-life to be approximately 108$\pm$1 min, showing less than 1$\pm$0.1% difference from the actual half-life of ^{18}F which is 109 minutes. Thus, demonstrating the ability of the probe to count ^{18}F beta emission. The 1 min different was suspected to be caused by the limited measurement time, hence, with this method of determining half-life, full time range is preferable[67].

Using the same set of data, absolute sensitivity of the beta probe was obtained from Figure 5.19 and is approximately 289 cps/MBq/ml (0.29 cps/kBq/mL). Thus, this results in only ~3 cps at 10 kBq/mL. Activity concentration in clinical application ranges from 0 to 500 kBq/mL. Therefore, further improvement is needed to adequately measure lower activity.

A typical detector count rate linearity response measurement is shown in Figure 5.20. The acquired data was fitted to first order polynomial, $y = ax + b$. Linearity response of the probe was calculated by comparing the measured to theoretical data as the ^{18}F decay from 1 MBq/mL to 0.21 MBq/ml. The curve

110
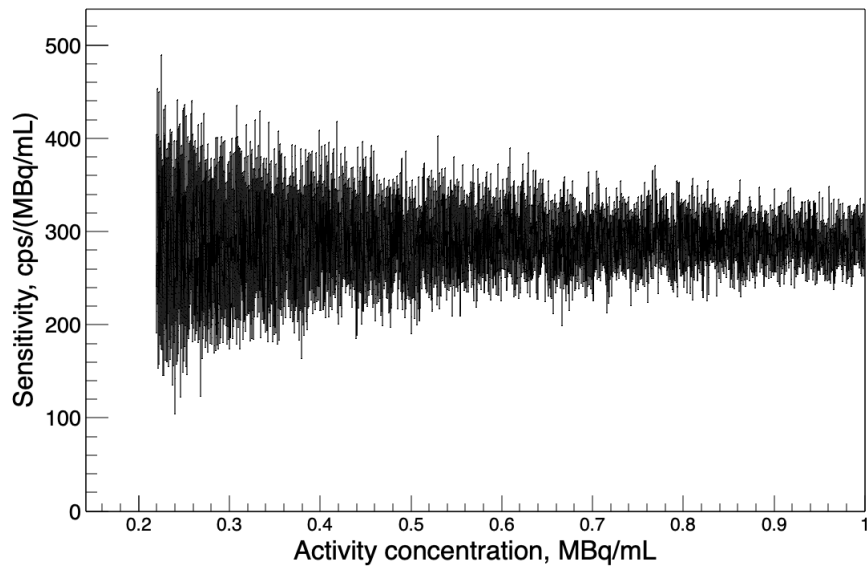
Figure 5.19: Ratio of measured count rate to actual activity of ^{18}F gives the sensitivity of the beta probe.
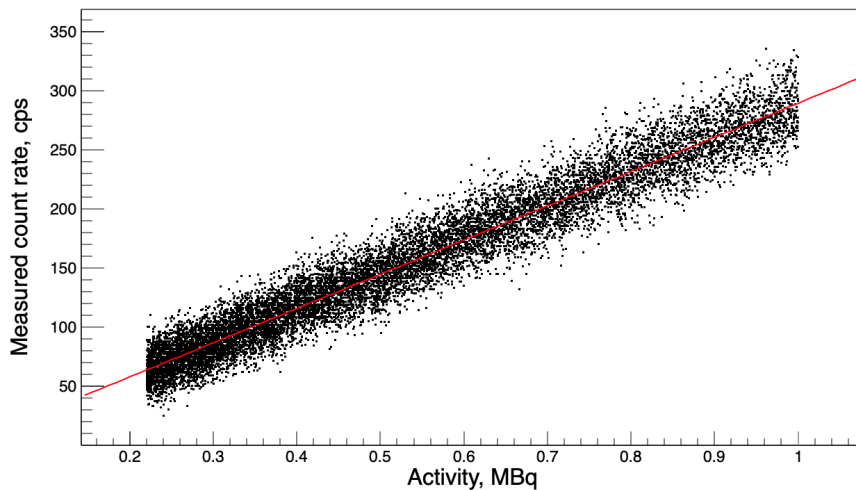
Figure 5.20: Plot of the decay of ^{18}F detected by the beta probe. Linearity of the device is evident from the high agreement of the measured data (black dots) with the theoretical decay (red line).

shows a good agreement between the measured and the actual ^{18}F activity in the vial.

5.4 Summary

This study was motivated by the development of fiber detector with small size photodetector that is intended to be use for intravenous time-activity measurements. Investigations were done on plastic scintillating fiber and designing a portable beta probe detector prototype to optimise the number of light output. A series of studies were done on a fiber bundle to validate the amount of fiber and photodetector suitable for the prototype and application. The beta probe prototype fabricated with the fiber design configuration has shown promising results. The measured decay time of ^{18}F was 108 minutes. The sensitivity of the prototype is 289 cps/MBq/ml. Over the measured activity, the prototype linearity is in good agreement to the actual activity.

The initial feasibility studies have shown the potential of the beta prototype to be blood radiotracer detector. Further improvement and assessments are needed in order to progress from a prototype to an actual detector.

Chapter 6

Conclusion

Two types of beta particle detector based on plastic scintillator were developed and studied. The first detector developed, aimed to operate at low detection volume based on the well established microfluidic technology. The second detector is a beta probe based on the plastic scintillator fiber technology and SiPM that capable of detecting low light intensity.

Prior to fabrication, GEANT4 simulation was done to evaluate the characteristic of the proposed detector systems. The maximum depth of the positron particle in the plastic scintillator is approximately at 2.4 mm for ^{18}F and approximately 5.0 mm for ^{68}Ga. Reducing the thickness of plastic scintillator to 2 mm may reduce photon collection by approximately 10% for for ^{18}F and approximately 40-50% for ^{68}Ga. The comparison between short and longer channel with same radioactive fluid volume indicated longer channel detected more counts. Measurements shows an increase of 9% photon detected on the fiber end.

Meanwhile, GEANT4 simulation for single fiber is showing more lights photons were trapped in fiber of no reflector compare to with reflective white paint. It was evident that majority of the photons were travelling along the fiber border. Therefore, photodetector used must be larger than the fiber cross section. On aver-

age positron deposit 46.6 keV, which allows only 6 photons reach the fiber end and that gives an average of 8 photons per keV reaching the fiber end. Thus show the simulation has successfully replicates the manufacturer trapping efficiency. Further investigations with 5 fiber bundle shows photon crosstalk between adjacent fibers resulting from the poor trapping efficiency.

Based on the simulation findings, three microfluidic detectors labelled as MC1, MC2 and MC3 were successfully made with the combination of material; PDMS and glass. However, the thickness of scintillator used were 2 mm and 1 mm which are only suitable for ^{18}F. Higher ^{18}F residual activity was observed in PDMS-PDMS chip because of adsorption in PDMS fluidic channel surface. The detectors were tested to measure the detection efficiency, minimum detectable activity, linearity and sensitivity. Results shows the detection efficiencies of 7-34% for ^{68}Ga and 3-8% for ^{18}F. The MC3 detector is showing good linearity for ^{18}F, however, for ^{68}Ga, the detection was only linear up to 3 kBq/μL. This is due to saturation on the SiPM caused by the higher energy ^{68}Ga deposited compare to ^{18}F energy.

Preliminary investigation on the behaviour of plastic scintillating fiber and different photodetectors has help on the design and performance optimisation of the beta probe. The beta probe was able to measure ^{18}F activity. The decay time measurement and linearity shows good agreement with the actual decay time of ^{18}F. The sensitivity of the beta probe to ^{18}F is 289 cps/MBq/mL. This can be improved by reducing reflective paint layers on the fiber bundle.

This study presented the first PDMS microfluidic chip integrated to SiPM and the first beta probe utilising full length plastic scintillating fiber detector. This thesis described the proof of principle of these detectors that potentially be use for application in nuclear medicine area and could have been developed further with additional time and resources. In particular, further testing on different material choice that can reduce molecule absorption such as SU-8[68] and the design of fluidic channel that can further increase photon detection. Furthermore, saturation of signal can be improved by selecting SiPM arrays with larger dynamic

Figure 6.1: Cutaneous beta detector made that can be fixed over the wrist to measure activity input function.[11]

range. Meanwhile, the beta probe can further be improved by reducing reflective material thickness.

These detectors have shown the feasibility of plastic scintillator detector as particle detector for medical application. Thus, it is interesting to observe the performance of the detectors in clinical studies. With the advantage of the small size, the detectors can also be developed as a portable wireless monitor system that could measure radiation from the skin of patient. This has been proven possible by a group of researcher [11] (Figure 6.1).

References

[1] Joonyoung Kim, Pilar Herrero, Terry Sharp, Richard Laforest, Douglas J Rowland, Yuan-Chuan Tai, Jason S Lewis, and Michael J Welch. Minimally invasive method of determining blood input function from pet images in rodents. *Journal of Nuclear Medicine*, 47(2):330–336, 2006.

[2] DL Smith, RG Polk, and TG Miller. Measurement of the response of several organic scintillators to electrons, protons and deuterons. *Nuclear Instruments and Methods*, 64(2):157–166, 1968.

[3] James A Sorenson, Michael E Phelps, et al. *Physics in nuclear medicine.* Grune & Stratton New York, 1987.

[4] P Buzhan, B Dolgoshein, A Ilyin, V Kantserov, V Kaplin, A Karakash, A Pleshko, E Popova, S Smirnov, Yu Volkov, et al. The advanced study of silicon photomultiplier. In *Advanced Technology And Particle Physics*, pages 717–728. World Scientific, 2002.

[5] P Annis, A Bay, L Benussi, N Bruski, S Buontempo, C Currat, N D'Ambrosio, R van Dantzig, J Dupraz, A Ereditato, et al. High-resolution tracking using large capillary bundles filled with liquid scintillator. *Nuclear Instruments and Methods in Physics Research Section A: Accelerators, Spectrometers, Detectors and Associated Equipment*, 449(1-2):60–80, 2000.

[6] Qiang Chen, Gang Li, Qing-Hui Jin, Jian-Long Zhao, Qiu-Shi Ren, and Yuan-Sen Xu. A rapid and low-cost procedure for fabrication of glass microfluidic devices. *Journal of Microelectromechanical Systems*, 16(5):1193–1200, 2007.

[7] J Cooper McDonald and George M Whitesides. Poly (dimethylsiloxane) as a material for fabricating microfluidic devices. *Accounts of chemical research*, 35(7):491–499, 2002.

[8] Shagun Gupta, Kritika Ramesh, Suhaib Ahmed, and Vipan Kakkar. Lab-on-chip technology: A review on design trends and future scope in biomedical applications. *Int. J. Bio-Sci. Bio-Technol*, 8:311–322, 2016.

[9] Ming Yu, Qingsong Wang, James E Patterson, and Adam T Woolley. Multilayer polymer microchip capillary array electrophoresis devices with inte-

grated on-chip labeling for high-throughput protein analysis. *Analytical chemistry*, 83(9):3541–3547, 2011.

[10] *ESTAR;Stopping power and Ranges Table for Electrons*, 2018 (accessed December 3, 2018).

[11] A Kriplani, D Schlyer, P Vaska, C Woody, S Stoll, J Logan, S Southekal, S Junnarkar, and JF Pratte. Feasibility studies for extracting an input function for quantitative positron emission tomography using a wrist scanner. In *2007 IEEE Nuclear Science Symposium Conference Record*, volume 6, pages 4051–4053. IEEE, 2007.

[12] Milan Grkovski, Heiko Schöder, Nancy Y Lee, Sean D Carlin, Bradley J Beattie, Nadeem Riaz, Jonathan E Leeman, Joseph A O'Donoghue, and John L Humm. Multiparametric imaging of tumor hypoxia and perfusion with 18f-fluoromisonidazole dynamic pet in head and neck cancer. *Journal of Nuclear Medicine*, 58(7):1072–1080, 2017.

[13] Matthias Brendel, Federico Probst, Anna Jaworska, Felix Overhoff, Viktoria Korzhova, Nathalie L Albert, Roswitha Beck, Simon Lindner, Franz-Josef Gildehaus, Karlheinz Baumann, et al. Glial activation and glucose metabolism in a transgenic amyloid mouse model: a triple-tracer pet study. *Journal of Nuclear Medicine*, 57(6):954–960, 2016.

[14] Jenny Ceccarini, Rebecca Kuepper, Dieter Kemels, Jim van Os, Cécile Henquet, and Koen Van Laere. [18 f] mk-9470 pet measurement of cannabinoid cb 1 receptor availability in chronic cannabis users. *Addiction biology*, 20(2):357–367, 2015.

[15] Ryuichi Harada, Nobuyuki Okamura, Shozo Furumoto, Katsutoshi Furukawa, Aiko Ishiki, Naoki Tomita, Tetsuro Tago, Kotaro Hiraoka, Shoichi Watanuki, Miho Shidahara, et al. 18f-thk5351: a novel pet radiotracer for imaging neurofibrillary pathology in alzheimer disease. *Journal of Nuclear Medicine*, 57(2):208–214, 2016.

[16] Christopher Cawthorne, C Prenant, A Smigova, P Julyan, R Maroy, K Herholz, N Rothwell, and H Boutin. Biodistribution, pharmacokinetics and metabolism of interleukin-1 receptor antagonist (il-1ra) using [18f]-il1ra and pet imaging in rats. *British journal of pharmacology*, 162(3):659–672, 2011.

[17] C Nanni S Fanti. Role of small animal pet for molecular imaging in pre-clinical studies. *Eur J Nucl Med Mol Imaging*, 34:1819–1822, 2007.

[18] Jurgen EM Mourik, Mark Lubberink, Alie Schuitemaker, Nelleke Tolboom, Bart NM van Berckel, Adriaan A Lammertsma, and Ronald Boellaard. Image-derived input functions for pet brain studies. *European journal of nuclear medicine and molecular imaging*, 36(3):463–471, 2009.

[19] D Salas-Gonzalez, JM Górriz, J Ramírez, IA Illán, M López, F Segovia, R Chaves, P Padilla, CG Puntonet, and Alzheimer's Disease Neuroimage Initiative. Feature selection using factor analysis for alzheimer's diagnosis using pet images. *Medical physics*, 37(11):6084–6095, 2010.

[20] Guido Germano, Benjamin C Chen, Sung-Cheng Huang, Sanjiv S Gambhir, Edward J Hoffman, and Michael E Phelps. Use of the abdominal aorta for arterial input function determination in hepatic and renal pet studies. *Journal of nuclear medicine: official publication, Society of Nuclear Medicine*, 33(4):613–620, 1992.

[21] Hao Peng and Craig S Levin. Recent developments in pet instrumentation. *Current pharmaceutical biotechnology*, 11(6):555–571, 2010.

[22] Hsiao-Ming Wu, Carl K Hoh, Yong Choi, Heinrich R Schelbert, Randall A Hawkins, Michael E Phelps, and Sung-Cheng Huang. Factor analysis for extraction of blood time-activity curves in dynamic fdg-pet studies. *Journal of nuclear medicine: official publication, Society of Nuclear Medicine*, 36(9):1714–1722, 1995.

[23] Geoff Warnock, Mohamed-Ali Bahri, David Goblet, Fabrice Giacomelli, Christian Lemaire, Joel Aerts, Alain Seret, Xavier Langlois, Andre Luxen, and Alain Plenevaux. Use of a beta microprobe system to measure arterial input function in pet via an arteriovenous shunt in rats. *EJNMMI research*, 1(1):13, 2011.

[24] Bruno Weber, Cyrill Burger, Peter Biro, and Alfred Buck. A femoral arteriovenous shunt facilitates arterial whole blood sampling in animals. *European journal of nuclear medicine and molecular imaging*, 29(3):319–323, 2002.

[25] Martin P Tornai, Edward J Hoffman, Lawrence R MacDonald, and Craig S Levin. Characterization of fluor concentration and geometry in organic scintillators for in situ beta imaging. *IEEE Transactions on Nuclear Science*, 43(6):3342–3347, 1996.

[26] Chie Seki, Hiroyuki Okada, Shinsuke Mori, Takeharu Kakiuchi, Etsuji Yoshikawa, Shingo Nishiyama, Hideo Tsukada, and Takaji Yamashita. Application of a beta microprobe for quantification of regional cerebral blood flow with 15 o-water and pet in rhesus monkeys. *Annals of nuclear medicine*, 12(1):7–14, 1998.

[27] Frédéric Pain, Philippe Lanièce, Roland Mastrippolito, Philippe Gervais, Philippe Hantraye, and Laurent Besret. Arterial input function measurement without blood sampling using a β-microprobe in rats. *Journal of Nuclear Medicine*, 45(9):1577–1582, 2004.

[28] S Maramraju, S Stoll, C Woody, D Schlyer, W Schiffer, D Lee, S Dewey, and P Vaska. A lso β microprobe for measuring input functions for quantitative

small animal pet. *Nuclear Instruments and Methods in Physics Research Section A: Accelerators, Spectrometers, Detectors and Associated Equipment*, 571(1-2):407–410, 2007.

[29] Josh Knowland, Ronald Lattanze, Jesse Kingg, and Steven Perrin. Practical clinical measurement of radiotracer concentration in blood – initial device concept and feasibility testing. *Journal of Nuclear Medicine Technology*, 46:jnmt.118.212266, 08 2018.

[30] Friedrich Roehrbacher, Jens P Bankstahl, Marion Bankstahl, Thomas Wanek, Johann Stanek, Michael Sauberer, Julia Muellauer, Thales Schroettner, Oliver Langer, and Claudia Kuntner. Development and performance test of an online blood sampling system for determination of the arterial input function in rats. *EJNMMI physics*, 2(1):1, 2015.

[31] Laurence Convert, Réjean Lebel, Suzanne Gascon, Réjean Fontaine, Jean-François Pratte, Paul Charette, Vincent Aimez, and Roger Lecomte. Real-time microfluidic blood-counting system for pet and spect preclinical pharmacokinetic studies. *J Nucl Med*, 57(9):1460–6, 2016.

[32] D Lapointe, J Cadorette, S Rodrigue, D Rouleau, and R Lecomte. A microvolumetric blood counter/sampler for metabolic pet studies in small animals. *IEEE Transactions on Nuclear Science*, 45(4):2195–2199, 1998.

[33] Laurence Convert, Guillaume Morin-Brassard, Jules Cadorette, Mélanie Archambault, M'hamed Bentourkia, and Roger Lecomte. A new tool for molecular imaging: the microvolumetric β blood counter. *Journal of Nuclear Medicine*, 48(7):1197–1206, 2007.

[34] GD Hutchins, RD Hichwa, and RA Koeppe. A continuous flow input function detector for h2 15o blood flow studies in positron emission tomography. *IEEE Transactions on Nuclear Science*, 33(1):546–549, 1986.

[35] Michael M Graham and Barbara L Lewellen. High-speed automated discrete blood sampling for positron emission tomography. *Journal of nuclear medicine: official publication, Society of Nuclear Medicine*, 34(8):1357–1360, 1993.

[36] SY Lu and VW Pike. Micro-reactors for pet tracer labeling. In *PET Chemistry*, pages 271–287. Springer, 2007.

[37] James M Gillies, C Prenant, GN Chimon, GJ Smethurst, W Perrie, Ian Hamblett, B Dekker, and Jamal Zweit. Microfluidic reactor for the radiosynthesis of pet radiotracers. *Applied radiation and isotopes*, 64(3):325–332, 2006.

[38] Mark D Tarn, Nuray Yavuzkanat Kızılyer, Mohammad MN Esfahani, Pankaj Joshi, Nathaniel J Brown, Nicole Pamme, David G Jenkins, and Stephen J

Archibald. Plastic scintillator-based microfluidic devices for miniaturized detection of positron emission tomography radiopharmaceuticals. *Chemistry–A European Journal*, 24(52):13749–13753, 2018.

[39] Noel Ha, Saman Sadeghi, and R van Dam. Recent progress toward microfluidic quality control testing of radiopharmaceuticals. *Micromachines*, 8(11):337, 2017.

[40] Matthew P Taggart, Mark D Tarn, Mohammad MN Esfahani, Daniel M Schofield, Nathaniel J Brown, Stephen J Archibald, Tom Deakin, Nicole Pamme, and Lee F Thompson. Development of radiodetection systems towards miniaturised quality control of pet and spect radiopharmaceuticals. *Lab on a Chip*, 16(9):1605–1616, 2016.

[41] Glenn F Knoll. *Radiation detection and measurement.* John Wiley & Sons, 2010.

[42] Zhonghua Kuang, Xiaohui Wang, Xin Fu, Ning Ren, Qian Yang, Binqing Zhao, Chunhui Zhang, San Wu, Ziru Sang, Zhanli Hu, et al. Dual-ended readout small animal pet detector by using 0.5 mm pixelated lyso crystal arrays and sipms. *Nuclear Instruments and Methods in Physics Research Section A: Accelerators, Spectrometers, Detectors and Associated Equipment*, 917:1–8, 2019.

[43] K Doroud, Z Liu, and MCS Williams. A new geometry of scintillating crystals with strip sipms: a pet detector with precise position and time determination. *Journal of Instrumentation*, 14(01):P01016, 2019.

[44] A Ros, L Barrientos, J Barrio, A Etxebeste, C Lacasta, E Muñoz, JF Oliver, J Roser, and G Llosá. Evaluation of lfs continuous scintillation crystals for pet. *Nuclear Instruments and Methods in Physics Research Section A: Accelerators, Spectrometers, Detectors and Associated Equipment*, 2018.

[45] J Hu, J Liu, L Chen, Z Zhang, X Ouyang, S He, M Xu, L Zhou, W Yan, and Z Yao. Identification of heavy ions by imaging individual particle tracks in cf4-filled gas scintillation detectors. *Journal of Instrumentation*, 13(09):P09025, 2018.

[46] Woo Nyun Choi, UkJae Lee, Jun Woo Bae, and Hee Reyoung Kim. Minimum detectable activity of plastic scintillator for in-situ beta measurement system in ground water. *Nuclear Engineering and Technology*, 2019.

[47] Seiichi Yamamoto, Katsuhiko Kato, Naotoshi Fujita, Masato Yamashita, Takuya Nishimoto, Hiroshi Kameyama, and Shinji Abe. Detection of alpha radionuclides in air from patients during ra-223 alpha radionuclide therapy. *Scientific reports*, 8(1):10976, 2018.

[48] J Antunes, J Machado, L Peralta, and N Matela. Plastic scintillation detectors for dose monitoring in digital breast tomosynthesis. *Nuclear Instruments and Methods in Physics Research Section A: Accelerators, Spectrometers, Detectors and Associated Equipment*, 877:346–348, 2018.

[49] Luis Peralta and Florbela Rêgo. Response of plastic scintillators to low-energy photons. *Physics in Medicine & Biology*, 59(16):4621, 2014.

[50] Kei Wagatsuma, Kenta Miwa, Muneyuki Sakata, Keiichi Oda, Haruka Ono, Masashi Kameyama, Jun Toyohara, and Kenji Ishii. Comparison between new-generation sipm-based and conventional pmt-based tof-pet/ct. *Physica Medica*, 42:203–210, 2017.

[51] Chankyu Kim, Hyoungtaek Kim, Jongyul Kim, Chaehun Lee, Hyunjun Yoo, Dong Uk Kang, Minsik Cho, Myung Soo Kim, Daehee Lee, Yewon Kim, et al. Replacement of a photomultiplier tube in a 2-inch thallium-doped sodium iodide gamma spectrometer with silicon photomultipliers and a light guide. *Nuclear Engineering and Technology*, 47(4):479–487, 2015.

[52] Kei Wagatsuma, Muneyuki Sakata, Kenji Ishibashi, Akira Hirayama, Hirofumi Kawakami, Kenta Miwa, and Kenji Ishii. Direct comparison between sipm-and pmt-pet/ct in [18f] fdg brain imaging. *Journal of Nuclear Medicine*, 60(supplement 1):1390–1390, 2019.

[53] Saint-Gobain Ceramics and Inc. Plastics. Scintillating optical fibers.

[54] Johan Pihl, Mattias Karlsson, and Daniel T Chiu. Microfluidic technologies in drug discovery. *Drug Discovery Today*, 10(20):1377–1383, 2005.

[55] Shikuan Yang, Feng Guo, Brian Kiraly, Xiaole Mao, Mengqian Lu, Kam W Leong, and Tony Jun Huang. Microfluidic synthesis of multifunctional janus particles for biomedical applications. *Lab on a Chip*, 12(12):2097–2102, 2012.

[56] Junping Ma, Simon Ming-Yuen Lee, Changqing Yi, and Cheuk-Wing Li. Controllable synthesis of functional nanoparticles by microfluidic platforms for biomedical applications–a review. *Lab on a Chip*, 17(2):209–226, 2017.

[57] Kangning Ren, Jianhua Zhou, and Hongkai Wu. Materials for microfluidic chip fabrication. *Accounts of chemical research*, 46(11):2396–2406, 2013.

[58] Sea Agostinelli, John Allison, K al Amako, John Apostolakis, H Araujo, P Arce, M Asai, D Axen, S Banerjee, G 2 Barrand, et al. Geant4—a simulation toolkit. *Nuclear instruments and methods in physics research section A: Accelerators, Spectrometers, Detectors and Associated Equipment*, 506(3):250–303, 2003.

[59] John Allison, Katsuya Amako, JEA Apostolakis, HAAH Araujo, P Arce Dubois, MAAM Asai, GABG Barrand, RACR Capra, SACS Chauvie, RACR Chytracek, et al. Geant4 developments and applications. *IEEE Transactions on nuclear science*, 53(1):270–278, 2006.

[60] Aigars Piruska, Irena Nikcevic, Se Hwan Lee, Chong Ahn, William R. Heineman, Patrick A. Limbach, and Carl J. Seliskar. The autofluorescence of plastic materials and chips measured under laser irradiation. *Lab Chip*, 5:1348–1354, 2005.

[61] Martin Janecek and William W Moses. Simulating scintillator light collection using measured optical reflectance. *IEEE Transactions on Nuclear Science*, 57(3):964–970, 2010.

[62] Eljen Technology. Reflective paint ej-510, ej-520, 2016.

[63] AP Ivashkin, Yu G Kudenko, OV Mineev, and J Imazato. Scintillation ring hodoscope with wls fiber readout. *Nuclear Instruments and Methods in Physics Research Section A: Accelerators, Spectrometers, Detectors and Associated Equipment*, 394(3):321–331, 1997.

[64] Wei-Yu Tseng, JS Cho, X Ma, A Kunihiro, A Chatziioannou, and RM Van Dam. Toward reliable synthesis of radiotracers for positron emission tomography in pdms microfluidic chips: Study and optimization of the [18f] fluoride drying process. In *Technical Proceedings of the 2010 NSTI Nanotechnology Conference and Trade Show*, volume 2, pages 472–475, 2010.

[65] Arkadij M Elizarov, R Michael van Dam, Young Shik Shin, Hartmuth C Kolb, Henry C Padgett, David Stout, Jenny Shu, Jiang Huang, Antoine Daridon, and James R Heath. Design and optimization of coin-shaped microreactor chips for pet radiopharmaceutical synthesis. *Journal of Nuclear Medicine*, 51(2):282–287, 2010.

[66] Jean-Marc Reymond, David Guez, Sophie Kerhoas, Philippe Mangeot, Raphaël Boisgard, Sébastien Jan, Bertrand Tavitian, and Régine Trebossen. Development of an instrument for time–activity curve measurements during pet imaging of rodents. *Nuclear Instruments and Methods in Physics Research Section A: Accelerators, Spectrometers, Detectors and Associated Equipment*, 571(1-2):358–361, 2007.

[67] T Kurtukian-Nieto, J Benlliure, and K-H Schmidt. A new analysis method to determine β-decay half-lives in experiments with complex background. *Nuclear Instruments and Methods in Physics Research Section A: Accelerators, Spectrometers, Detectors and Associated Equipment*, 589(3):472–483, 2008.

[68] A Zacheo, V Arima, G Pascali, PA Salvadori, A Zizzari, E Perrone, L De Marco, G Gigli, and R Rinaldi. Radioactivity resistance evaluation of polymeric materials for application in radiopharmaceutical production at microscale. *Microfluidics and nanofluidics*, 11(1):35–44, 2011.

Appendix A

(a)

(b)

(c)
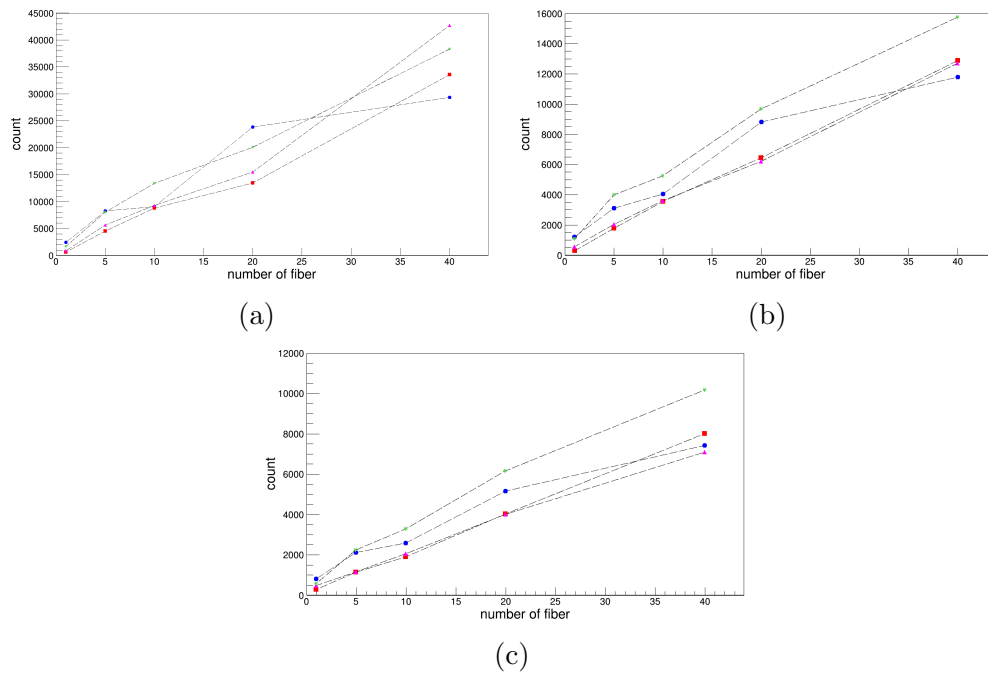
Figure A.1: Comparison of 1×1 mm^2 Sensl SiPM (blue), hammamatsu 3×3mm^2 MPPC S13360-3025PE(red), hammamatsu 1.3×1.3 mm^2 TE-cooled MPPC module(pink) and 1×3 mm^2 μPMT(green) for 1, 5, 10, 20 and 40 fiber bundle at (a)1 cm, (b)2 cm and (c)3 cm distance from ^{137}Cs source.